DISSERTATION

submitted to the

Combined Faculty of Natural Sciences and Mathematics
of Heidelberg University, Germany

for the degree of

Doctor of Natural Sciences

Put forward by

Saba Zia Hassan

born in: Delhi, India

Oral examination: May 24th, 2022

DYNAMICS OF ANIONS AND ULTRACOLD ATOMS IN A HYBRID ATOM-ION TRAP

SABA ZIA HASSAN

Referees: Prof. Dr. Matthias Weidemüller

Prof. Dr. Andreas Wolf

"An experiment is a question which science poses to Nature and a measurement is the recording of Nature's answer."

-Max Planck

ABSTRACT

In this work, the dynamics of anion-neutral interactions are studied in a hybrid atom-ion trap. An octupole radio-frequency trap is used for trapping anions, and a dark spontaneous-force optical trap is employed to create ultracold rubidium (Rb) atoms. Spatial density distributions of the ion and atom clouds are determined via photodetachment tomography and saturation absorption imaging, respectively. A method to map the ions' translational temperature onto their time of flight to the detector is presented. This technique is applied to determine the temperature of OH^- anions as they undergo laser-induced forced evaporative cooling to temperatures below 4 K. The dynamics of associative electronic detachment reaction between closed-shell anions OH^- and alkali atoms Rb are investigated where for a ground-state Rb the influence of a dipole-bound state as a reaction intermediate is observed. The interaction dynamics of Rb with $OH^-(H_2O)$ are also explored, where a smaller atom-to-ion mass ratio favors ion sympathetic cooling via elastic collisions. For atomic O^-, the detachment processes involving ground-state Rb are found to be closed and efficient anion sympathetic cooling, via ultracold Rb, is observed. These results present hybrid systems as a platform to investigate anion-neutral collision dynamics, particularly interesting for astrochemistry, fundamental physics, and quantum chemistry.

ZUSAMMENFASSUNG

In dieser Arbeit wird die Dynamik von Anion-Neutral-Wechselwirkungen in einer hybriden Atom-Ionen-Falle untersucht. Eine Oktupol-Hochfrequenzfalle wird zum Fangen von Anionen verwendet, und eine dunkle optische Falle mit spontaner Kraft wird verwendet, um ultrakalte Rubidiumatome (Rb) zu erzeugen. Räumliche Dichteverteilungen der Ionen- und Atomwolken werden mittels Photodetachment-Tomographie bzw. Sättigungsabsorptions-Bildgebung bestimmt. Eine Methode, um die Translationstemperatur der Ionen auf ihre Flugzeit zum Detektor abzubilden, wird vorgestellt. Diese Technik wird angewendet, um die Temperatur von OH^- Anionen zu bestimmen, während sie durch eine laserinduzierte erzwungenen Verdunstungskühlung auf Temperaturen von unter 4 K werden. Die Dynamik assoziativer elektronischer Ablösungsreaktionen zwischen geschlossenschaligen Anionen OH^- und Alkaliatomen Rb wird untersucht, wobei für den Grundzustand von Rb, der Einfluss eines Dipol-gebundenen Zustands als Reaktionsintermediat beobachtet wird. Die Wechselwirkungsdynamik von Rb mit $OH^-(H_2O)$ wird ebenfalls untersucht, wobei ein kleineres Atom-zu-Ionen-Massenverhältnis die sympathische Ionenkühlung durch elastische Stöße begünstigt. Effiziente sympathische Kühlung von Anionen über ultrakaltes Rb wird für atomares O^- beobachtet, wo sich herausstellt, dass die Ablösungsprozesse mit Rb im Grundzustand unterdrückt sind. Diese Ergebnisse präsentieren Hybridsysteme als Plattform zur Untersuchung der Anion-Neutral Kollisionsdynamik, die besonders interessant für Astrochemie, Grundlagenphysik und Quantenchemie ist.

LIST OF PUBLICATIONS

This work is based on the following peer-reviewed publications.

- Markus Nötzold, Saba Zia Hassan, Jonas Tauch, Eric Endres, Roland Wester, and Matthias Weidemüller. "Thermometry in a Multipole Ion Trap." Appl. Sci. **10**(15), 5264 (2020) [1].
- Saba Zia Hassan, Jonas Tauch, Milaim Kas, Markus Nötzold, Henry López Carrera, Eric S. Endres, Roland Wester, and Matthias Weidemüller. "Associative detachment in anion-atom reactions involving a dipole-bound electron." Nat. Commun. **13**, 818 (2022) [2].
- Saba Zia Hassan, Jonas Tauch, Milaim Kas, Markus Nötzold, Roland Wester, and Matthias Weidemüller. "Quantum state-dependent anion–neutral detachment processes." J. Chem. Phys. **156**, 094304 (2022) [3].

This work also consists of results detailed in the following manuscripts.

- Jonas Tauch, Saba Zia Hassan, Markus Nötzold, Eric Endres, Roland Wester, and Matthias Weidemüller. "Laser induced forced evaporative cooling of molecular anions to the Kelvin range" **(in preparation)**.
- Jonas Tauch, Saba Zia Hassan, Markus Nötzold, Eric Endres, Roland Wester, and Matthias Weidemüller. "Sympathetic cooling of O^- and OH^- by an ultracold heavy buffer gas" **(in preparation)**.

TABLE OF CONTENTS

Page

1 A brief history in time

An introduction to hybrid atom-ion trapping 1

1.1 Developments of atom and ion traps 2

1.2 Hybrid traps as tools for atom-ion research 3

1.3 Anions in nature 6

1.4 Research on anion-neutral collisions 9

1.5 Outline of this thesis 11

2 Hybrid atom-ion trap

An introduction to the experimental setup and methods 13

2.1 Anion production, trapping, and extraction 15

2.2 Creation of an ultracold atom cloud 16

2.3 Ion-atom diagnostics 17

  2.3.1 Photodetachment tomography for anions 18

  2.3.2 Atom distribution via saturation absorption imaging 19

  2.3.3 Excited state atoms via fluorescence imaging 21

  2.3.4 Determination of reaction rate coefficients 23

3 Thermometry in a multipole trap 25

3.1 Motivation for temperature diagnostics 25

3.2 Thermometry in a multipole ion trap 26

3.3 Mapping ion temperature to their TOF 44

3.4 Temperature determination in anion cooling 47

4 Dynamics of molecular anions with atoms 51

4.1 Insights on anion-neutral reaction dynamics 51

4.2 Associative detachment in anion-atom reactions 52

4.3 Effect of hydration on hydroxide anions 70

  4.3.1 Preparation of ion cloud 70

  4.3.2 Qualitative description of anion cooling via ultracold atoms 73

5 Dynamics of atomic anions with atoms **79**
5.1 Hybrid systems for state-dependent studies 79
5.2 Quantum state-dependent detachment processes 80
5.3 Sympathetic cooling of atomic anions 90

6 Synopsis

Summary & Outlook **95**

Bibliography **105**

CHAPTER 1

A BRIEF HISTORY IN TIME

An introduction to hybrid atom-ion trapping

The established techniques of atom and ion trapping and their combined study in hybrid atom-ion traps, with their remarkable contributions in advancing the studies on cation-neutral interaction dynamics, also motivated the use of such hybrid systems to push the frontiers in anion-neutral research. The hybrid atom-ion trap, which is the focus of this work, was conceived over a decade ago as an international collaboration under the guidance of Prof. Dr. Matthias Weidemüller from the University of Heidelberg, Germany, and Prof. Dr. Roland Wester from the University of Innsbruck, Austria, providing a platform to study anion-neutral collision dynamics in well-controlled conditions.

This chapter starts with walking the reader through the historical advancements in the individual fields of the atom and ion trapping. The combination of these two diverse fields, led to the realization of hybrid atom-ion traps to study atom-ion interactions with unprecedented control and precision. Inspired by these developments in the understanding of cation-neutral interactions in hybrid traps, the idea of studying anionic systems in such cold and well-controlled conditions is motivated. To underline the relevance and importance of anion research, the role of anions as important species in distinct environments, as well as their interactions with other particles, are elucidated upon. These insights are then brought together, to motivate the use of a hybrid atom-ion trap for exploring anion-neutral collision dynamics, and an outline of the results that were achieved during the framework of the collaboration and particularly, this thesis are presented.

1.1 Developments of atom and ion traps

The quest to cool particles to absolute zero has always been a fascinating, albeit a challenging journey. With every new advancement towards a new temperature regime, a plethora of exotic and novel processes is revealed [4]. At the beginning of the 20th century, cooling helium-4 particles into the sub-10 Kelvin range led to the discovery of superconductivity and superfluidity [5, 6, 7]. Soon afterward, superfluidity of helium-3 was demonstrated in the millikelvin regime [8]. With the emergence of laser cooling techniques, the frontiers of these observed low temperatures were pushed further into the ultracold regime [9, 10, 11]. The pioneers of this groundbreaking research were duly awarded the physics Nobel Prize in 1997 [12, 13, 11]. The possibility to cool atoms to the microkelvin range (and below) has led to unprecedented developments in the field of cold and ultracold research [14]. These works include, but are not limited, to the enhancement of atomic clocks [15, 16], precision studies of fundamental physics [17, 18], study of quantum many-body phenomena [19, 20], quantum simulation [21, 22, 23] and information processing [24, 25]. The ultracold atomic systems offer well-controlled and highly scalable environments often connecting the rather distinct field of atomic physics and quantum optics research to condensed matter [26], solid-state [27] and even high-energy physics [28]. Thus, from the study of the fundamental quantum nature of light-matter interactions to the application of these ideas to shape the quantum technologies of the future, the development of laser cooling techniques for the creation of ultracold atoms has played a pivotal role [29, 30].

The 20th century was not only an exciting time for the field of atomic physics. Motivated by the possibility to observe isolated particles, Hans Dehmelt and Wolfgang Paul developed the techniques for trapping ions employing the use of static electric/magnetic fields (Penning traps) [31, 32, 33] and radio-frequency (rf) fields (Paul traps) [34], respectively. Soon after their realization, the groups of Peter Toschek and David Wineland, achieved laser cooling of trapped ions in these two traps [35, 36]. While the former was the first to photograph individual trapped Ba^+ ions in a Paul trap [37], the latter demonstrated the first clock that implemented the principles of laser cooling in a Penning trap and was awarded the Nobel Prize in 2012 for pioneering work on the manipulation of individual systems [38]. Trapped ions have long lifetimes and long-range interactions, offering systems with a high degree of control. Another method to store ions for extended periods of time, which has been of key importance to further the research on atomic and molecular ions, is the ion storage ring [39]. These systems, apart from fundamental research [40], also find their applications in exploratory studies of astrophysical relevance [41, 42]. However, with developments in the field of ion traps, many groups were able to realize the rather compact ion trap setups, drastically scaling down the physical constraints from a technological point of view. Additionally, ion traps (in combination with laser cooling) offer a platform to overlap the trapped ions with other neutral or charged particles, to investigate their interaction dynamics even at low collision energies. These features make ion traps an indispensable tool for research in diverse fields like precision spectroscopy [43, 44], cold chemistry [45, 46], fundamental physics phenomena [47, 48], many-body quantum physics [49, 50], and quantum information processing [51, 52, 53], to name a few.

1.2 Hybrid traps as tools for atom-ion research

Given their widespread application, it can be safely said that the fields of trapped atoms and ions are the two cornerstones of today's research on exploring the dynamics of fundamental processes as well as the upcoming quantum technologies [54]. The amalgamation of the novel and distinct features of these systems led to the development of hybrid atom-ion traps. These systems employing ion traps offer a high degree of control and spatial localization with a long lifetime in the trap. The addressability of ions via laser beams also allows for their optical detection and precise state-control. For instance, laser-cooling of ions along with the inherent Coulombic repulsive forces in ionic systems allows the ions to be spatially separated and thus, individually detected and addressed via optical forces. This provides a localized ion probe for investigating an atomic bath [55]. The ultracold atomic clouds in hybrid traps offer a system with a large degree of scalability along-with long coherence times, which can also be used as a coolant species for the sympathetic cooling of ions. In addition to the complementary features of long-range and short-range van der Waals interactions of purely ionic and atomic systems respectively, the hybrid traps make it possible to investigate and tune intermediate-range ion-atom interactions [54, 56, 57].

The first realization of a hybrid atom-ion trap system was achieved less than two decades ago, but this field has already seen tremendous developments. The first hybrid traps were reported in the first decade of the 21st century, with the early experiments employing Paul traps and magneto-optical traps [58, 59, 60]. To date, Paul traps seem to be the go-to choice for ion trapping in such systems as the collisions of ions with atomic species in Penning traps would render the orbital motion unstable [61]. Unlike Penning traps, Paul traps do not employ large magnetic field coils that need to be cooled via liquid helium and are thus easier to implement from an engineering and technical point of view.

The first proof-of-principle experiment in 2005, showed the experimental feasibility of hybrid atom-ion systems and demonstrated the co-trapping of Ca^+

ions with ultracold Na atoms [58]. These systems have been an experimental and theoretical playground to investigate atom-ion collisions dynamics in the cold and ultracold regime ever since. Co-trapped ion-atom species undergo primarily three kinds of collisions: elastic, inelastic, and reactive. Elastic collisions result in energy transfer in the translational degree of freedom. Inelastic processes primarily involve state-changing collisions, like the rotational states for molecular ions and reactive collisions including the atom-ion reaction process like associative electronic detachment (AED), charge-transfer, or charge-exchange process, etc.

The first experimental results on ion-atom reactive collisions were presented in 2009, on the charge-exchange reactions in the Yb^+-Yb system for collision energies between 35 mK and 45 K [59]. The initial designs were further developed to enable systems with lower atomic temperatures, such as the ones using an optical dipole trap or a Bose-Einstein condensate (BEC). In 2010, investigations on the charge-exchange processes in the Yb^+-Rb system were presented and demonstrated, for the first time, sympathetic cooling of an ion to 0.6(7) K by immersing it in a BEC [62, 63]. The use of the single-ion as a probe for mapping atomic density profile was demonstrated in the Ba^+-Rb system, where the ions, estimated to be at a temperature ≈ 40 mK, were co-trapped with a Rb BEC [55].

These developments marked the beginning of an era that used these hybrid systems as platforms to explore controlled chemical reactions. In the early 2010s, the study on the charge-exchange reactions in the Yb^+-Rb system was further developed to experimentally explore the influence of electronically excited states on the reaction rates [64]. Such electronic quantum state-dependent charge transfer reactions were also studied in Yb^+-Ca and Yb^+-Li systems [65, 66]. It was shown how the change in the electronic quantum state can result in the suppression of certain charge-exchange processes. The work on other systems of Rb^+-Rb [67], Ca^+-Na [58] and also molecular ions in $BaCl^+$-Ca [68] further demonstrated the effect of electronic excitation of the atoms, due to the cooling lasers, on the reactive processes occurring in the systems. Subsequently, the light-assisted radiative charge-exchange and molecule formation were studied in the Ca^+-Rb system, where the laser-cooled Ca^+ ions formed a crystal [60, 69]. The work on the Coulomb crystals was further developed to study reactions between laser-cooled Ba^+ ions and Rb atoms [70]. Towards the later years of the decade, the excited state-dependent charge-exchange collisions were investigated for Ca^+-Li in the mK energy regime [71], and the measured reaction rate coefficients were compared to a theoretical semi-classical capture model proposed in [72]. Subsequently, the sympathetic cooling of the ions by suppressing heating effects in the rf trap was demonstrated [73]. This was particularly remarkable, as it is commonly seen that the ions in a Paul trap do not thermalize to the temperature of the buffer gas used. This is attributed to the micromotion which is a fast oscillatory motion, in addition to the ions' secular motion, in ponderomotive rf-field potential. These oscillatory rf-fields result in the heating of the ions during elastic collisions. This has been a major limitation for achieving temperatures pertaining to the s-wave scattering regime which is already two orders of magnitude lower in atom-ion systems, as compared to that of its neutral counterparts [74].

In recent years, a large number of systems focus on the study of spin-changing collisions. These include the study of spin-exchange rates in Sr^+-Rb and Yb^+-Li systems, or spin relaxation rates in Sr^+-Rb system [75, 76, 77]. Theoretical studies on these processes revealed the possibility to probe Feshbach resonances in the s-wave regime in systems where a large difference between the singlet and triplet scattering length exists like for the Yb^+-Li system [78, 79]. These predictions have been recently experimentally confirmed in 2021, where for the first time Feshbach resonances in the long-range particle interactions were observed between a single laser-cooled Ba^+ ion and Li atoms in a crossed optical dipole trap. Four out of eleven resonances observed were identified as s-wave resonances, rendering these systems particularly interesting in paving the way for applications in many-body physics [80, 81], and quantum simulations [82, 83]. With these works, it is evident that the steady technological and conceptual advancements in the field of hybrid atom-ion trapping have led to monumental growth in the understanding of atom-ion collisional dynamics. These studies also highlight the role of quantum state-dependence of the reactive processes that occur in distinct hybrid systems, including the probing into the novel s-wave regime.

However, from the exhaustive list of the systems discussed above, it is also quite evident that the majority of these systems employ the well-established laser-cooling techniques for cooling and observing the ions which are exclusively cationic species, completely leaving out their negative counterparts. The anion-neutral collisions in hybrid atom-ion traps are of interest in several theoretical studies [84, 85, 86], but experimental investigations on these systems are rather sparse. While laser cooling of ions has been of central importance for the isolated trapping and manipulating of cations, anions have resisted all attempts at direct laser cooling due to the lack of closed-optical transitions in most anions. Several candidates like the atomic anions Os^- [87], La^- [88] exist and schemes for Doppler laser-cooling of molecular anions like OH^- [89], C_2^- [90, 91] were proposed, but direct laser-cooling of anions has, till date, not been experimentally achieved.

Creating an ultracold ensemble of any anionic species would further enable to sympathetically cool any other atomic or molecular anionic particles, including electrons and antiprotons. Laser-induced cooling of anions via evaporative techniques had already been proposed over three decades ago [92] and was recently shown experimentally in a linear Paul trap for the cooling of atomic O^- anions from 1.15 eV to 0.33 eV [93]. Another evaporative cooling technique based on the alteration of the ion trap's potential landscape was demonstrated experimentally to cool trapped antiprotons down to 9 K [94]. This is of particular importance in the studies involving antihydrogen or antimatter in general [95].

The storage rings also provide a pivotal system to probe the internal cooling of molecular anions. Combining the ion storage technique with high-resolution detachment spectroscopy, the radiative cooling of vibrationally excited C_2^- was experimentally observed [96]. The rotational quantum states were experimentally probed for the OH^- anions, employing near-threshold photodetachment in a cryogenic storage ring (CSR) [97, 98]. The molecular anions were cooled internally, corresponding to a steady-state effective internal temperature of 13-15 K. The CSR provides a cryogenic environment with long ion storage times, constituting a novel system to study collisional [99] as well as radiative [40] processes in cations, but also anions of varying molecular complexity [100, 101, 102].

Thus, cooling anions to low temperatures has increasingly gained attention in theoretical and experimental studies, prompting the need to devise efficient cooling techniques for trapping, cooling, and manipulating anions and eventually investigating anion-neutral interactions. Analogous to the atoms and cations, the possibility to study anions in a well-controlled manner in cold or even ultracold regimes would provide valuable insights into their chemical and physical properties and also their applications in many diverse fields, like precision spectroscopy [103, 104], the study of fundamental interactions [105, 106], cold-chemistry [107, 108] and astrochemistry [109, 110, 111].

1.3 Anions in nature

To address the stability of an anion, one of the properties that are frequently addressed or referred to is the electron affinity (EA) [112]. It is an intensive property and is defined as the energy difference between the neutral and its corresponding anionic species, when both are in their electronic as well as the rovibrational ground states. Thus, the EA quantifies how strongly the excess electron is bound to the neutral core. For an anion with a positive EA, it is said to be a stable entity as energy is needed to remove the electron to create its neutral counterpart. Until the 1970s and 1980s, even the most fundamental data like the EAs, were not directly or precisely determined for most of the anions, as the experimental frameworks for these studies were limited by the technology of the time. With the improvements in light and ion production and storage sources, the subsequent decades saw major improvements in both the quality (precision) and quantity (the species studied) of the research into determining the EAs of different anions. As the experimental investigations advanced, this field garnered the attention of physicists and theoretical chemists alike, to develop and improve methods to determine the anions' fundamental structural and spectroscopic properties. As interest grew, it led to several investigatory studies on the role of anions as important constituents in varied fields like in the interstellar medium (ISM), in the Earth's atmosphere, biological clusters, plasmas, and minuscule nanoscopic materials, some of which are highlighted as follows.

The presence of cations in the ISM has been long established since 1941. However, it was only in late 2006, that the detection and identification of numerous carbon chain anions were confirmed [113]. Prior to this discovery, the most relevant anion for astrophysics (or chemistry) was the H^- anion. The radiative attachment of electrons to the neutral H to create anionic hydrogen and the associative electronic detachment (AED) between neutral and anionic hydrogen, led to the formation of molecular hydrogen gas with the detachment of the excess electron [114]. The study of this seemingly simple process was pivotal in the understanding of the formation of particles in the early Universe [115]. With the unforeseen detection of molecular anions in the 2007 Cassini mission in the upper atmosphere of Saturn's moon Titan, the interest in the study of anions in space has tremendously grown [116]. This led to further investigations into the chemical reactions, of these astrochemically relevant anions, with neutrals to understand the creation and/or destruction dynamics of different particles in these hostile environments by attempting to simulate these astrophysical conditions in the laboratories [117, 118]. In the Earth's ionosphere, negative ions were also detected in the lower ionosphere in the polar region. The associative detachment reaction between O^- and molecular oxygen gas results in the formation of the Ozone particles, which are critical for the life on Earth [119, 120].

Anions also play a fundamental role in signal transduction and energy storage in many biological systems, like the phosphate anions for enzymatic reactions involving zinc (II) ions [121, 122]. The investigations into the interactions between aromatic rings and carboxylate anions have also shed light on the biological relevance of anion quadrupole interactions [123]. The study of the reactivity of amino-acid anions with nitrogen and oxygen in laboratory astrophysics is critical to understanding the amino-acid behavior in extra-terrestrial environments [124].

Apart from the exploratory studies to explain the origin of life on Earth seeded by extraterrestrial molecules, research involving anions in applied fields is also gaining widespread interest. Heavy anions have been detected in plasmas and the study of the formation of dusty, reactive plasmas involving negative ions is important in the field of colloidal chemistry, and also Coulomb crystals [125]. Such ion-ion plasmas comprising of anions instead of electrons are also used in silicon etching and thin film deposition industries [126, 127]. From an additional industrial point of view, the development of molecular gates which can be controlled with the presence of certain anions at the nanoscopic scale would be an imperative building block for the future of nanometric devices [128, 129].

It can be seen that the universality of anions in a vast multitude of environments, encapsulating areas of the gigantic extra-terrestrial space right down to the development of minute nanoscopic particles, makes the anions ubiquitous in nature. The study of these anionic systems in well-controlled conditions would not only further our knowledge about the fundamental processes that occur in nature but also elaborate on how these insights could be developed further from a technological point of view.

Given the common occurrences of anions in nature, the presence of an attractive potential between the core and the excess electron of the anion is implied. In the asymptotic regions, the attractive potential that the valence electron feels falls for cations and neutrals as $-Ze^2/r$, where $Z = 1$ for neutral and $Z = 2$ for singly-charged particles, e is the elementary charge and r is the distance between the electron and the core. However, for anions, this potential scales significantly slower with increasing distance. The long-range attractive potentials important for an electron in singly-charged anions are the charge-dipole ($\propto 1/r^2$), the charge-quadrupole ($\propto 1/r^3$) and the charge-induced dipole ($\propto 1/r^4$) potentials [112]. Anions, whose neutral counterparts possess a large permanent dipole moment can support excited electronic states that are close to the detachment threshold, mediated via a charge-dipole interaction. Such anions are called dipole bound anions (DBAs), observed experimentally for the first time in Lykke *et. al* [130]. These anions have gone from being esoteric to being of great relevance in mainstream chemistry as these anions can act as precursors to the formation of valence-bound anions [131] and also play an important role in zwitterion chemistry [132, 133]. Even anions that are considered valence-bound can exhibit dipole-bound states, as long as they support large dipole moments. Thus, while anions like OH^- are valence-bound anions, other anions like the alkali hydroxides are dipole-bound where the reaction between alkali and hydroxide anion is primarily mediated via dipolar forces [86]. It is noteworthy to add, that with these novel interaction dynamics with the neutral atoms, OH^- is one of the most well-investigated anions, both experimentally and theoretically, due to its simplicity and importance in astrophysics [134], laser chemistry [135] and spectroscopic studies [104, 136].

1.4 Research on anion-neutral collisions

As we have seen, while anions are on their own a very interesting species, they can exhibit novel dynamics when undergoing interactions with other neutral or even cationic particles. Many phenomena involving anions are interpreted via the reaction rate coefficients of anions interacting with different neutral particles. The simplest model to explain the ion-neutral collision dynamics is given by the Langevin capture model. In an entirely classical picture, this describes the interaction between two colliding particles solely governed by the long-range charge-induced dipole interaction [137, 138]. Investigations into ion-neutral reactions often reveal deviations from this model, and the interaction potential of the collision complex is then modified to account for other short-range effects.

Several experimental setups have been developed to study anion-neutral reactions [139]. For instance in flowing afterglow and ion drift tube experiments [140, 141, 142, 143] anion-neutral reactions can be studied at high temperatures (up to a few hundred Kelvin) and the reaction partners can also be independently controlled. Guided ion beams are also extensively used to study collision-energy dependent reaction processes and cross-sections, with energies ranging between 0.1 eV to nearly 20 eV [144, 145]. A method that is currently widely used to study reaction kinematics in experiments is the crossed molecular beams, and its developers Herschbach and Lee were awarded the 1986 Nobel prize in Chemistry [146, 147]. This method enables the measurement of both, kinematics and the energy stored in the internal degrees of freedom of the reactants. In combination with velocity map imaging, this method also provides a tool to study bimolecular reactions, like nucleophilic substitution [148, 149].

Another method that is also extensively implemented is the use of cryogenic multipole traps developed in the early 1990s by Dieter Gerlich [150]. These are used for preparing cold and controlled ionic ensembles for studies pertaining to laboratory astrophysics [113, 151], collisional dynamics [149, 152, 153], photodetachment and quantum state-dependent studies [154, 155, 156, 157] and spectroscopic studies [104, 158], including the recent novel experimental observation of a dipole-bound state in C_3N^- [159]. The ions in a multipole trap can be cooled down to the Kelvin regime in all degrees of freedom via collisions with a cryogenic buffer gas like helium [157, 160, 161]. This is a commonly used technique to cool ions, where direct laser-cooling is not feasible and is the current state of the art for cooling anions. However, the final temperature of the ions is limited by the temperature of the buffer gas used, which prompted the use of laser-cooled ultracold atoms as a buffer gas for cooling the ions to the cold and even ultracold temperature regime [54].

With this motivation, the experience on the atom and ion trapping from the respective working groups of Prof. Dr. Matthias Weidemüller and Prof. Dr. Roland Wester, led to the development of a hybrid atom-ion trap, and with that, provided a platform to study interactions of different anions with photons and ultracold atoms. In the former years of our collaboration, early measurements on the electronic quantum state-dependent associative electronic detachment between rubidium atoms in a magneto-optical trap and OH^- anions trapped in an octupole rf trap were reported [162]. The implications of the results observed were also discussed in the context of anion sympathetic cooling.

Subsequently, extensive theoretical investigations on the cooling dynamics of ions via elastic collisions with an ultracold buffer gas were developed, including a discussion on the use of a localized buffer gas in a system, where the mass of the atom is heavier than that of the ion, to facilitate the process of sympathetic cooling [163, 164]. Meanwhile, under the framework of another collaboration with Dr. Milaim Kas at the University of Brussels, Belgium (and later at DESY, Hamburg, Germany) theoretical investigations on the reactive collisions (including the electronic quantum-state dependence) between ultracold rubidium and anions like OH^- and their hydrated counterparts, were developed [85, 86, 165].

In recent years, with vast improvements in the experimental setup and its characterization, the collision dynamics between atomic and molecular anions with photons as well as a localized cloud of ultracold atoms in a dark spontaneous optical trap (darkSPOT) were studied [166]. The previously established technique of photodetachment tomography via a far-threshold laser beam was used to map out the ions' spatial distribution [167], and a new technique was formulated to map the ions' temperature in the translational degrees of freedom [1]. In addition to these insights and diagnostics techniques, several important results were achieved during the framework of this doctoral thesis. Reaction dynamics between atomic O^- and molecular OH^- and $OH^-(H_2O)$ anions with ultracold rubidium were experimentally investigated and their implications on the prospects of anion sympathetic cooling were further explored by studying anion-neutral elastic collisions [2, 3]. New frontiers of cooling molecular anions were also demonstrated by implementing laser-induced forced evaporative cooling, proposed in [92], to cool OH^- anions to the Kelvin regime. It must be noted that, while some details of these results are already published in [168], this thesis will primarily focus on the anion-neutral reactive collisions and the implications of these results on the other processes relevant to the system, will be discussed. This thesis is presented in terms of three peer-reviewed publications, each followed by an additional discussion, and is structured as follows.

1.5 Outline of this thesis

In Chapter 2, the experimental setup of the hybrid atom-ion trap is introduced. Key features of the system are encapsulated and details on the diagnostics of the atom and the ion clouds' spatial distributions via absorption imaging and photodetachment tomography respectively, are discussed. The determination of the fraction of excited rubidium in the atom cloud via fluorescence imaging is also presented followed by a description of the determination of atom-ion reaction rate coefficients.

The diagnostics for mapping the translational temperature of the trapped ions are discussed in Chapter 3. A brief motivation and introduction to the different techniques used for mapping the ion temperatures are presented, followed by the published work on ions' time of flight thermometry. Subsequently, the validity of this technique in a one-dimensional case is analytically discussed. Additionally, the application of this technique is demonstrated for temperature determination of the OH^- ion cloud as it undergoes laser-induced forced evaporative cooling via a far-threshold detachment laser.

With the temperature of the ions quantified, the temporal evolution of the overlap between the atom and the ion clouds co-trapped in the system was determined. This provided us the tool to experimentally measure the reaction rate coefficients as a function of the amount of excited rubidium present in the atomic ensemble. In Chapter 4, the collisional dynamics between molecular anions and ultracold atoms are presented. An introduction to the associative detachment reactions in anion-neutral reactions is discussed, followed by the published work on rubidium and OH^- anions. Subsequently, results of the experimental investigations on the dynamics of $OH^-(H_2O)$ anions with rubidium are presented.

In Chapter 5, the elastic and reactive collision dynamics between atomic O^- anions and rubidium atoms are investigated. Brief insights into the use of hybrid atom-ion traps for state-dependent studies are motivated, followed by the published work on the electronic quantum state-dependent detachment processes. The results of the work are then discussed with their implications on the sympathetic cooling of anions via the rubidium atoms.

Finally, in Chapter 6 the results presented throughout the course of this thesis, including the published works, are summarized. The insights derived are put into the broader context of exploring anion-neutral collision dynamics in hybrid atom-ion traps, followed by a brief outlook on future experiments to advance the exploratory studies on anion-neutral interactions.

CHAPTER 2

HYBRID ATOM-ION TRAP

An introduction to the experimental setup and methods

In this chapter, a concise description of the hybrid atom-ion trap located at the University of Heidelberg is presented. An introduction to the experimental setup and the diagnostic methods used for the characterization and measurement of the dynamics of the ion-atom collisions is given. Firstly, an overview of the complete setup is shown. Additional details about ion and atom trapping are described, along with the well-established diagnostic methods for the determination of their spatial density distributions. A description of the measurements for the atoms' excited-state fraction is discussed followed by the determination of ion-atom overlap and reaction rate coefficients. In this work, only the key aspects of the system directly related to the forthcoming chapters are highlighted. Detailed experimental as well as theoretical descriptions of the system and elaborate details on the components of the setup, can be found in the earlier works from the group in [168, 169, 170, 171].

A section view of the experimental setup is shown in Figure 2.1. The different components of the ion production, trapping and detection stages are highlighted along with the description of atom trapping and detection laser transitions.

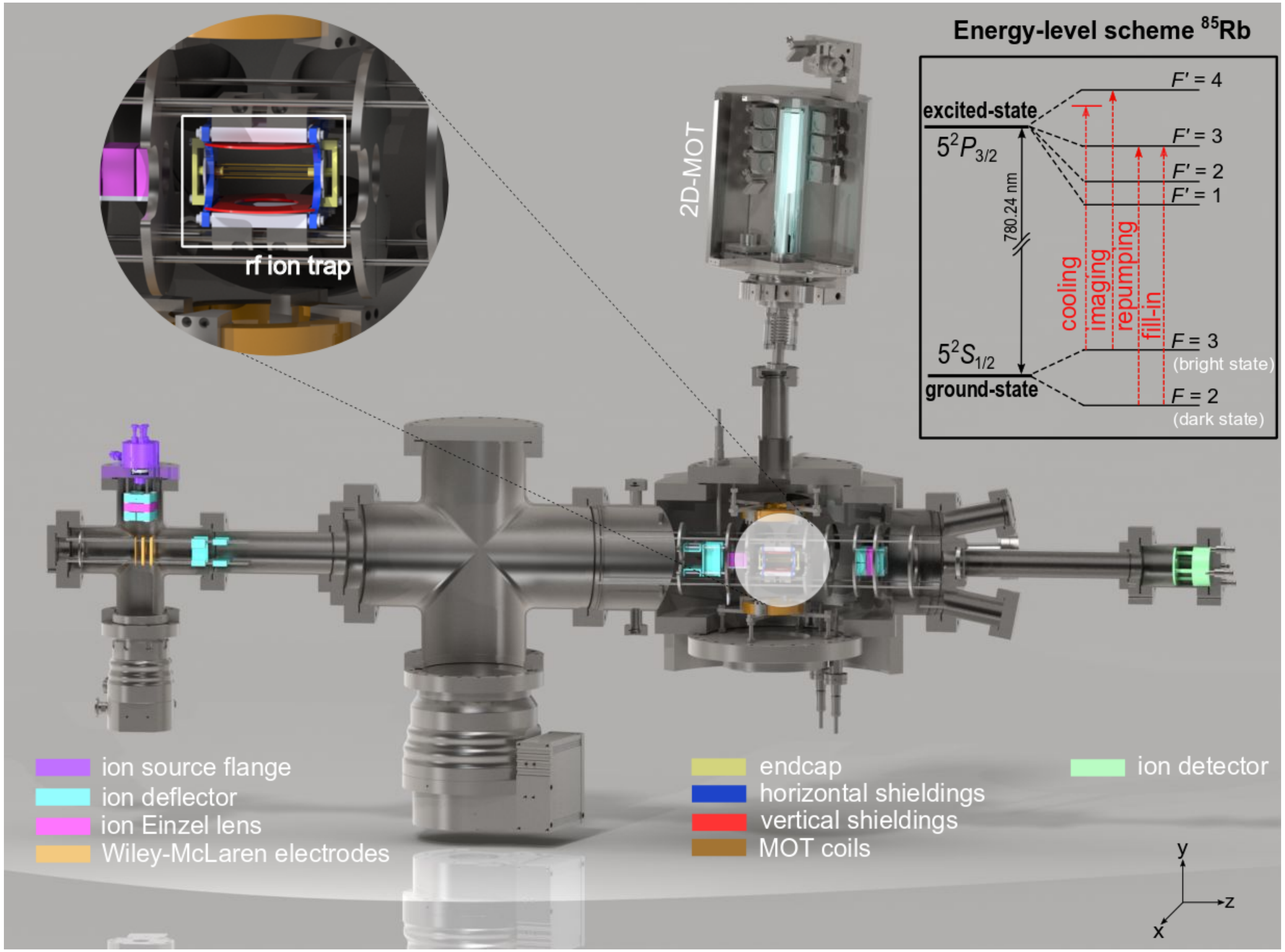
rf ion trap
2D-MOT
Energy-level scheme ^{85}Rb
excited-state
$5^2P_{3/2}$
780.24 nm
$5^2S_{1/2}$
ground-state
F′ = 4
F′ = 3
F′ = 2
F′ = 1
F = 3
(bright state)
F = 2
(dark state)
cooling
imaging
repumping
fill-in
ion source flange
ion deflector
ion Einzel lens
Wiley-McLaren electrodes
endcap
horizontal shieldings
vertical shieldings
MOT coils
ion detector
y
z
x

Figure 2.1: Section view of the hybrid atom-ion trap experiment. The main components of the setup are marked in different colors. The zoom-in shows the octupole rf ion trap. With the available optical access (due to the use of wires), an ultracold atom cloud is created at the center of the ion cloud. The energy-level scheme for ^{85}Rb depicting the different laser transitions used for trapping and detection is also shown.

2.1 Anion production, trapping, and extraction

The ions are created with a pulsed piezo-controlled valve producing a supersonic expansion of a gas pulse that is ignited, subsequently creating a plasma discharge. The ion source is based on the designs illustrated in [172, 173] and has been adapted over the years as discussed in [168, 169, 174, 175]. Due to the dissociative electron attachment happening within a supersonic jet, not only the charged molecules of the gas species used are created but also their charged fragments, as well as small clusters can be produced and studied. A gas reservoir is used that can be filled with a carrier gas of choice, and if required can also be mixed with another gas depending on the ions of interest. The species intended to be studied in our setup, primarily O^-, OH^-, and different order clusters of hydrated hydroxide $OH^-(H_2O)_l$ anions (where $l \in \mathbb{N}$) are produced via argon gas seeded with water vapor at room temperature. Once the gas is injected, it is followed by a pulsed plasma ignition, which creates enough accelerated free charges that result in the production of the desired anions in the source. After the creation of the ions, ion optics consisting of a combination of ion deflectors and Einzel lenses are used to guide the ions, towards the mass-selection stage. Depending on their mass-to-charge ratio, the ions are separated in their time of flight (TOF), as they are accelerated through stages of linear electric fields. This mass spectrometer is based on the design by Wiley and McLaren [176] and for mass m and charge q, the ions' total time of flight is characterized as [168, 175]:

$$t_{\mathrm{TOF}} \propto \sqrt{\frac{m}{q}} \tag{2.1}$$

This acceleration stage is further followed by another group of ion optics, to guide and focus the ions into the trap. With the ions separated in the time domain, the final selection of the ion species that is loaded into the trap is done by pulsing the deflector before the trap as well as adjusting the opening time of the entrance endcap.

Thus, mostly ions of a single m/q ratio are loaded into the octupole radio-frequency wire trap. The use of wires instead of hyperbolic or cylindrical electrodes provides optical access for the laser beams required for the creation of laser-cooled ultracold atoms. Secondly, a multipole trap provides a large field-free region where the rf-induced heating of the ions, when undergoing elastic collisions with buffer gas, is suppressed [138]. As the ions enter the trap, the trap is homogeneously filled with a pulse of helium gas at room temperature to increase trapping efficiency as well as allow thermalization of the ion ensemble. The collisions with the helium buffer gas also ensure that the ions are in their vibrational ground state.

The ion trap consists of eight gold-coated molybdenum wires with a diameter of 100 µm. During ion loading, the potential on the entrance hollow endcap is lowered to let the ions pass through, after which the potential is switched to high. The static potential created confines the ions in the axial direction. Two pairs of shielding electrodes are also present in the trap. While the horizontal set acts as potential shaping electrodes to further modify the axial potential, the vertical set provides shielding against the grounded magneto-optical trap's coils. In the radial direction, the effective potential V_{eff}, is described as [138]:

$$V_{\text{eff}}(\vec{r}) = \frac{q^2 n^2 U_{\text{rf}}^2}{4m\omega^2 r_0^2} \left(\frac{r}{r_0} \right)^{2(n-1)} \tag{2.2}$$

where n is the pole order ($n = 4$ for an octupole trap), U_{rf} and ω is the rf-field amplitude and angular frequency respectively. The inscribed radius of the trap electrodes (or wires) is given by r_0. Thus, while the axial spatial distribution of the ions is dictated only by the static voltages applied to the electrodes, the distribution in the radial direction is influenced by the mass of the ion, where the heavier ions will radially be spread out farther away from the center of the trap.

After the ions are trapped and initialized with the helium gas at room temperature, they can either be overlapped with ultracold atoms or subjected to a laser beam. After interaction with the atoms or photons for a given amount of time, the ions are then extracted onto the detector, which in our setup is a multi-channel plate (MCP). The extraction potential landscape is modified (as in the Wiley-McLaren mass spectrometer) to decrease the ions' time of flight broadening caused by the initial ion spread in the trap to first order. An analysis of the ions' time of flight distribution allows a mapping of the trapped ions' translational temperature and their time of flight to the detector. The investigations on such a TOF thermometry of ions in a multipole trap are presented in detail in Chapter 3.

2.2 Creation of an ultracold atom cloud

Laser cooling of atoms via red-detuned laser radiation and their subsequent trapping via position-dependent forces within a magnetic quadrupole field, in a magneto-optical trap (MOT), is a well-established technique to create an ultracold cloud of atoms [177]. In our experiment, the atomic species of interest is rubidium 85 (^{85}Rb). The transition for the optical cooling is characterized by the D$_2$ line, i.e., $|5^2S_{1/2}, F = 3\rangle \rightarrow |5^2P_{3/2}, F' = 4\rangle$, and the laser beam addressing this transition is called as "cooling" light. However, due to finite widths of transitions and lasers, it is also possible that some of the atoms are excited into the $|5^2P_{3/2}, F' = 3\rangle$ level from where they can spontaneously decay to the lower ground state $|5^2S_{1/2}, F = 2\rangle$. This is also termed as "dark state" as the atoms that fall into this state, are lost from the cooling cycle. In order to cool these atoms, an additional laser beam addressing the transition $|5^2S_{1/2}, F = 2\rangle \rightarrow |5^2P_{3/2}, F' = 3\rangle$ is employed and is termed as the "repumping" light. The atoms are cooled and trapped via the intersection of three sets of counter-propagating laser beams and the magnetic fields created by coils in an anti-Helmholtz configuration, to create a three-dimensional (3D) MOT. Additional sets of compensation coils are used in the three dimensions to tune the zero of the magnetic field, also allowing the possibility to spatially move the atom cloud.

In addition to mitigating the atom losses, firstly due to two-body collisions between excited-state and ground-state atoms and secondly due to reabsorption of spontaneously emitted photons, the atom trap in our setup is employed in the dark spontaneous force trap (darkSPOT) configuration [166, 178]. In this case, the intensity of the repumping light is spatially reduced in the center of the atom trap. Thus, the atoms that fall into the dark state, cannot be addressed by the cooling light resulting in an increase of the atom cloud density. In order to ensure an efficient loading rate of the atom cloud, the atoms are loaded into the 3D-MOT via a 2D-MOT [179]. The rubidium vapors are emitted into the glass cell via a rubidium source dispenser and employing the principles of laser cooling, the atoms are loaded into the 2D-MOT which then provides a high flux of atomic beam pre-cooled in two dimensions. The atoms leave the 2D-MOT towards the main chamber via a differential pumping stage, with velocities lower than the capture velocity required for a 3D-MOT [179]. In the setup, it is possible to alternate between the MOT and darkSPOT configuration via an additional "fill-in" laser beam (which is at the same transition as repumping light but can be independently controlled). All anions will undergo reactions with the excited state rubidium, but for the ground state rubidium, several anions show a very low reactivity. Thus, the possibility to tune the number of atoms in the dark state in the darkSPOT, is of key importance in the system as it enables the study of electronic state-dependent ion-atom reaction dynamics.

2.3 Ion-atom diagnostics

Once we have created the ion and atom clouds co-trapped in the same setup, they undergo different kinds of collisions. In order to characterize the dynamics of these processes, it is important to map the spatial density distributions of the two collision partners. In this section, we briefly describe the techniques of photodetachment tomography and saturation absorption imaging to determine the ions' and atoms' spatial density profiles.

2.3.1 Photodetachment tomography for anions

Experimentally, the ions' spatial density distribution is determined via photodetachment tomography [167, 180]. A laser beam with wavelength $\lambda = 660$ nm ($E_\gamma = 1.88$ eV) and beam waist $\omega_0(1/e^2) \approx 180\,\mu$m is used to detach the electron from the O^- and OH^- ions, which have the electron affinities of 1.46 eV and 1.83 eV, respectively. For other species photon energies (E_γ) larger than the electron affinity of the trapped anion species are required. For the spatial tomography of $OH^-(H_2O)$ anions with a photodetachment threshold at 2.95 eV, a laser beam at $\lambda = 405$ nm ($E_\gamma = 3.06$ eV) is used.

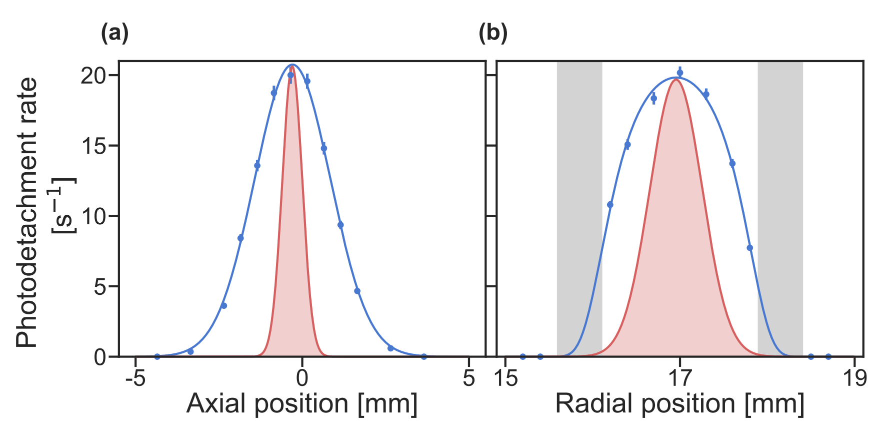

Figure 2.2: Spatial density distribution of O^- ions obtained via photodetachment tomography. The points are the experimental measurements. For comparison of the relative sizes of the atom and the ion clouds, a typical atom distribution is shown in red (for illustrative purposes only). (a) The ions' axial distribution as a function of the axial position of the laser beam. The solid line corresponds to a fit from Equation 2.4, yielding $\sigma_{I,z} = 1.14(1)$ mm. The zero position represents the trap center. The ions are shifted due to the surface charges present on the wire mounts [1]. (b) The ions' radial distribution is shown, integrated along the propagation direction of the photodetachment light. The solid line corresponds to Equation 2.5. This gives $\sigma_{I,r} = 0.700(7)$ mm. The grey regions correspond to the area blocked by the trap wires.

The ion loss rate k_{pd} obtained at a particular position of the laser r_L at the ion cloud, is directly proportional to the column density of ions $\rho_c(r_L)$. The change in the ion number N_I, is described as [167]:

$$\dot{N}_I = -k_{pd}(r_L)\cdot N_I \tag{2.3}$$

where $k_{pd} = [\sigma_{pd}\Phi_L\rho_c(r_L) + k_{bgd}]$. Here, the total photdetachment cross-section and total photon flux is defined as σ_{pd} and Φ_L respectively and k_{bgd} is the background loss rate due to collision of ions with the residual buffer gas. The results of the spatial density distribution of O^- ions, with the laser beam, coupled into the trap, orthogonal to the azimuthal axis, are presented in Figure 2.2.

The spatial ion distribution in the axial direction is governed by the harmonic potential, resulting in a Gaussian shaped distribution, such that:

$$\rho_c(z) \propto \underbrace{\cdot \exp\left(-\frac{(z-z_0)^2}{2\cdot\sigma_{\mathrm{I},z}^2}\right)}_{Axial} \tag{2.4}$$

In the radial direction, the effective potential following r^6-behaviour, governs the spatial distribution and is determined by integrating over the transverse photodetachment axis such that:

$$\rho_c(y) \propto \underbrace{\int_{-\infty}^{\infty} \exp\left(-\frac{(x^2+(y-y_0)^2)^{6/2}}{8\cdot\sigma_{\mathrm{I},r}^6}\right) dx}_{Radial} \tag{2.5}$$

In the above equations, the spatial width in the axial and radial direction as defined as $\sigma_{\mathrm{I},z}$ and $\sigma_{\mathrm{I},r}$ respectively. Also, the center of the ion cloud in the axial and vertical direction are given by z_0 and y_0 respectively.

2.3.2 Atom distribution via saturation absorption imaging

The darkSPOT configuration of the atom cloud leads to an enhanced atom cloud density, due to the reduction of the radiative pressure and collisional losses.

In such an optically dense cloud, the optical pumping of atoms into the stretched state (here, $m_F = 3$) to create a two-level probe transition is not feasible, due to particularly high probe beam intensities required [166, 181]. Consequently, the two-level resonant absorption cross-section, σ_0, no longer holds valid as the effective absorption cross-section for homogeneously distributed Zeeman sub-levels is approximately reduced by a factor $\alpha = \alpha_0(1+4\delta^2)$ (assuming a Lorentzian profile of the absorption cross-section). Here, α_0 is the saturation correction factor on resonance (which must be determined independently in order to determine the optical depth and subsequently the spatial density profile of the atomic cloud), and $\delta = \Delta\omega/\Gamma$ is defined in terms of the detuning of the probe beam (or the "imaging" light) from the atomic resonance $\Delta\omega$, and the natural linewidth Γ of the transition, $|5^2S_{1/2}, F=3\rangle \rightarrow |5^2P_{3/2}, F'=4\rangle$.

The optical depth is calculated as:

$$\text{Optical depth, } od^* = -\alpha_0 \cdot \underbrace{\log\left(\frac{I_{\mathrm{abs}}-I_{\mathrm{bgd}}}{I_{\mathrm{div}}-I_{\mathrm{bgd}}}\right)}_{\text{Optical density,} od_0} + \left(\frac{I_{\mathrm{div}}-I_{\mathrm{abs}}}{I_{\mathrm{sat}}}\right) \tag{2.6}$$

where the image I_{abs} is with atom cloud and absorption beam, I_{div} is without the atom cloud, and I_{bgd} is without both atom cloud and absorption probe beam.

The three pictures are recorded by the camera for each experimental cycle, as shown in Figure 2.3. The saturation intensity of the imaging transition is given as $I_{\text{sat}} = 1.67\ \frac{\text{mW}}{\text{cm}^2}$ [182].

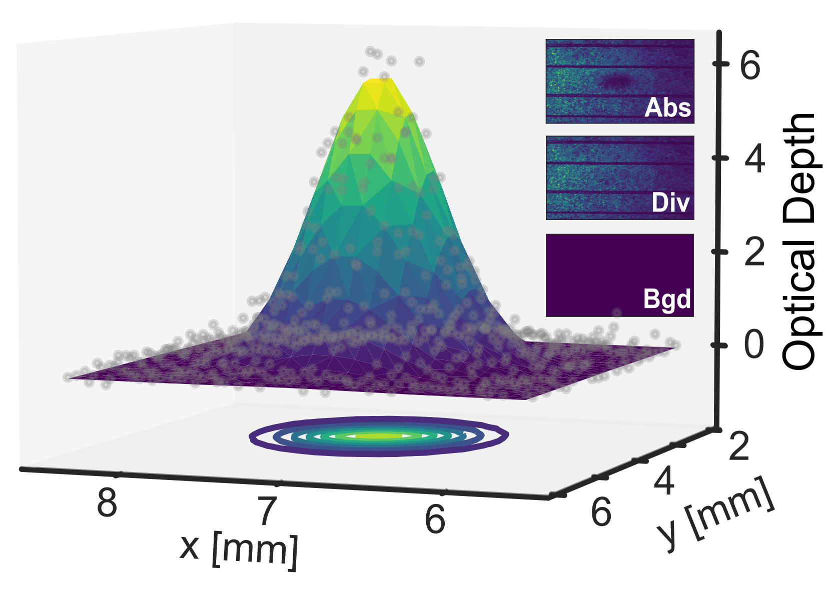

Figure 2.3: Determination of atom density distribution via saturation absorption imaging. The data points represent the optical depth calculated via Equation 2.6 and are fitted with a 2D Gaussian distribution, which gives us the peak optical depth and the spread of the atom cloud in two directions. The raw images recorded by the CCD camera are also shown where **Abs** is the image recorded with both the atom cloud and the probe beam, **Div** is the image with only the probe beam and **Bgd** is the image without the atoms and the probe beam.

For low beam intensities ($I_{\text{div}} \ll I_{\text{sat}}$), the second term in Equation 2.6 can be neglected such that, $od^* \simeq -\alpha_0 od_0$. However, when $I_{\text{div}} \gg I_{\text{sat}}$, the contribution from the intensity term can no longer be neglected and optical depth becomes dependent on the intensity of the probe beam. In order to determine this term, a measurement for the counts recorded on a camera pixel for an incident beam of known intensity for a certain exposure time is performed [171]. This provides a calibration curve between the counts recorded on the camera and the power or intensity of the light incident on it. To prevent the saturation of the camera chip, wavelength-dependent neutral density filters are used and accounted for.

In order to determine the correction factor α_0, the atom cloud is imaged for various intensities of the probe beam (on-resonance). With the beam intensity known, the optical depth is then calculated via Equation 2.6 for different values of α_0. The value of α_0 is chosen as such that the optical depth calculated is independent of the probe beam intensity or in other words the value for which the standard deviation of the optical depth over the entire probe beam intensity range is the minimum. For our system, we determine the saturation correction factor as, $\alpha_0 \approx 3.3$ [168, 171].

For an atom cloud with a Gaussian density profile, the atom number N_A, and atom density ρ_A is calculated as:

$$N = \left(\frac{2\pi\sigma_x\sigma_y od_0^*}{\sigma_0}\right) \tag{2.7}$$

$$\rho_A = \left(\frac{od_0^*}{\sqrt{2\pi}\sigma_z\sigma_0}\right) \tag{2.8}$$

where od_0^* is the peak height of the optical depth's 2D-Gaussian fit, σ_i is the spread of the atom cloud in $i-$th direction with $i = x, y, z$. Independent fluorescence measurements from a different angle of view confirmed that the atom cloud is spherical in nature, thus the spread of the atom cloud in the z-direction is approximated as the average of the spread in the other two directions [171]. In the experiment, with independent control of the fill-in laser beam, it is also possible to determine the number of atoms present in the dark state. Without the fill-in, the atoms present in the states $|5^2P_{3/2}, F' = 4\rangle$, $|5^2P_{3/2}, F' = 3\rangle$, $|5^2S_{1/2}, F = 3\rangle$ are imaged, and with the fill-in beam, in addition to the atoms in these states, the atoms in the dark state $|5^2S_{1/2}, F = 2\rangle$ are also addressed by the probe beam, giving us the total number of atoms present in the atomic ensemble. The temporal evolution of the total number of atoms, N_A is described as:

$$N_\mathrm{A}(t) = N_\mathrm{A0} \cdot \left(1 - \exp\left(-\frac{t}{\tau_\mathrm{A}}\right)\right) \tag{2.9}$$

where N_A0 is the peak atom number and τ_A is the loading time of the atom cloud (when approximately 63% of the total atoms are loaded).

2.3.3 Excited state atoms via fluorescence imaging

The fluorescence caused due to the emission of photons from the atoms in the excited state can be obtained by focusing the emitted light onto a CCD camera [171]. This gives the number of atoms fluorescing from the excited state:

$$\mathrm{N}^* = \left(\frac{P_\mathrm{atoms} - P_\mathrm{bgd}}{E_r\gamma\Omega}\right) \tag{2.10}$$

where P_atoms is power measured on the camera (in mW) and P_bgd is the background power without the atoms but with the presence of laser beams, E_r is the photon energy at $\lambda = 780$ nm, γ is the spontaneous decay rate from the excited state to the ground state and $\Omega = \frac{\pi r_\mathrm{lens}^2}{4d^2}$ is the solid angle subtended by the atom cloud at the camera, defined in terms of the radius of the lens used for focusing the fluorescence light r_{lens}, and the distance between the atom cloud and the imaging lens, d.

The excited-state fraction is defined as the ratio between the number of atoms in the excited state N*, i.e., ($|5^2P_{3/2}, F' = 4\rangle + |5^2P_{3/2}, F' = 3\rangle$) to the total number of atoms, determined via fluorescence imaging and saturation absorption imaging respectively. The loading curves for the atom density for two different excited-state fractions are shown in Figure 2.4.

The determination of atom numbers via fluorescence and saturation absorption imaging are the main source of systematic uncertainties in the estimation of excited-state fraction in our setup. These include the error in the calibration of the cameras used, estimation of the collection solid angle, reflection losses, and also in the determination of the laser intensities at the position of the atoms in the trap, particularly for the repumper beam in the dark-SPOT configuration. Another source of error for measuring the atom fluorescence is the scattering of photons by different components of the trap, especially the trap wires. Though these effects are accounted for via background correction of the recorded images, this could still result in a slight overestimation of the number of excited-state atoms. Taking these sources of errors into consideration, we estimate the systematic uncertainty in the experimental determination of excited-state fraction to be ~ 40%.

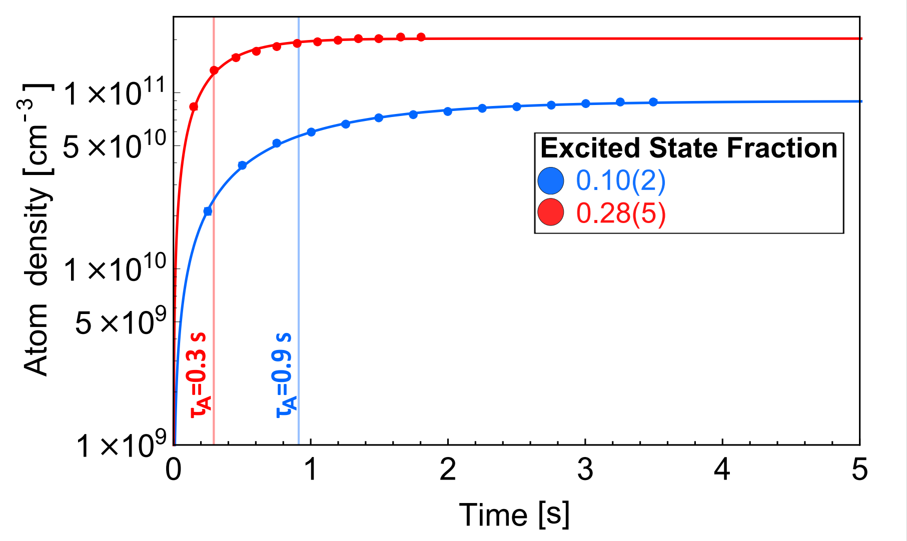

Figure 2.4: Atom density as a function of time. The loading time τ_A, of the atom density distributions is marked via shaded lines for two different excited state fractions 0.10(2) and 0.28(5), shown in blue and red respectively. The points are the atom densities experimentally determined via saturation absorption imaging (from Equation 2.8). The solid lines are the fits corresponding to the Equation 2.9.

In order to compare the population dynamics in our system to those typically observed for atoms in a MOT, we approximate our system as a two-level system, in the context of the model proposed by Townsend *et. al* in [183]. For a two-level atom system irradiated by a monochromatic light source, the population of the excited state, ρ_{ee} is calculated via the optical Bloch equations as:

$$\rho_{\text{ee}} = \frac{1}{2}\frac{\frac{C_1^2\Omega_{\text{tot}}^2}{2}}{\delta^2 + \frac{\Gamma^2}{4} + \frac{C_2^2\Omega_{\text{tot}}^2}{2}} \tag{2.11}$$

where $\Omega_{\text{tot}} = \Gamma\sqrt{\frac{I}{2I_{\text{sat}}}}$ is the Rabi frequency calculated by the average light intensity, I in the optical trap, I_{sat} is the saturation intensity, δ is the detuning of the light beam from the atomic resonance, Γ is the natural linewidth and C_1^2 and C_2^2 are the average Clebsch-Gordan coefficients. With our system approximated as a two-level system with $\delta = 14\,\text{MHz}$, we estimate $C_1^2 = 1.0(1)$ and $C_2^2 = 0.3(1)$, which are in reasonable agreement with the typical values for these coefficients [183].

2.3.4 Determination of reaction rate coefficients

From these diagnostic methods, we determine the time-evolution of the ions' and atoms' spatial density distributions. The interaction with atoms results in the change of ions' density distribution due to a change in its translational temperature as a result of sympathetic cooling via atom-ion elastic collisions. In addition to these collisions, reactive processes induce additional ion losses from the trap. In order to model these reaction dynamics, the atom-ion overlap integral, Φ_{AI}, is defined as (in units of cm^{-3}):

$$\Phi_{\text{AI}}(t) = \int_{-\infty}^{\infty} \rho_{\text{I}}(x,y,z,T_{\text{I}}(t)) \cdot \rho_{\text{A}}(x,y,z,t)\, dV_{\text{A}} \tag{2.12}$$

where ρ_{I} is the time-dependent ion density changing in accordance with the ions' translation temperature T_{I} and ρ_{A} is the time-dependent atom density evolving analogous to Equation 2.9. It is to be noted that while the ion density distribution was found to be constant in time for the case of Rb-OH$^-$ system, it was significantly altered for both Rb-O$^-$ system and Rb-OH$^-$(H$_2$O) system, making it imperative to account for the time-dependence of the ion distribution, in the determination of the overlap integral.

The change in the normalized ion number $\bar{N}_{\text{I}}$ is given as:

$$\frac{\text{d}\bar{N}_{\text{I}}}{\text{d}t} = -\left(\kappa \cdot \Phi_{\text{AI}}(t) + k_{\text{bgd}}\right) \cdot \bar{N}_{\text{I}} \tag{2.13}$$

with κ the reaction rate coefficient in cm^{3}s^{-1}, k_{bgd} the background loss rate in s^{-1} and $\bar{N}_{\text{I}}$ the normalized ion number. Rearranging the above equation provides:

$$\int_0^t \frac{\text{d}\bar{N}_{\text{I}}}{\bar{\text{N}}_{\text{I}}} = -\int_0^t \left(\kappa \cdot \Phi_{\text{AI}}(t) + k_{\text{bgd}}\right) \text{d}t \tag{2.14}$$

Solving the above differential equation yields:

$$\bar{N}_{\mathrm{I}}(t) = \bar{N}_{\mathrm{I}}^{0} \cdot \exp\left(-\kappa \int_{0}^{t} \Phi_{\mathrm{AI}}(t')dt'\right) \cdot \exp(-k_{\mathrm{bgd}}t) \tag{2.15}$$

where $\bar{N}_{\mathrm{I}}^{0}$ is the initial ion number (normalized to 1) at time $t = 0$. With all the other parameters pre-determined, the observed ion losses as a function of interaction time with the atoms can be fitted with Equation 2.15, yielding the only fit parameter, the reaction rate coefficient κ for a given configuration of the system. In our work, we have extensively explored the dependence of the reaction rate coefficients on the fraction of excited rubidium in the atomic ensemble, for different atom-ion systems. These results would be discussed in detail in Chapter 4 and Chapter 5. However, the only thing missing in our diagnostics of the atom-ion systems is the determination of the ions' translation temperature, which is discussed in detail in the following chapter.

CHAPTER 3

THERMOMETRY IN A MULTIPOLE TRAP

In this chapter, a thermometry method for the determination of the trapped ions' temperature in a multipole radio-frequency trap, is described. Firstly, the motivation and the existing diagnostic techniques to obtain the temperature of a trapped ionic species are discussed. This is followed by the published work on determining the trapped ions' translational temperature by mapping it onto their time-of-flight (TOF) to the detector. Subsequently, the validity and limitations of the linear mapping of ions' temperature onto the variance of their TOF distribution, is analytically discussed. Finally, the application of the thermometry technique is demonstrated by estimating the temperature of OH^- anions as they undergo laser-induced forced evaporative cooling from temperatures above room temperature down to the Kelvin regime.

3.1 Motivation for temperature diagnostics

Multipole radio frequency ion traps are pivotal in the study of trapped ions and their interactions with other neutral and charged particles [138]. These include research of laser-induced processes [92, 184, 185], spectroscopic studies [186, 187, 188, 189, 190], and ion-neutral elastic [63, 191], inelastic [192, 193] and reactive [66, 153] collision dynamics. One of the pre-requisites to investigate these interactions in a well-controlled environment, is the accurate determination of the ions' spatial and energy distribution.

The most frequently used methods to determine the ion temperature in a multipole trap involve the measurement of temperature-dependent coefficients like ion mobility or reaction rates [194, 195], and performing spectroscopic studies to resolve Doppler profile [37, 196, 197]. The fluorescence created by the ions can be imaged by a CCD camera to image the ions' distribution, but for most molecular anions, the latter is not feasible particularly due to the lack of closed optical transitions or efficient probing schemes. While near-threshold photodetachment techniques to estimate the internal temperature for such molecular anions exist [192], the rethermalization of the ions with the surrounding black-body radiations might result in different rotational and translational temperatures. The estimation of the temperature of an ion in a radio-frequency (rf) multipole trap is a non-trivial process [198]. The dimensions of the trap may also influence the energy distribution of the ion ensemble, along with its coupling to the trap imperfections [199] as well as the background residual gas and the rf-induced micromotion [200]. These effects can further manifest themselves in the emergence of non-thermal behavior exhibited by the ion ensemble [201, 163]. Thus, in order to completely characterize the ion distribution, it is imperative to devise a versatile, time-efficient method to determine the ions' translational temperature in a multipole trap.

3.2 Thermometry in a multipole ion trap

In our system, we study the interaction of anions with photons and laser-cooled ultracold atoms to investigate anion cooling as well as anion-neutral reactive processes. To model and understand the dynamics of these processes, it is necessary to accurately determine the temperature of the trapped ions. A detailed investigation to model the ion trap's potential landscape as well as to study the influence of trap geometry and imperfections on the ion distributions is performed and the results are presented in the following publication.

The work is published under the framework of our collaboration with the group of Prof. Dr. Roland Wester from the University of Innsbruck. Markus Nötzold and I are the shared first authors of this published work as also stated in the article. I contributed to the experimental measurements on tomography and was also involved in the analysis and discussions on the COMSOL simulations, for investigating the ion dynamics in a multipole trap. I was also responsible for the preparation and communication of the final manuscript [2], published in the journal Applied Sciences (see Permission).

Title: **Thermometry in a Multipole Ion Trap**

Authors: Markus Nötzold, **Saba Zia Hassan**, Jonas Tauch, Eric Endres, Roland Wester Matthias Weidemüller.

Published in: Appl. Sci. **10**(15), 5264 (2020).

applied sciences

MDPI

Article

Thermometry in a Multipole Ion Trap

Markus Nötzold [1,†], Saba Zia Hassan [2,†], Jonas Tauch [2], Eric Endres [1], Roland Wester [1] and Matthias Weidemüller [2,*]

[1] Institut für Ionenphysik und Angewandte Physik, Universität Innsbruck, Technikerstraße 25, 6020 Innsbruck, Austria; markus.noetzold@uibk.ac.at (M.N.); eric.endres@uibk.ac.at (E.E.); roland.wester@uibk.ac.at (R.W.)

[2] Physikalisches Institut, Ruprecht-Karls-Universität Heidelberg,Im Neuenheimer Feld 226, 69120 Heidelberg, Germany; hassan@physi.uni-heidelberg.de (S.Z.H.); tauch@physi.uni-heidelberg.de (J.T.);

* Correspondence: weidemueller@uni-heidelberg.de; Tel.: +49-6221-54-19470

† These authors contributed equally to this work.

Received: 3 July 2020; Accepted: 27 July 2020; Published: 30 July 2020

Featured Application: In this work, we present a versatile method to determine the translational temperature of ions trapped in a multipole ion trap. The temperature of the trapped ions is mapped onto their time of flight to the detector. Unlike other ion-thermometry techniques, e.g., Doppler spectroscopy, this method is time-efficient and can be applied to any ionic species, without relying on the availability of suitable optical transitions.

Abstract: We present a characterization of the ions' translational energy distribution in a multipole ion trap. A linear mapping between the energy distribution of the trapped ions onto the ions' time-of-flight (TOF) to a detector is demonstrated. For low ion temperatures, a deviation from linearity is observed and can be attributed to the emergence of multiple potential minima. The potential landscape of the trapped ions is modeled via the finite element method, also accounting for subtleties such as surface-charge accumulation. We demonstrate the validity of our thermometry method by simulating the energy distribution of the ion ensemble thermalized with buffer gas using a Molecular Dynamics (MD) simulation. A comparison between the energy distribution of trapped ions in different multipole trap configurations—i.e., with hyperbolic rods, cylindrical rods, and cylindrical wires—is provided. With these findings, one can map the temperature of the trapped ions down to the Kelvin regime using their TOF distributions. This enables future studies on sympathetic cooling and chemical reactions involving ions in multipole traps.

Keywords: multipole ion traps; wire traps; ion thermometry; ion tomography

1. Introduction

Developments in the field of trapped particles have enabled the exploration of dynamical processes under the action of diverse short-range and long-range interactions. A detailed characterization of the spatial distribution and energy distribution of these trapped particles is imperative to investigate phenomena in ultracold chemistry [1–8], astrophysics [9], as well as astrochemistry [10], including the formation and evolution of the interstellar medium (ISM) [11–15]. For charged particles trapped in multipole ion traps, the measurement of temperature-dependent ion mobility and rate coefficients is one of the key methods to characterize the temperature of the ions [16]. With advances in the application of electrostatic lenses, another method called velocity map imaging became feasible such that ions with same initial velocity in the trap could be mapped onto the same point on the detector [17]. Similar to atoms, the phase space distribution of the trapped ions with closed optical transitions can also be characterized via Doppler-spectroscopy [18–23]. However, this is limited to only a number of atomic cations. In case of molecular anions, a detailed characterization for the internal thermometry via photodetachment techniques exists [24]. However, due to the rethermalization of the ions with the black-body radiation, the temperature of ions in the external and internal degrees of freedom are not necessarily the same. Recent work [25] measured the translational temperature of hydroxyl (OH^-) anions via the Doppler width of an overtone transition, but this method is time-intensive and requires an exact knowledge of the overtone transition frequency.

In this work, we put forward a versatile tool to characterize the translational temperature of ions trapped in a multipole ion trap by mapping the ions' time-of-flight (TOF) to the detector. Here, we describe an octupole radio frequency (rf) wire trap in a Hybrid Atom–Ion trap (HAI-trap) setup. We start by detailing the experimental setup and the ion trap assembly in Section 2 and Section 3, respectively. The current setup is an improved version of the earlier design described in [26]. Following the description of the trap, we investigate the potential landscape created by a multipole wire trap and traps with ideal cylindrical or hyperbolic rods in Section 4. We further compare the influence of different trap geometries on the final energy distribution of the trapped ions after interaction with a buffer gas. Then, in Section 5, we extend our investigations to the HAI-trap setup, where the 3-dimensional (3D) model of the system is used to simulate potential landscape in the trap, including surface charges that accumulate on the plastic components of the trap. The ion distributions obtained via the simulated potentials are compared with the measured ion distributions obtained via photodetachment tomography [27,28]. It is shown that the spatial energy distribution of ions in the trap can be mapped onto the ions' time-of-flight to the detector, including the effect of multiple regions of potential minima that arise in multipole ion traps (with the pole order > 2). Independent of the trapped ionic species, this technique is time-efficient and can be applied to any system without relying on the existence of suitable transitions for determining the ions' motional temperature.

2. Overview of the Experimental Setting

A schematic representation of our experimental setup is shown in Figure 1. The ion source consists of a pulsed piezo valve, which injects a gas pulse into the vacuum system. In the current setup, a modified version of the design introduced by [29] is used. By actively controlling the discharge voltage and the gas flow into the vacuum chamber, a variety of ionic species can be created depending on the gas mixture used. Our benchmark system is the hydroxyl anion, which serves as our system of interest for the rest of this work. For the creation of hydroxyl anions, argon gas mixed with water vapor is used in the reservoir before the nozzle of the gas inlet. As the ions exit the source, they are guided via ion optics towards a Wiley–McLaren-based time-of-flight mass spectrometer, which is operated in a pulsed mode. Here, the ions are accelerated orthogonally with respect to their initial trajectory and are then separated in the time domain based on their mass-to-charge ratio. The ions are then focused through a pinhole into the next chamber where they are loaded into an octupole wire trap.

The trap assembly is explained in detail in Section 3. A 3-dimensional (3D) model of the wire trap is illustrated in Figure 2a, and a qualitative representation of the potential during loading, trapping, and extraction of the ions is shown in Figure 2b. The mass selection of the ions is done by switching the entrance endcap of the trap between a high and low potential in order to load the desired species. As the ions approach the trap, the entrance endcap electrode is set to a lower potential. Once the ions enter the trap, the entrance endcap electrode is switched to a higher potential, thus confining the ions in the trap axially.

In order to increase the trapping efficiency of the ions, a pulse of helium buffer gas is injected into the trap. This not only greatly enhances the number of ions trapped, but also ensures that the hot ions produced from the plasma discharge source are properly thermalized and lie in their vibrational ground state. This serves as the starting condition for the ion ensemble which can then be overlapped with a cloud of laser-cooled rubidium atoms. The implementation and characterization of the atom trapping setup is detailed in [30]. Additionally, a far-threshold laser beam can be shone onto the ions in order to characterize their spatial density distribution via photodetachment tomography [27].

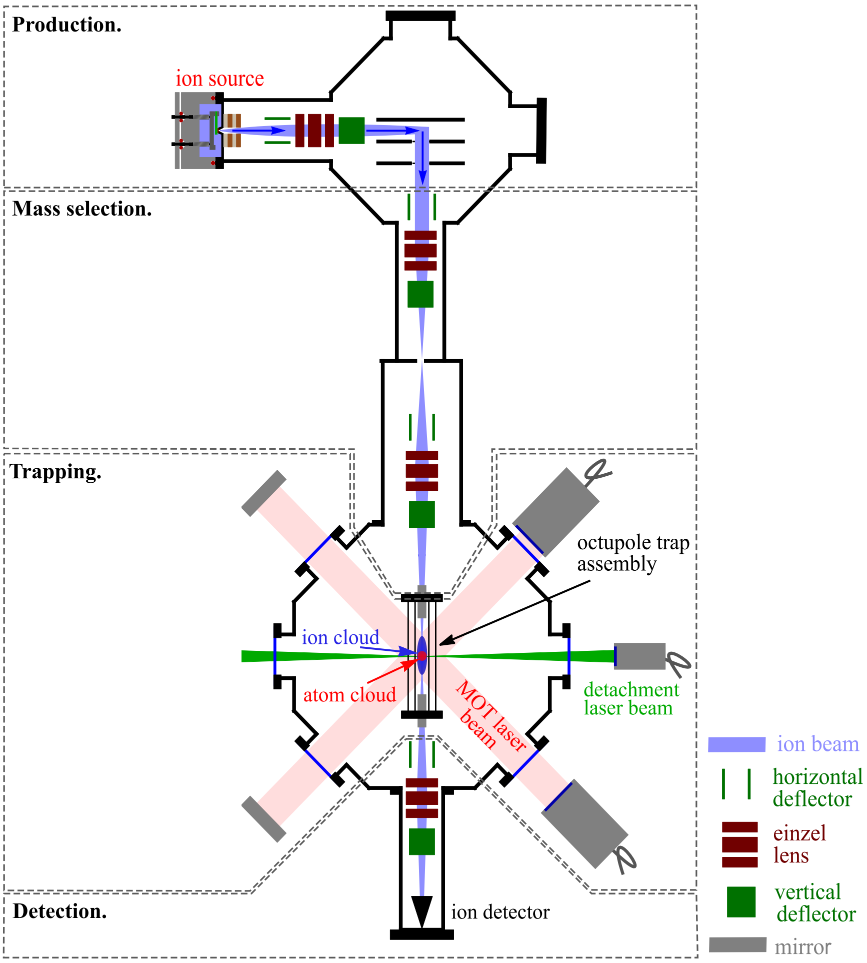
Production.
ion source
Mass selection.
Trapping.
octupole trap assembly
ion cloud
atom cloud
MOT laser beam
detachment laser beam
Detection.
ion detector
ion beam
horizontal deflector
einzel lens
vertical deflector
mirror

Figure 1. Schematic representation of the Hybrid Atom–Ion Trap (HAI-trap). The ions are produced via a plasma discharge in a pulsed molecular beam and are then guided towards a Wiley–McLaren time-of-flight spectrometer, where the ions are separated according to their mass-to-charge ratio. The ion beam is then guided into the trap, and the entrance endcap is switched to mass-select the desired species. Subsequently, the ions can be overlapped with a cloud of laser-cooled atoms to study atom–ion interactions, or a detachment laser beam can be shone onto the ion cloud for photodetachment tomography. Finally, the ions are extracted via the hollow endcap onto a detector that records the ions' arrival time.

Depending on the nature of the experiment, the ions can be confined in the trap for varying amounts of time. The interaction with laser-cooled atoms and/or a laser beam results in the change of the ions' energy distribution which is recorded by extracting the ions from the trap and measuring the spread in the TOF distribution. The ions are extracted by lowering the potential on the exit endcap electrode and exit shielding plate close to the detector. Furthermore, the entrance shielding plate is switched to a higher potential to facilitate an additional acceleration of the ions towards the ion detector. In our case, a microchannel plate (MCP) is used to detect the arrival time of the individual ions. It is imperative to note that the ion detector counts single ion events, and does not integrate the signal. This is critical for comparing the measured ion distributions to those obtained from the simulations. (An integrator would introduce an additional broadening of the detected distribution). The width of this TOF distribution recorded on the detector can provide a direct mapping to characterize and quantify ions' energy distributions.

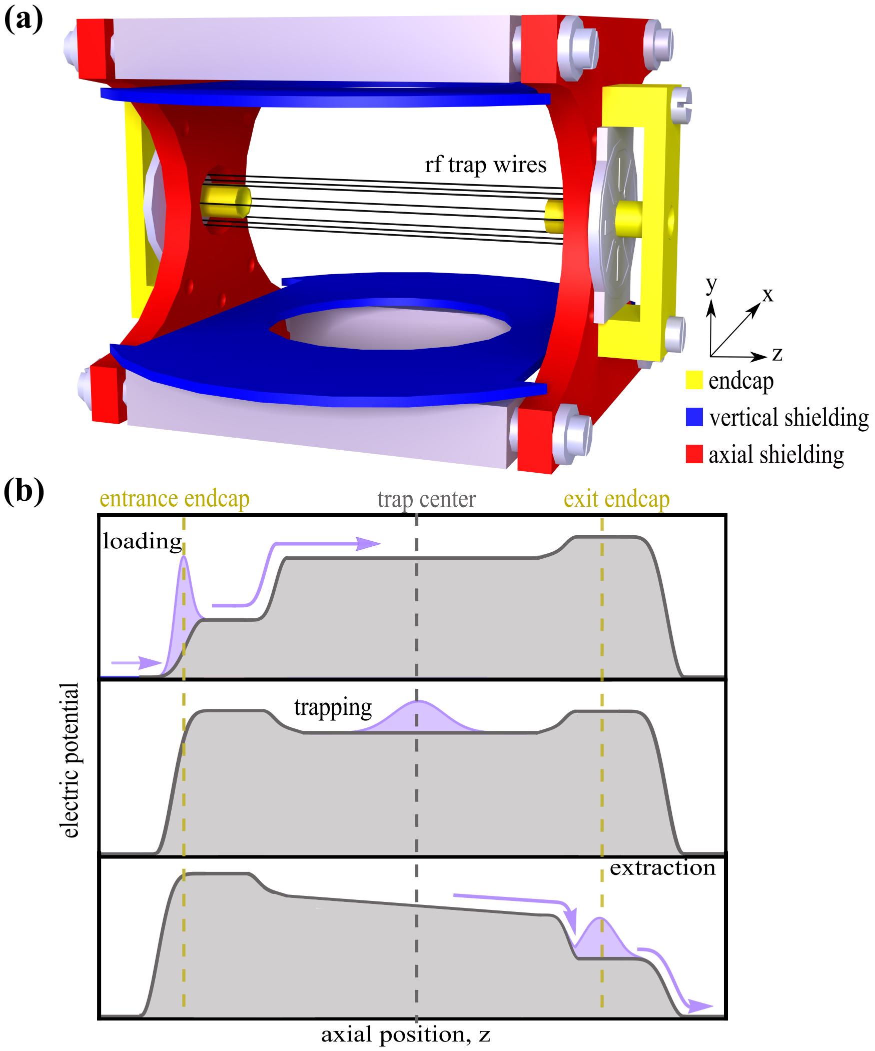
(a)
rf trap wires
y
x
z
🟨 endcap
🟦 vertical shielding
🟥 axial shielding
(b)
entrance endcap
trap center
exit endcap
loading
trapping
extraction
electric potential
axial position, z

Figure 2. Description of the ion trap. (**a**) A 3D model of the ion trap is shown with an illustration of the radio frequency (rf) trap wires, endcap electrodes, and shielding plates used in the setup. (**b**) A qualitative description of the electric potential as a function of the position along the trap's main axis during three different stages. Firstly, the loading of ions from the source into the trap. Secondly, the axial confinement of ions. Finally, the unloading of ions from the trap to be further extracted onto the detector.

3. Description of the Ion Trap

The 3D model of the trap assembly is shown in Figure 2a. The octupole trap consists of eight gold-coated molybdenum wires with a diameter of 100 µm. They are symmetrically placed around the trap axis on a circle with radius of 3 mm. The wires are soldered onto a printed circuit board (PCB). A radio-frequency field is applied to the trap wires, along with an additional static voltage as an offset. The offset chosen corresponds to the voltages used in the Wiley–McLaren acceleration stage, which lowers the kinetic energy of the incoming ions such that the trapping potential can confine them. While the static voltage applied to the endcap electrodes provides axial confinement to the ions, the radio-frequency field applied to the wires confines the ions radially, such that the ions experience a position-dependent field proportional to r^{2n-2}, where n is the pole order of the ion trap, with $n = 4$ for an octupole trap. The potential that the ions experience governs their spatial density distribution. Thus, while they are Gaussian-distributed in the axial direction due to the harmonic potential in this direction, they are described by a super-Gaussian distribution of order six in the radial direction [31].

The total potential exhibits a local maximum at the center of the trap along with off-center minima [32]. While the endcaps create a necessary confining potential in the axial direction, they also create a deconfining potential in the radial direction, which exhibits r^2 dependency close to the center [33]. This is a feature common to all multipole traps with $n > 2$, and not only to octupole wire traps, thus creating multiple regions of local minima called "pockets".

In addition to the rf wires and endcap electrodes, the trap consists of a set of vertical and axial shielding plates. The vertical shielding plates prevent the grounded MOT coils (not shown) from pulling down the potential in the trap center. The hole in the plates provide optical access for laser beams to create an MOT. The axial shielding plates provide the flexibility to shift the ion cloud during trapping or giving them additional acceleration during extraction, thus increasing the detection efficiency. The axial shieldings are important for controlling the slope of the potential during extraction, as seen in Figure 2b. The voltages applied to the endcap electrodes and shielding plates are optimized such that the trapped ion cloud is initially exposed to a linear acceleration region during extraction. This is necessary for obtaining a symmetric TOF spread. Additionally, the axial shieldings can also be used to modify the potential topology for the extraction process to enhance the mass resolution of the system. This is particularly useful for exploring systems with higher masses, where multiple ionic species are simultaneously trapped.

A wire trap offers the advantage of providing optical access for laser beams for hybrid atom–ion experiments, and an octupole trap provides a large central field-free region where the influence of radio-frequency heating is reduced. However, one feature of wire traps that needs to be noted while designing a trap assembly is that all nearby electrodes and grounded plates will influence the potential, in the region enclosed by the wires, drastically. This effect is diminished for a trap using thicker rods, as the penetration of outer electrodes is greatly reduced.

As opposed to the traps with wires, the ones using ideal cylindrical rods and hyperbolic rods are mechanically more robust. The large size difference between wire and rod traps raises the question of how the potential landscape deviates in these different types of trap. To understand the differences in the potential between a wire trap and the more commonly used multipole trap consisting of thicker cylindrical rods, a detailed comparison between traps with wires and cylindrical or hyperbolic rods is subsequently described in Section 4.

4. Comparison between Wire and Rod Traps

In order to describe the confining potential created by an rf field and the physics governing the dynamics in an ion trap, the adiabatic approximation is used. Here, the ion motion is split into a fast oscillatory motion, also called micromotion; and a slow drift motion in the confining ponderomotive potential, called macromotion. Henceforth, the potential created by rf traps can be expressed as an effective conservative potential (averaged over one oscillation period), given by [34]

$$V_{\text{eff}}(\vec{R}(t)) = \frac{e^2}{2m\omega^2}\langle \vec{E}(\vec{R}(t), t)^2 \rangle. \tag{1}$$

Here, $\vec{R}(t)$ describes the trajectory of the macromotion, $\vec{E}$ is the time-dependent electric field, e is the electronic charge, and m is the mass of the ion. This results in a pseudo-static effective potential, which can approximately describe the ion trajectories in different multipole traps. This approximation allows the comparison between different trap types via a static potential. The three trap types under consideration are the ideal hyperbolic trap, a trap consisting of cylindrical rods, and a trap using wires. A geometric comparison between the trap types is given in Figure 3a.

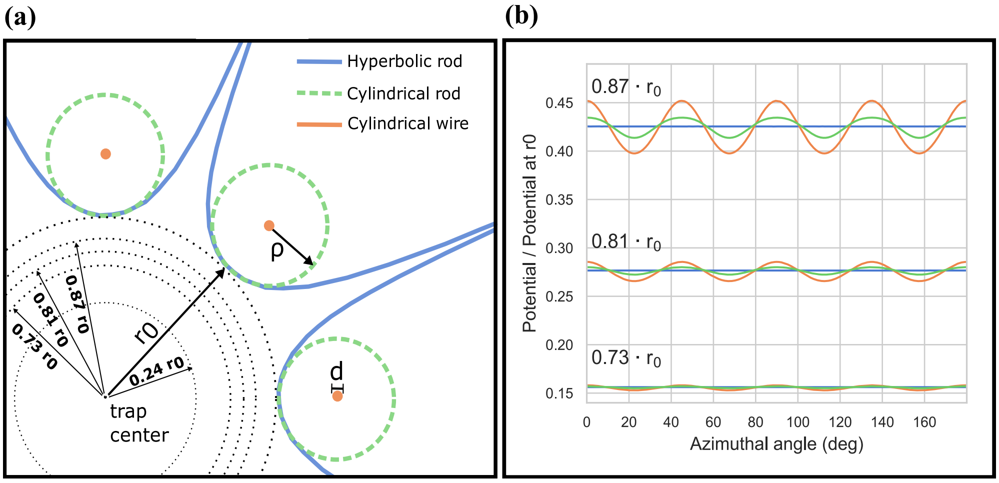

Figure 3. Comparison between different multipole traps. (**a**) True size relations between hyperbolic rods, ideal cylindrical rods, and cylindrical wires are represented. The distance of a hyperbolic rod from the trap center is $r_0 = 2.25$ mm, the diameter of an ideal cylindrical rod is $2\rho = 1.5$ mm and the wire diameter is $d = 100$ µm. The wires are placed concentrically with the ideal cylindrical rods and are located 3 mm from the trap center. (**b**) The effective potential created by hyperbolic rods is shown along with that obtained from a rod and a wire trap with their voltages matched to the same average potential as in the hyperbolic case. It can be seen that the hyperbolic trap potential exhibits true azimuthal angle independence, while distinct maxima/minima in the potential for traps with cylindrical rods or wires can be observed. Additionally, the modulations in a wire trap have a higher amplitude than those in a rod trap. For instance, the amplitude of fluctuations in a rod trap at $0.87 \cdot r_0$ is already attained by a wire trap at $0.81 \cdot r_0$.

In order to replicate the curvature of the ideal multipole potential to first and second order, the radius of the cylindrical rods used must fulfill the following relation [34,35]:

$$\rho = \frac{r_0}{n-1}. \tag{2}$$

For our wire trap with 100 µm diameter wires and a distance from the trap center of 3 mm, the ideal rod diameter is 1.5 mm, which is more than an order of magnitude larger than the wire size, and thus, Equation (2) is far from being fulfilled.

Due to the vast geometric differences between the three mentioned rod shapes, it is not trivial to predict if and how the potential landscape differs in the different trap types. In an attempt to investigate these differences, we used COMSOL Multiphysics to simulate infinitely long traps without endcaps. For details on the COMSOL simulations, see Appendix A. The geometries are chosen as seen in Figure 3a, with the hyperbolic and cylindrical rod trap having the same inscribed radius of 2.25 mm, and the wire trap lying concentrically inside the rod. The simulated electric fields are used to calculate an effective potential via Equation (1) assuming OH^- ions and a trap frequency f of 5 MHz. The resultant potential was then averaged over the azimuthal angle and the voltage was varied until the difference in the average effective potential between the hyperbolic trap and the rod/wire trap was minimized.

As a result, it was observed that in order to match the potential created by hyperbolic rods, the ideal rod trap needs a factor of 1.01, or about a 1% increase in the voltage; while the wire trap needs a voltage 5.4 times higher for the same. Thus, with a suitably higher voltage, it is possible to match the averaged potential. However, the ideal rod trap and wire traps exhibit maxima and minima over the azimuthal angle corresponding to the position of the rods/wires and the space in between them. These results are depicted in Figure 3b. The effective potential for the different trap configurations as a function of the azimuthal angle at three different radii (from the center of the trap) is shown. These radii are also marked in Figure 3a. At each of these radii, it can be seen that the amplitude of modulations in the wire trap exceeds those in the rod traps. Furthermore, these distortions become more prominent as one goes radially outwards in the case of a cylindrical rod/wire trap. As a consequence of these deviations, the minimum voltage for stable trapping of ions increases for a cylindrical rod trap, and is even further increased for a wire trap.

In order to estimate the influence of the deviations from the ideal hyperbolic potential on the temperature of ions in the trap when they encounter a neutral collision partner, a Monte-Carlo buffer gas simulation for all three trap configurations was performed. The voltages used are the same as the ones previously used to match the potential landscape of a hyperbolic trap with 50 V rf amplitude. These simulated, matched voltages are used to calculate the electric field vectors, which are then loaded into a home-built script. Subsequently, the ion trajectories are calculated, and a classical, hard-sphere-based collision model is used to simulate the collisions with a buffer gas. For details on the Molecular Dynamics simulations, see Appendix B. In our case, we investigate the thermalization of OH^- ions with a room-temperature helium buffer gas. The mean speed of the ions is obtained via the Molecular Dynamics (MD) simulations. The resultant energy distribution is demonstrated in Figure 4. The temperature of the ion ensemble T is calculated from the ions' mean speed ($\bar{v}$) as

$$T = \frac{\pi m \bar{v}^2}{8k_\mathrm{B}}, \tag{3}$$

where k_B is the Boltzmann constant (We hereby use Equation (3) to define the notion of temperature, as well as in case of the emerging nonthermal distributions.). In all three cases, a temperature of 366 K was obtained, with the deviations between the traps being < 1 K. The insignificant deviation in the temperature between the different types of traps can be explained via the mean radial extension of ions in the trap which, in the simulations, is $0.24 \cdot r_0$ (also depicted in Figure 3a). This means that the ions primarily explore the innermost region of the trap, and spend only a little time in the outer region of the trap, where the modulations in the effective potential are relatively higher. In Figure 4, the dashed black line represents an analytical Maxwell–Boltzmann distribution at 366 K [36]. Furthermore, it can be inferred that the ions energy distribution is not perfectly described by a Maxwell–Boltzmann distribution and exhibits a nonthermal behavior. The simulated temperature is significantly higher than the temperature of the buffer gas at 293 K. This effect is dependent on the multipole order and is well-investigated in previous works [37], amounting it to the collision of ions in the micromotion-dominated region of the rf trap.

In view of the above results, it can be assumed that the main heating mechanism is the micromotion-dominated rf heating which causes the ions to gain additional energy when colliding in the rf field. In the case of thermalization of ions with a neutral buffer gas at room temperature, the deviations prevalent in the rod or wire trap from the ideal hyperbolic potential can be neglected.

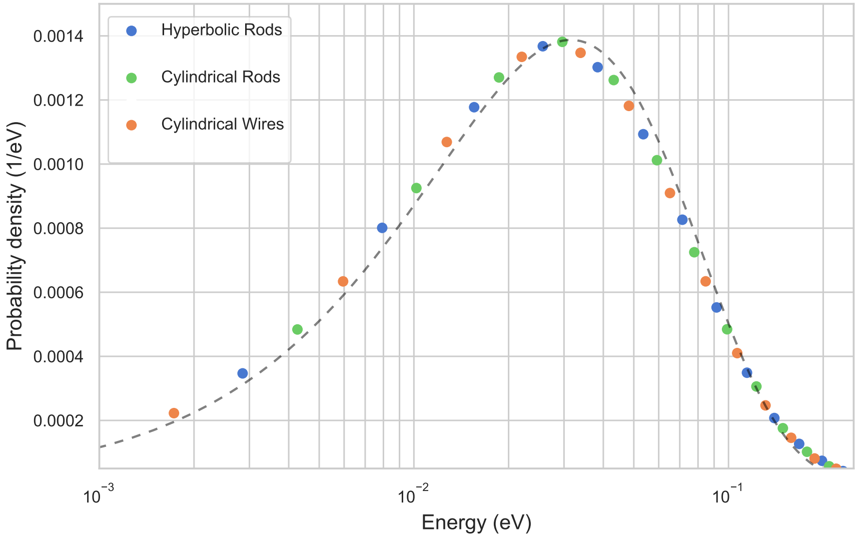

Figure 4. Simulated energy distribution of ions after collisions with helium buffer gas at 293 K for different trap configurations are shown. For traps with hyperbolic rods, cylindrical rods, and wires, the temperature obtained from the distributions are all 366 K, using Equation (3). On comparison with an analytical Maxwell–Boltzmann distribution at 366 K (black dashed line), it can be seen that the distribution is not perfectly thermal.

5. Translational Temperature Determination in HAI-Trap

The mapping of the ion ensemble's energy distribution in the trap onto the TOF spread of the extracted ions demands a more sophisticated model of the setup. Thus, the 3D trap assembly of the HAI-trap experiment with all the electrodes including the endcaps and shieldings, as described in Section 3, are accounted for in the COMSOL simulation. In this section, firstly, the translational temperature of the ions is simulated via an MD simulation. The energy distribution thus obtained is then characterized via a photodetachment tomography of the ions' spatial distribution. The energy and spatial distribution is then used to determine the influence of surface charges that can accumulate on the printed circuit boards (PCBs) in the trap assembly. Subsequently, the mapping of the ions' TOF distribution onto the detector and the obtained correlation between the spread of TOF distribution and the ions' translational temperature is discussed. For details on the COMSOL simulations, see Appendix A; and for details on the Molecular Dynamics simulations, see Appendix B.

5.1. Energy Distribution of Trapped Ions

A 3D model of the trap is imported into the COMSOL environment to obtain the potential landscape created by the static voltages of the various electrodes. Subsequently, in the Monte-Carlo simulation, this static potential is then combined with the potential created by the rf field to simulate the energy distribution, as shown in Figure 5. In case of OH^- thermalizing with helium buffer gas, the temperature obtained from the distribution is 373 K, and is a few Kelvin higher than that of the infinitely long wires (no endcaps). This stems from the fact that the static voltages push the ions into the rf field near the endcaps. While this relative effect is minimal at room temperatures, it is shown to become more pronounced and critical for cryogenic traps, where collisions occur in Kelvin regime [37]. While the dynamics of the ions in the low-to-mid energy range are well-represented by a Maxwell distribution, the high-energy tail of the distribution can be described with a Tsallis distribution [38].

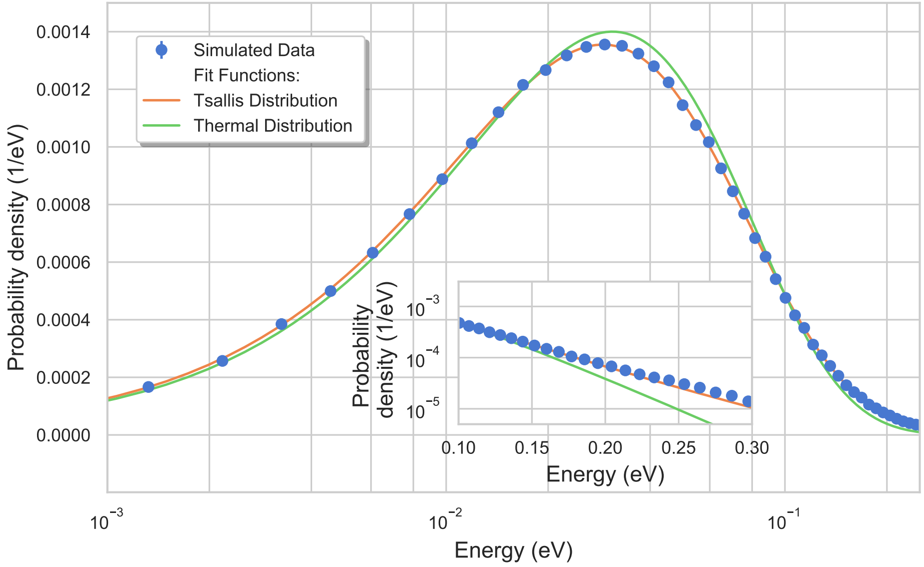

Figure 5. Simulated energy distribution of ions thermalized with a 293 K helium buffer gas in the HAI-trap potential landscape. The energy of the ions is characterized via a Tsallis with $T = 313(2)$ K and $q = 1.070(2)$ as well as a Maxwell distribution with $T = 359(3)$ K. It can be seen that the Maxwell fit overestimates the relative amount of low-energy to mid-energy and underestimates the high-energy tails which are then better represented via a Tsallis distribution (as shown in graph inset).

5.2. Spatial Distribution from Photodetachment Tomography

The difference between the two distributions, shown in Section 5.1, can be further characterized by mapping out the spatial ion distribution along the cylindrical axis of the ion trap via a far-threshold photodetachment tomography. This technique determines the density distribution without relying on a closed cycling transition and precise imaging systems. If the photon energy of the laser is above the electron affinity of the anion, then the process of laser-induced photodetachment, $OH^- + h\nu \rightarrow OH + e^-$, causes neutralization of the anion—as a result, it is lost from the trap.

For a narrow laser beam, this photodetachment loss rate is proportional to the photon flux and the ions' single particle column density at the position of the laser beam. The single particle column density n_{col} can then be extracted by measuring the exponential decay rate κ (extracted from the ions' loss behavior following $N(t) = N_0 \exp\left[-\kappa t\right]$) and the background loss rate Γ in the trap as

$$n_{\mathrm{col}}(x_L, y_L) = \frac{\kappa(x_L, y_L) + \Gamma}{\sigma_{pd} P_L / h\nu}, \tag{4}$$

where σ_{pd} is the absolute photodetachment cross section and P_L the laser power. For OH^-, a free-running laser diode at a wavelength of 660 nm, far above the detachment threshold of 678 nm, was used. The laser light is focused to a beam diameter of 180 µm and can be moved parallel to the trap's axis. A measurement along the trap axis is shown in Figure 6. The axial confinement created by the endcaps and the axial shielding plates can be well described by a harmonic potential. That implies a direct proportionality between the variance in position along that axis and the translational temperature of the ions.

Note that for more accurate modeling of our trap, surface charges were introduced on both PCBs to account for the shift in mean position and width of the ion cloud. More details on this procedure can be found in Section 5.3. In Figure 6, the spatial distribution of the ions' corresponding to the energy distribution described previously (in Figure 5) is shown. The simulated ion distribution n_{ion} is related to the potential as

$$n_{\text{ion}} \sim \exp(-\frac{V_{\text{tot}}}{k_{\text{B}}T}) \tag{5}$$

for a Maxwell distribution and as

$$n_{\text{ion}} \sim \left(1 - (1-q)\left(\frac{V_{\text{tot}}}{k_{\text{B}}T}\right)^{\frac{1}{1-q}}\right) \tag{6}$$

for a Tsallis distribution [38,39], where q is the shaping parameter and V_{tot} is the sum of the static potentials as well as the effective potential calculated via Equation (1). A significant difference between the Tsallis and the Maxwell distribution can be seen near the peak of the distribution, with the Tsallis model exhibiting a narrower ion distribution. Although higher energy tails are predicted by the Tsallis distribution, the wings show little to no deviations.

In conclusion, it can be said that in the case of collisions of ions with a buffer gas at room temperature, the deviations from the Maxwell distribution in an octupole trap can be neglected. However, changes in the ions' phase space density arising due to sympathetic cooling methods with different neutral-ion mass ratio might result in distributions with a higher q-parameter [40–42]. In this case, it becomes imperative to include a detailed characterization of the Tsallis energy distribution.

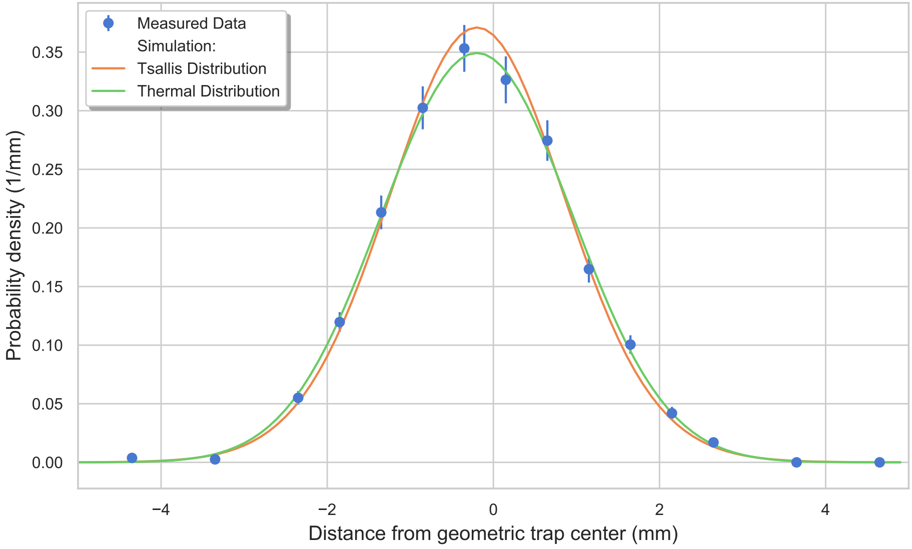

Figure 6. Column density profile as a function of the axial laser position along the cylindrical axis of the trap. Each point was derived by fitting a first-order exponential decay to the ion signal for multiple interaction times with a far-threshold laser beam. The standard deviation of the fits are presented by the error bars. The measured density distribution is compared with the simulated potential which accounts for surface charges. Equations (5) and (6) are used to derive a density distribution from this potential using the simulated energy distribution from Figure 5. The probability density curves shown here are normalized to 1.

5.3. Effect of Surface Charges on the Ion Distribution

Tomography of an ion ensemble also serves as a tool to account for the charging up of PCBs used in the setup. The exposed PCBs can accumulate charges, thus prompting the modification of the potentials used in the model. Hence, we add surface charges to both PCBs until the mean position and the width of ions' distribution matches the one obtained via a photodetachment tomography.

To motivate the modeling of trap discrepancies via surface charges, an example is demonstrated in Figure 7. The charge build-up on the PCBs in this instance is more severe than the one seen in Figure 6 (where a symmetric charge distribution on the PCBs is observed). In order to characterize the charges, two tomography measurements were performed at different static voltages applied to the endcap electrodes. Change in the static voltage results in the change of both mean position and width of the ion cloud. The charges are calculated such that they match the ion distribution observed at an endcap voltage of 80 V and at a temperature of 373 K. Once the distributions match, the charges are fixed and, using the same charge distribution, the modified potential successfully reproduces the ion density distribution measured for an endcap voltage of 40 V.

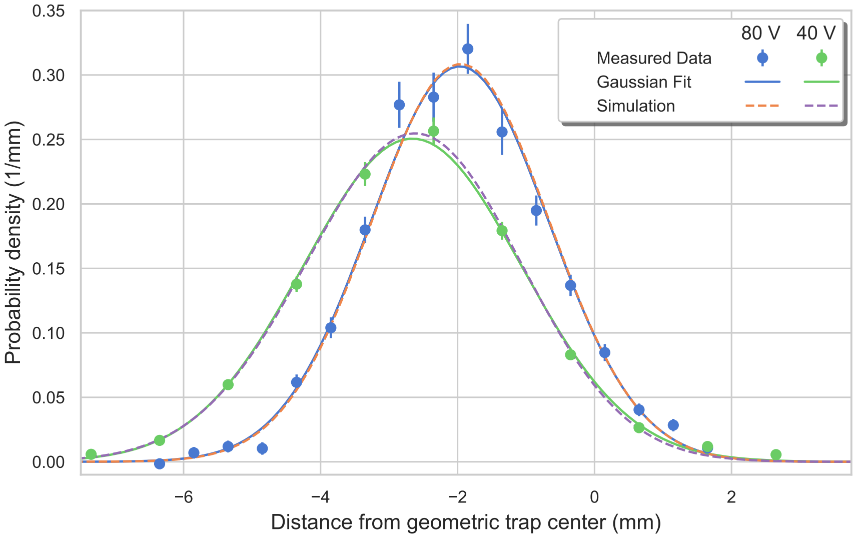

Figure 7. Characterization of surface charge accumulation on PCBs. The surface charge distribution is defined such that the tomography measurements for 80 V endcap voltage matches the simulated ion distribution at a temperature of 373 K. Once the charges are fixed, the modified potential is used to obtain the ion distribution for a configuration with 40 V endcap voltage, which matches the measured ion density distribution for the chosen endcap voltage.

5.4. Correlation between Ions' TOF Distribution and Their Translational Temperature

To model the extraction of the ions from the trap onto the detector, the ions are initially placed in the extraction potential of the trap at randomized initial positions and velocities. The velocity vectors are randomly sampled from a Maxwell–Boltzmann distribution at a given temperature. The ion's position, though randomly sampled, is weighted with the simulated trapping potential, and expected ion distribution is calculated as $\rho_{\text{ion}} \sim \exp(-\frac{V_{\text{tot}}}{k_B T})$. It is imperative to account for the simulated potential so as to accurately describe the appearance of pockets, i.e., regions of global maxima in the ion density distribution. Figure 8a shows a cut of the radial ion distribution at the axial local potential minimum (trap center) at 373 K, while Figure 8b shows the same at 30 K. At higher temperatures, the ion distribution is very homogeneous, but the effect of local potential minima becomes particularly pronounced at lower temperatures. The origin of these pockets lies in the symmetry-breaking of the potential, as reported in [32]. Here, the axial and vertical shielding electrodes have a strong influence in the trap center, thus leading to symmetry-breaking in the trap. This results in the two pockets, as the potential landscape is strongly dominated by the two pairs of shielding electrodes. The depth of the pockets is calculated from the energy of ions E via the relation $T = \frac{2E}{k_B}$ to $\sim$60 K. As previously mentioned, the initial positions and velocities of the ions are randomly sampled, prior to the extraction from the trap. The arrival time of the ions is then binned and subsequently represented by a Gaussian fit.

The expectation for the relationship between the variance of the ions' TOF distribution and their temperature is a linear function. This assumption is based on the following considerations: Firstly, the TOF spread is primarily dominated by the velocity vectors along the main axis, pointing towards or opposite to the detector. The TOF spectrometer was adjusted to create a symmetric ion distribution via the axial shielding plates, as described in Section 3. The axial velocity spread is described by a Gaussian distribution with $\sigma_v^2 \propto k_\mathrm{B}T$. Secondly, the axial spatial distribution is governed by the harmonic potential defined via a Gaussian distribution, where $\sigma_s^2 \propto k_\mathrm{B}T$ holds valid again. Lastly, the extraction potential is well-approximated via sequential regions of linear acceleration. Thus, the axial velocity distribution of the ions can be linearly mapped onto the ions' time of flight to the detector. In agreement with this expected behavior, a linear relationship between the variance, i.e., σ^2, of ions' TOF distribution and their translational temperature is seen in Figure 9.

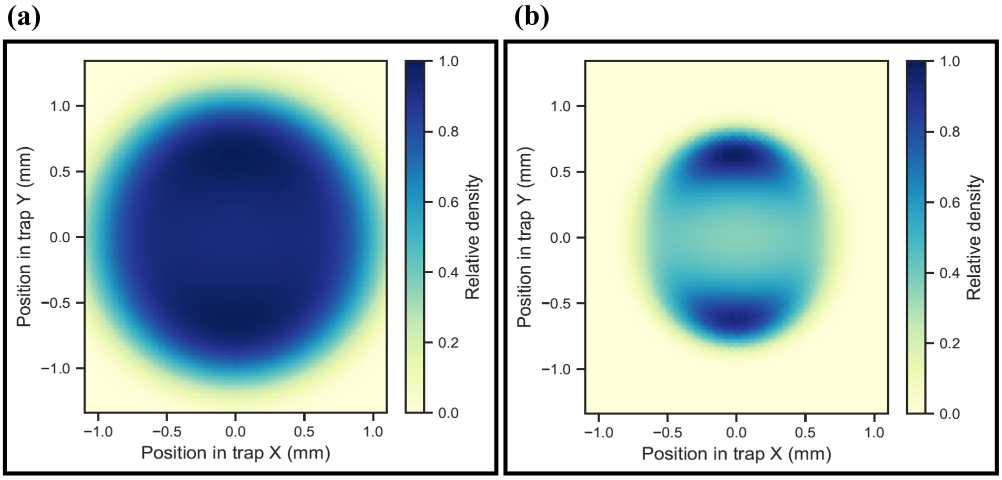

Figure 8. Heatmap representation for the density distribution of ions in the trap. (**a**) Homogenoues ion density distribution at 373 K. (**b**) Ion density distribution at 30 K exhibiting regions of global maxima called "pockets". The depth of the pockets is calculated from the energy of ions E via the relation $T = \frac{2E}{k_\mathrm{B}}$ to ~60 K. The axes used are corresponding to the coordinates shown in Figure 2.

It is important to note that for temperatures lower than 60 K, a deviation from the initial linear slope is seen. This can be attributed to the aforementioned occurrence of pockets in this temperature regime. The ions get trapped locally in these pockets which exhibit a more quadrupole-like character. During the extraction, this causes the radial velocity component of the ions pointing radially outwards to rapidly turn around, thus decreasing the time spent in the trap and hence, the TOF spread.

Using the time-of-flight (TOF) trace corresponding to the tomography from Figure 6, and the linear fit for temperatures above 60 K in Figure 9, one can calculate the temperature of the "benchmark measurement" as 370(12) K. This is in line with the predicted value by the Monte-Carlo simulations. Since the tomography measurements are time-consuming, the calibration between the TOF variance and temperature of the ion ensemble provides a fast and reliable thermometry method to determine external or translational temperature of the ions trapped in a rf trap.

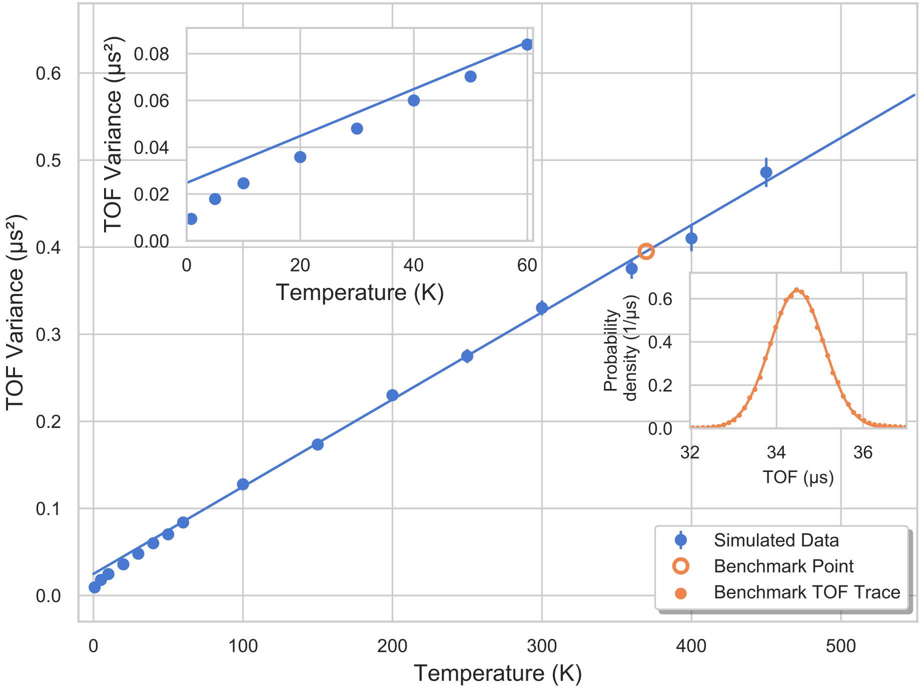

Figure 9. The variance of the TOF distribution, i.e., σ^2, plotted as a function of the initial temperature of the ions in the trap before extraction onto the detector. The change in the linear slope can be seen in the left inset. It is interpreted as a consequence of the pockets arising at a temperature regime of about 60 K. Furthermore, the temperature from the corresponding TOF trace of the tomography measurements is derived to be 370 K, which is consistent with the Monte-Carlo simulations' prediction. This TOF trace is shown in the right inset along with the Gaussian fit representing the distribution.

6. Conclusions

In this work, we presented a thermometry technique that uses the linear relationship between the motional temperature of an ensemble of ions trapped in a multipole trap and the variance of the time-of-flight distribution of the extracted ions. This technique provides a fast and reliable method to determine the energy distribution of, in principle, any ionic species confined in an ion trap, and can be used to measure the external temperature ranging from hundreds of Kelvin down to a few Kelvin. In our study, a deviation of the linear behavior was observed for lower temperatures. This is attributed to the existence of multiple potential minima in the trapping potential. These minima become more prominent at lower temperatures and were included in our model to obtain an accurate temperature calibration curve in the Kelvin range for our thermometry method. Additionally, the simulation of the trapping potential was modified to account for surface charge accumulation, thus increasing the accuracy of our model and allowing us to simulate the spatial distribution of the ion ensemble in the trap. This altered potential was determined by using an axial tomography measurement from our trap as well as a Monte-Carlo simulation, which predicted the energy distribution of ions colliding with room-temperature helium buffer gas. We showed that our octupole radio-frequency wire trap can create, with sufficiently higher voltage, nearly the same effective potential as the corresponding ideal hyperbolic or cylindrical rod trap. Further, a Monte-Carlo simulation shows that, after interaction with a room temperature helium buffer gas, the ions thermalize to the same final energy distribution in all the three trap types. A temperature higher than that of the buffer gas is obtained for all simulated traps attributed to the rf micromotion heating. These findings support that a wire trap with its superior optical access, in comparison to a trap utilizing thicker rods, is an ideal instrument for a hybrid trap and comes at little to no disadvantages. The optical access facilitates the laser cooling of rubidium atoms present in the chamber in order to create a dense atomic cloud and overlap it with the trapped ensemble of hydroxyl anions. With the flexibility to trap and characterize any ionic species in the setup, this system provides an excellent platform to study diverse atom–ion interactions.

Author Contributions: Conceptualization, E.E., R.W., and M.W.; formal analysis, M.N.; software, M.N.; investigation, M.N., S.Z.H., and J.T.; writing—original draft preparation, S.Z.H.; writing—review and editing, M.N., S.Z.H., R.W., and M.W.; supervision, R.W. and M.W.; funding acquisition, R.W. and M.W. All authors have read and agreed to the published version of the manuscript.

Funding: This work has been supported by the Austrian Science Fund (FWF) through Project No. I3159-N36 and Deutsche Forschungsgemeinschaft (DFG) under Project No. WE/2661/14-1. S.Z.H. acknowledges the support from IMPRS-QD fellowship and HGSFP.

Acknowledgments: The authors would like to acknowledge Bastian Höltkemeier, Henry López-Carrera and Tobias Heldt for their role in implementing the experimental setup and fruitful discussions.

Conflicts of Interest: The authors declare no conflict of interest. The funders had no role in the design of the study; in the collection, analyses, or interpretation of data; in the writing of the manuscript, or in the decision to publish the results.

Appendix A. COMSOL Multiphysics® Simulations

The simulations described in this work were performed in the COMSOL Multiphysics 5.4 software [43]. It utilizes the finite element method for calculation of the static potentials as well as the harmonically changing radio frequency field. The *AC/DC* module with its *Electrostatics* and *Electric Currents* submodules were used in all the simulations. The 2-dimensional geometries of the different trap types were created within COMSOL.

The ideal multipole potential is created by rods with hyperbolic shapes, however, in practice, cylindrical rods are often used instead. For the hyperbolic trap, the octupole field was modeled as [44]

$$\psi(x,y) = \left(\frac{\psi_0}{2r_0^4}\right)(x^4 - 6x^2y^2 + y^4). \tag{A1}$$

For the 3D simulation of the trapping potential, a 3D model of our setup including ion optics and metal and plastic holders was loaded into the software. For the different materials used in the trap assembly (Steel, PEEK, etc.), the corresponding relative permittivity constants were accounted for. Note that for both the 2D as well as the 3D simulations, COMSOL's infinite element domain feature was employed. This was used to model a grounded vacuum chamber infinitely far away, which allowed for an overall smaller geometry to be simulated.

For extraction of ions from the trap, the *Charged Particle Tracing* module was used. The extraction from the trap is done without including Coulomb interaction between the particles. For each temperature, an ensemble consisting of 150,000 ions was initialized into the trap and the particles were extracted simultaneously.

Appendix B. Molecular Dynamics Simulation

The molecular dynamics simulation employed in this work calculates the ion trajectory of a single ion in a multipole trap by solving Newton's equations of motion. The electric field vectors for the calculation of the force acting on the charged particle are obtained from a COMSOL simulation. The radio-frequency field is modulated with a sine-function and is superimposed with constant electric field vectors forming the static voltages. The ion is propagated using the well-known Verlet algorithm since it is time efficient to compute and is symplectic—i.e., it conserves phase space. Since a discrete amount of electric field vectors are loaded into the simulation, the exact force acting on a particle is determined by linear interpolation of the nearby vectors. The collisions with a buffer gas are modeled as random events. After each time step, it is calculated by drawing a number from a random distribution, representing whether a collision occurred or not. In the case where a collision is detected, the ion and the buffer gas are moved into the center-of-mass frame, with the buffer gas velocity vector components being drawn from 1D Maxwell–Boltzmann distributions. A hard sphere collision is calculated, and the velocity vector components of the ion are changed accordingly. The position and velocity of the ion is recorded after the time-average of 25 buffer gas collisions. In case the ion is lost from the trap, a new ion is added in the center of the trap and initialized by waiting for 500 collisions.

After half a million recordings (for the 2D simulations), or 1 million recordings (for the 3D simulations), the simulation is terminated and the data is evaluated by binning the velocities. The time between two collisions with the buffer gas is 10 µs, the time-step size of the simulation is 7 ns, and the resolution of the electric field grid is 1000 per mm. All the three parameters were checked for convergence, and sweeps of different time steps, electric field grid resolution, and buffer gas collision rate were performed in order to investigate a change in temperature for the result. Note that the time between two buffer gas collision was checked between 1 ms and 0.1 µs, but no significant change in temperature was detected for the trap frequencies f of 5 MHz and 6.8 MHz used in the simulation. The simulation step sizes were checked between 0.7 ns to 50 ns. Stable trapping and convergent energy distributions were achieved for 10 ns step size, thus a step size of 7 ns was chosen for time efficiency.

References

1. Schuessler, H.A.; Holder, C.H.; Chun-Sing, O. Orbiting charge-transfer cross sections between He^+ ions and cesium atoms at near-thermal ion-atom energies. *Phys. Rev. A* **1983**, *28*, 1817–1820. [CrossRef]
2. Côté, R. From Classical Mobility to Hopping Conductivity: Charge Hopping in an Ultracold Gas. *Phys. Rev. Lett.* **2000**, *85*, 5316–5319. [CrossRef] [PubMed]
3. Balakrishnan, N.; Dalgarno, A. Chemistry at Ultracold Temperatures. *Chem. Phys. Lett.* **2001**, *341*, 652–656. [CrossRef]
4. Rellergert, W.G.; Sullivan, S.T.; Kotochigova, S.; Petrov, A.; Chen, K.; Schowalter, S.J.; Hudson, E.R. Measurement of a Large Chemical Reaction Rate between Ultracold Closed-Shell ^{40}Ca Atoms and Open-Shell $^{174}Yb^+$ Ions Held in a Hybrid Atom-Ion Trap. *Phys. Rev. Lett.* **2011**, *107*, 243201. [CrossRef] [PubMed]
5. Willitsch, S. Coulomb-crystallised molecular ions in traps: Methods, applications, prospects. *Int. Rev. Phys. Chem.* **2012**, *31*, 175–199. [CrossRef]
6. Ravi, K.; Lee, S.; Sharma, A.; Werth, G.; Rangwala, S.A. Cooling and stabilization by collisions in a mixed ion-atom system. *Nat. Commun.* **2012**, *3*, 1126. [CrossRef]
7. Ratschbacher, L.; Zipkes, C.; Sias, C.; Köhl, M. Controlling chemical reactions of a single particle. *Nat. Phys.* **2012**, *8*, 649–652. [CrossRef]
8. Puri, P.; Mills, M.; Simbotin, I.; Montgomery, J.A.; Côté, R.; Schneider, C.; Suits, A.G.; Hudson, E.R. Reaction blockading in a reaction between an excited atom and a charged molecule at low collision energy. *Nat. Chem.* **2019**, *11*, 615–621. [CrossRef]
9. Dalgarno, A.; Rudge, M.R.H. Cooling of Interstellar Gas. *Astrophys. J.* **1964**, *140*, 800. [CrossRef]
10. Stancil, P.C.; Lepp, S.; Dalgarno, A. The lithium chemistry of the early Universe. *Astrophys. J.* **1996**, *458*, 401. [CrossRef]
11. Steigman, G. Charge transfer reactions in multiply charged ion-atom collisions. *Astrophys. J.* **1975**, *199*, 642–646. [CrossRef]
12. Vuitton, V.; Yelle, R.; McEwan, M. Ion chemistry and N-containing molecules in Titan's upper atmosphere. *Icarus* **2007**, *191*, 722–742. [CrossRef]
13. Snow, T.P.; Bierbaum, V.M. Ion Chemistry in the Interstellar Medium. *Ann. Rev. Anal. Chem.* **2008**, *1*, 229–259. [CrossRef] [PubMed]
14. Vuitton, V.; Lavvas, P.; Yelle, R.; Galand, M.; Wellbrock, A.; Lewis, G.; Coates, A.; Wahlund, J.E. Negative ion chemistry in Titan's upper atmosphere. *Planet. Space Sci.* **2009**, *57*, 1558–1572. [CrossRef]
15. Reddy, V.S.; Ghanta, S.; Mahapatra, S. First Principles Quantum Dynamical Investigation Provides Evidence for the Role of Polycyclic Aromatic Hydrocarbon Radical Cations in Interstellar Physics. *Phys. Rev. Lett.* **2010**, *104*, 111102. [CrossRef]
16. Bohringer, H.; Glebe, W.; Arnold, F. Temperature dependence of the mobility and association rate coefficient of He^+ions in He from 30–350K. *J. Phys. B At. Mol. Phys.* **1983**, *16*, 2619–2626. [CrossRef]

17. Eppink, A.T.J.B.; Parker, D.H. Velocity map imaging of ions and electrons using electrostatic lenses: Application in photoelectron and photofragment ion imaging of molecular oxygen. *Rev. Sci. Instrum.* **1997**, *68*, 3477–3484. [CrossRef]
18. Neuhauser, W.; Hohenstatt, M.; Toschek, P.E.; Dehmelt, H. Localized visible Ba^+ mono-ion oscillator. *Phys. Rev. A* **1980**, *22*, 1137–1140. [CrossRef]
19. Bergquist, J.C.; Wineland, D.J.; Itano, W.M.; Hemmati, H.; Daniel, H.U.; Leuchs, G. Energy and Radiative Lifetime of the $5d^9 6s^{22} D_{\frac{5}{2}}$ State in Hg II by Doppler-Free Two-Photon Laser Spectroscopy. *Phys. Rev. Lett.* **1985**, *55*, 1567–1570. [CrossRef]
20. Segall, J.; Lavi, R.; Wen, Y.; Wittig, C. Acetylene carbon-hydrogen bond dissociation energy using 193.3-nm photolysis and sub-Doppler resolution hydrogen-atom spectroscopy: 127 .+-. 1.5 kcal mol^{-1}. *J. Phys. Chem.* **1989**, *93*, 7287–7289. [CrossRef]
21. Kinugawa, T.; Arikawa, T. Three-dimensional velocity analysis combining ion imaging with Doppler spectroscopy: Application to photodissociation of HBr at 243 nm. *J. Chem. Phys.* **1992**, *96*, 4801–4804. [CrossRef]
22. Schlemmer, S.; Kuhn, T.; Lescop, E.; Gerlich, D. Laser excited N2+ in a 22-pole ion trap:: Experimental studies of rotational relaxation processes. *Int. J. Mass Spectrom.* **1999**, *185–187*, 589–602. [CrossRef]
23. Glosík, J.; Hlavenka, P.; Plašil, R.; Windisch, F.; Gerlich, D.; Wolf, A.; Kreckel, H. Action spectroscopy of and D_2H^+ using overtone excitation. *Philos. Trans. R. Soc. A Math. Phys. Eng. Sci.* **2006**, *364*, 2931–2942. [CrossRef] [PubMed]
24. Otto, R.; von Zastrow, A.; Best, T.; Wester, R. Internal state thermometry of cold trapped molecular anions. *Phys. Chem. Chem. Phys.* **2013**, *15*, 612–618. [CrossRef] [PubMed]
25. Lakhmanskaya, O.; Simpson, M.; Wester, R. Vibrational overtone spectroscopy of cold trapped hydroxyl anions. *Phys. Rev. A* **2020**, in press. [CrossRef]
26. Deiglmayr, J.; Göritz, A.; Best, T.; Weidemüller, M.; Wester, R. Reactive collisions of trapped anions with ultracold atoms. *Phys. Rev. A* **2012**, *86*, 043438. [CrossRef]
27. Trippel, S.; Mikosch, J.; Berhane, R.; Otto, R.; Weidemüller, M.; Wester, R. Photodetachment of cold OH^- in a multipole ion trap. *Phys. Rev. Lett.* **2006**, *97*, 193003. [CrossRef]
28. Hlavenka, P.; Otto, R.; Trippel, S.; Mikosch, J.; Weidemüller, M.; Wester, R. Absolute photodetachment cross section measurements of the O^- and OH^- anion. *J. Chem. Phys.* **2009**, *130*, 061105. [CrossRef]
29. Osborn, D.L.; Leahy, D.J.; Cyr, D.R.; Neumark, D.M. Photodissociation spectroscopy and dynamics of the $N_2O_2^-$ anion. *J. Chem. Phys.* **1996**, *104*, 5026–5039. [CrossRef]
30. Höltkemeier, B.; Glässel, J.; López-Carrera, H.; Weidemüller, M. A dense gas of laser-cooled atoms for hybrid atom-ion trapping. *Appl. Phys. B Lasers Opt.* **2017**, *123*, 51. [CrossRef]
31. Nadarajah, S. A generalized normal distribution. *J. Appl. Stat.* **2005**, *32*, 685–694. [CrossRef]
32. Otto, R.; Hlavenka, P.; Trippel, S.; Mikosch, J.; Singer, K.; Weidemüller, M.; Wester, R. How can a 22-pole ion trap exhibit ten local minima in the effective potential? *J. Phys. B At. Mol. Opt. Phys.* **2009**, *42*, 154007. [CrossRef]
33. Okada, K.; Yasuda, K.; Takayanagi, T.; Wada, M.; Schuessler, H.A.; Ohtani, S. Crystallization of Ca^+ ions in a linear rf octupole ion trap. *Phys. Rev. A* **2007**, *75*, 033409. [CrossRef]
34. Wester, R. Radiofrequency multipole traps: Tools for spectroscopy and dynamics of cold molecular ions. *J. Phys. B At. Mol. Opt. Phys.* **2009**, *42*, 154001. [CrossRef]
35. Gerlich, D., Inhomogeneous RF Fields: A Versatile Tool for the Study of Processes with Slow Ions. In *Advances in Chemical Physics*; John Wiley & Sons, Ltd.: Hoboken, NJ, USA, 2007; pp. 1–176. [CrossRef]
36. Ter Haar, D. (Ed.) The Maxwell—Boltzmann Distribution. In *Elements of Statistical Mechanics*, 3rd ed.; Butterworth-Heinemann: Oxford, UK, 1995; Chapter 2, pp. 36–58. [CrossRef]
37. Asvany, O.; Schlemmer, S. Numerical simulations of kinetic ion temperature in a cryogenic linear multipole trap. *Int. J. Mass Spectrom.* **2009**, *279*, 147–155. [CrossRef]
38. Tsallis, C. Possible generalization of Boltzmann-Gibbs statistics. *J. Stat. Phys.* **1988**, *52*, 479–487. [CrossRef]
39. Tsallis, C.; Mendes, R.; Plastino, A. The role of constraints within generalized nonextensive statistics. *Phys. A Stat. Mech. Appl.* **1998**, *261*, 534–554. [CrossRef]
40. Höltkemeier, B.; Weckesser, P.; López-Carrera, H.; Weidemüller, M. Dynamics of a single trapped ion immersed in a buffer gas. *Phys. Rev. A* **2016**, *94*, 062703. [CrossRef]

41. Höltkemeier, B.; Weckesser, P.; López-Carrera, H.; Weidemüller, M. Buffer-Gas Cooling of a Single Ion in a Multipole Radio Frequency Trap Beyond the Critical Mass Ratio. *Phys. Rev. Lett.* **2016**, *116*, 233003. [CrossRef]
42. Rouse, I.; Willitsch, S. Superstatistical Energy Distributions of an Ion in an Ultracold Buffer Gas. *Phys. Rev. Lett.* **2017**, *118*, 143401. [CrossRef]
43. COMSOL Multiphysics, Version 5.4. Available online: https://www.comsol.com/ (accessed on 16 June 2020).
44. Friedman, M.H.; Yergey, A.L.; Campana, J.E. Fundamentals of ion motion in electric radio-frequency multipole fields. *J. Phys. E Sci. Instrum.* **1982**, *15*, 53–56. [CrossRef]

© 2020 by the authors. Licensee MDPI, Basel, Switzerland. This article is an open access article distributed under the terms and conditions of the Creative Commons Attribution (CC BY) license (http://creativecommons.org/licenses/by/4.0/).

In the following sections, additional insights about the thermometry method presented in the published work are discussed. Firstly, a discussion on the linear mapping between the temperature of the trapped ions and the variance of their TOF to the detector for a one-dimensional (1D) case is presented along with the limitations of this method, followed by an example application where the ion ensemble's temperature is measured as it undergoes far-threshold laser-induced forced evaporative cooling.

3.3 Mapping ion temperature to their TOF

In order to understand the origin of the linear mapping found between the trapped ions' temperature (or kinetic energy) and their TOF to the detector, we investigate an ensemble of ions flying towards a detector, in a 1D scenario.

Assume an ion with charge q and mass m, initially at rest at $t = 0$. When subjected to an electric field E, it is accelerated by an amount $a = \frac{qE}{m}$, over a certain distance z. The time it takes to traverse through this field is calculated as [176, 202]:

$$t_{\text{field}} = \sqrt{\frac{2mz}{qE}} \tag{3.1}$$

After passing through this single acceleration stage, the ion enters a field-free drift region, flying towards a detector placed at a distance D. The time spent in this region is calculated as:

$$t_{\text{drift}} = D \cdot \sqrt{\frac{m}{2qEz}} \tag{3.2}$$

Thus, the total time ions take to arrive at the detector, t_{total} is described as:

$$\begin{align} t_{\text{total}} &= t_{\text{field}} + t_{\text{drift}} \tag{3.3}\\ &= \sqrt{\frac{2mz}{qE}} + D \cdot \sqrt{\frac{m}{2qEz}} \tag{3.4}\\ &= \frac{\sqrt{2mU}}{qE} + D \cdot \sqrt{\frac{m}{2U}} \tag{3.5} \end{align}$$

where $U = qEz$ is the kinetic energy gained by the ion during the acceleration stage. If the ion had an initial velocity v_0 with the corresponding kinetic energy U_0, then U transforms as $U = qEz + U_0$.

This principle can be extended to any subsequent acceleration or extraction potential of any arbitrary shape by approximating it as a finite sum of short linear acceleration stages where the time of flight for ions subjected to a total of k fields is described as:

$$t_{\text{total}} = \frac{v_1 - v_0}{a_1} + \sum_{i=2}^{k} \left(\frac{v_i - v_{i-1}}{a_i} \right) + \frac{D}{v_k} \tag{3.6}$$

where the last term represents flight time in the field-free region and v_k is defined as:

$$v_k = \left(v_0^2 + \sum_{i=1}^{k} 2a_i d_i\right)^{\frac{1}{2}} \tag{3.7}$$

Here, v_i are the velocities after the i-th field is applied after which the ions are accelerated by a_i, and v_0 is the initial velocity of the ion. The length of each acceleration stage is given as d_i and D is the last field-free flight region.

Assuming a thermal ensemble, some ions have a starting direction opposite to that of the detector. These ions will first be slowed down by the applied fields, and once they have zero velocity, they are turned around and are then accelerated towards the detector. This "turn-around" time t_{turn}, due to the initial kinetic energy of the ions, causes an additional lag in these ions' arrival time and is defined as:

$$t_{\text{turn}} = \mp \frac{m|v_0|}{qE} \cdot \hat{e}_z \tag{3.8}$$

where $\hat{e}_z$ is unit vector directed towards the detector and the ions' initial energy towards the detector gives them a head start. Thus, the observed time-of-flight of the ions (TOF) is now given as $t_{\text{obs}} = t_{\text{total}} + t_{\text{turn}}$. This effect also causes a broadening of the ions' TOF distribution.

Now that we have estimated the ions' time of flight to the detector in terms of its kinetic energy (or the initial velocity along the axis towards the detector), we can determine the ions' TOF distribution on the detector, if the ions' starting velocity distribution $P(v_0)$ is known. Here the function $P(\Delta t)$ gives the ion's time of flight distribution, as measured by the detector. With $v_0 = \frac{qE\Delta t}{m} = f(\Delta t)$, the distribution functions are related as [203]:

$$P(\Delta t) = P(f(\Delta t)) \cdot f'(\Delta t) = P(v_0) \cdot \frac{qE}{m} \tag{3.9}$$

If we start with an ion ensemble with a velocity distribution described via a Maxwell-Boltzmann distribution, we have:

$$P(v_0) = N_v \cdot \exp^{-\frac{mv_0^2}{k_\mathrm{B} T_\mathrm{I}}} \tag{3.10}$$

where N_v is the normalization constant, k_B is the Boltzmann constant and T_I is the temperature of the ion ensemble. This would correspond to a TOF distribution, $P(\Delta t)$ as:

$$P(\Delta t) = N_t \cdot \exp^{-\frac{q^2 E^2 \Delta t^2}{m k_\mathrm{B} T_\mathrm{I}}} \tag{3.11}$$

where N_t is the normalization constant. Thus, we see that the Gaussian shape of the thermal ion ensemble is conserved in the time domain, where the variance of the TOF distribution is directly proportional to the ion temperature (via $k_\mathrm{B} T_\mathrm{I}$).

This mapping between the ions' energy distribution and the TOF distribution also applies for non-thermal ion distributions, for instance Tsallis ion distributions often encountered in rf traps.

Until now, all the ions are assigned the same starting position and the spread in the initial position of the ions is neglected. In order to account for this spread, the spatial density distribution of the trapped ions must be determined. The axial confinement of the ions, in a multipole ion trap, is created via static voltages, which results in a harmonic potential in the axial direction. The spatial distribution of the ion cloud in this direction is thus described by a Gaussian distribution. In the case of an initial section with non-linear accelerations over the region of ions' spatial extent, an asymmetrical broadening of the ions' TOF distribution will arise. The simulations show that these effects are found to be negligible in the case of our octupole trap for ion temperatures between 1 K and 400 K. However, for higher temperatures due to a larger spatial extent of the ions, the ion distribution will increasingly experience the effects of such non-linearities (as they are spread farther away from the center of the trap and also closer to the endcap electrodes). In such a scenario, a more extensive acquisition and analysis of the TOF spread would be needed.

An additional effect that is more prominent in our system, is the radial spatial and velocity distribution of the ion cloud. During their extraction onto the detector, the ions are spatially focused through a narrow endcap which also causes the redistribution of the radial and axial components of their velocities. This gives rise to the offset between TOF variance and temperature, as seen in Figure 9 of the published paper in Section 3.2. To observe the dependence of the offset on the trap order, a simple three-dimensional model for a multipole trap with varying pole order n, is simulated and is shown in Figure 3.1. The radial trapping parameters are adjusted to have the same effective radial potential for all cases. It can be seen that for higher multipole orders, a higher offset in the linear mapping is observed. As shown, for temperatures lower than 100 K, the regions of local potential minima become significant and the mapping between the ions' TOF variance and ion temperature deviates from the initial linear trend and exhibits a larger slope.

With these considerations into account, we established a thermometry method to determine the temperature of ions in our system comprising of an octupole rf trap. In the following section, the results of the laser-induced forced evaporative cooling of an anion cloud are presented, where the ion temperature determination via TOF thermometry, supplemented with a thermodynamical description, played a critical role in explaining the dynamics of anion-photon interactions.

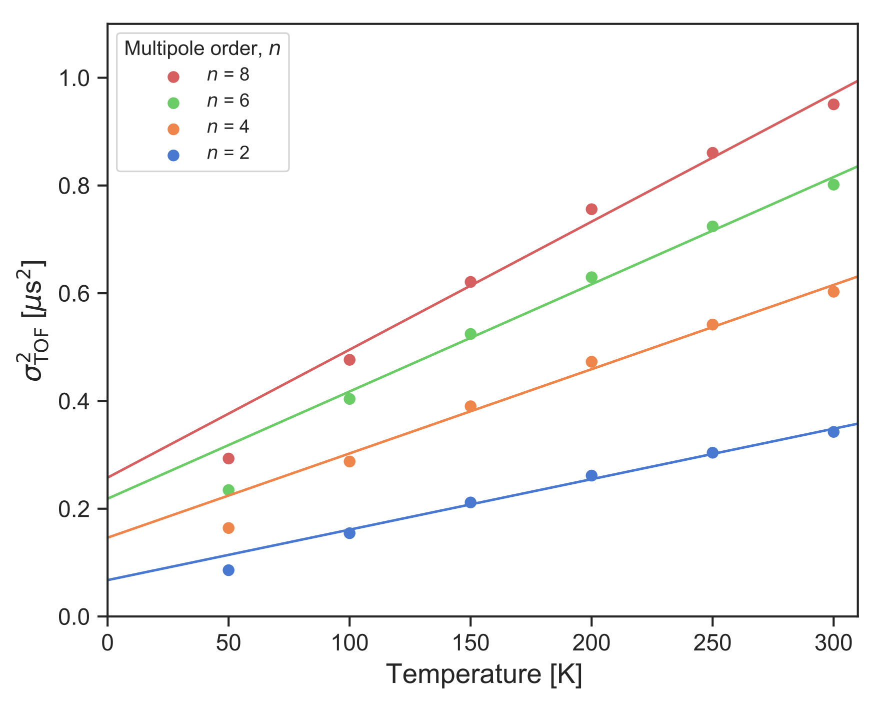

Figure 3.1: The mapping between the variance of the ions' TOF distribution and the temperature of the trapped ions, is shown for a simple model of a multipole trap with different pole order n. The offset arising due to the redistribution of the radial and axial velocity components during extraction increases with increasing pole order. For temperatures lower than 100 K, a deviation from the initial trend is seen as the effect of local potential minima becomes significant at lower temperatures.

3.4 Temperature determination in anion cooling

The theoretical model for laser-induced cooling of trapped anions was already proposed decades ago in the work of A. Crubellier [92]. Building on these ideas, the experimental results achieved for the laser-induced forced evaporative cooling of OH^- anions via a far-threshold photodetachment laser beam are presented in this section, with a focus on the temperature determination of the ions using the previously described TOF thermometry method. The details on the measurement techniques and the thermodynamical model are extensively discussed in [168].

A cloud of OH^- anions is trapped in the octupole ion trap, and after thermalization with a room-temperature helium buffer gas the initial temperature of the ions is determined to be 390(15) K. A far-threshold photodetachment (PD) beam with wavelength $\lambda_{\mathrm{PD}} = 660$ nm, power $P_{\mathrm{PD}} = 41$ mW and beam diameter $\omega_{\mathrm{PD}} \approx 180\ \mu$m is placed at the radial center of the ion cloud and moved axially from an initial position of 4 mm away from the axial center of the ion cloud towards the center of the ion distribution with a speed $v_{\mathrm{PD}} = 0.5\,\mathrm{mm\,s^{-1}}$. The change in the ions' TOF distributions due to the varying interaction times with the laser beam is shown in Figure 3.2.

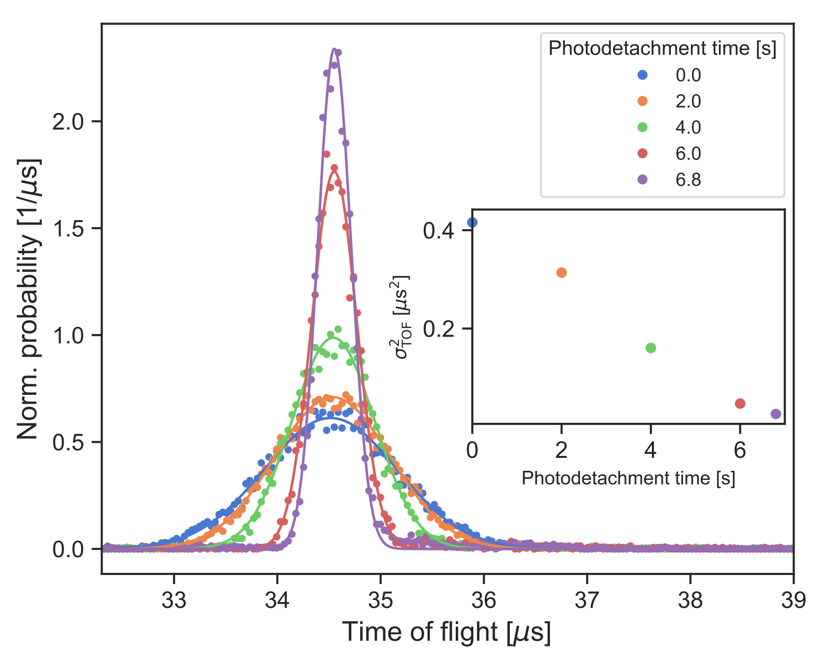

Figure 3.2: Evolution of the ions' TOF distribution for varying interaction time with the photodetachment laser beam. The points are the experimentally measured distributions, fitted with Gaussian distributions, represented by the solid lines. In the inset, the variance of the obtained Gaussian distribution's width, σ^2_{TOF}, is shown as a function of the photodetachment time. The shrinking of the ions' TOF variance is a signature of the forced evaporative cooling of the ions via a far-threshold laser beam.

Since the initial position of the beam is always the same, the effective interaction time of the ion ensemble with the photodetachment laser beam is determined by the final beam position which is the observable being tuned during the measurements. As a result, the hottest ions at the edge of the ion cloud are dynamically photodetached from the trap, such that the remaining ions closer to the center then rethermalize to a colder temperature. As discussed in Section 3.2, the established mapping between the temperature of ions in the trap and their TOF to the detector is used to determine the ions' temperature from the variance of their TOF distribution (square of the width σ_{TOF}, obtained via a Gaussian fit).

This measurement is then performed for different speeds of the photodetachment laser beam. The change in ions' temperature as a function of photode-

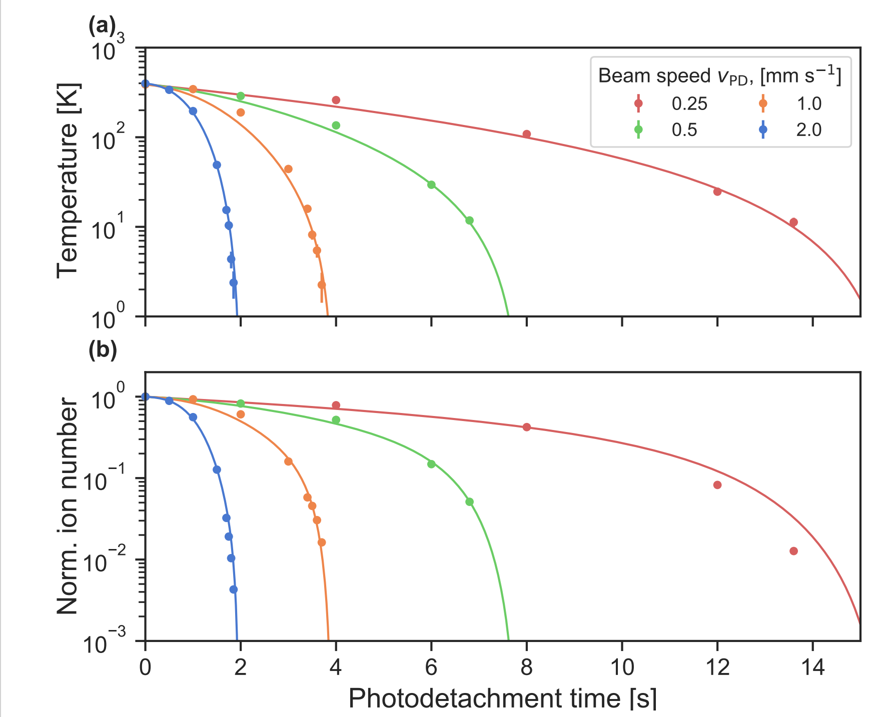

Figure 3.3: Laser-induced forced evaporative cooling of molecular OH$^-$ anions. (a) The change in the ion temperature as a function of interaction time with the photodetachment laser beam is shown for varying speeds of the laser beam. The effective interaction time is determined by the initial beam position (same for all cases), the final beam position, and the displacement speed of the photodetachment beam. (b) The corresponding change in the normalized ion number is shown. The points are the experimentally measured data and the solid lines are the numerical solution of the differential equation given in Equation 3.12 and 3.13. Adapted from [168].

tachment time is shown in Figure 3.3 (a). The corresponding change in the ion numbers is shown in Figure 3.3 (b).

The description of the time evolution in the ion temperature T_I and number N_I, due to the dynamic photodetachment of ions is adapted from Crubellier's model [92] to account for a time-dependent laser beam position and is described as [168]:

$$\begin{aligned}\dot{T}_\mathrm{I} = &-\left(\frac{3}{7}\right)\frac{\sigma_\mathrm{PD}}{k_\mathrm{B}}\int_{-\infty}^{\infty}\rho_\mathrm{I}(x,y,z,T_\mathrm{I})\phi_\mathrm{L}\big(y,z,0,(4\,\mathrm{mm}-v_\mathrm{PD}t)\big)V_{\mathrm{OH}^-}(x,y,z)\,dxdydz\\ &+\left(\frac{3}{7}\right)\left(\frac{5}{6}\right)\sigma_\mathrm{PD}T_\mathrm{I}\int_{-\infty}^{\infty}\rho_\mathrm{I}(x,y,z,T_\mathrm{I})\phi_\mathrm{L}\big(y,z,0,(4\,\mathrm{mm}-v_\mathrm{PD}t)\big)\,dxdydz\\ &\underbrace{+\left(\frac{3}{7}\right)\left(\frac{1}{3}\right)T_\mathrm{I}\bar{\epsilon}\nu_{ii}(T_\mathrm{I})}_{T_\mathrm{Heat}}\end{aligned} \tag{3.12}$$

$$\dot{N}_{\mathrm{I}} = \sigma_{\mathrm{PD}} N_{\mathrm{I}} \int_{-\infty}^{\infty} \rho_{\mathrm{I}}(x,y,z,T_{\mathrm{I}}) \phi_{\mathrm{L}}\big(y,z,0,(4\,\mathrm{mm} - v_{\mathrm{PD}} t)\big)\, dx\, dy\, dz - k_{\mathrm{bgd}} N_{\mathrm{I}} \tag{3.13}$$

where σ_{PD} is the absolute photodetachment cross-section of OH^- at $\lambda = 662\,\mathrm{nm}$ measured as $8.5(1)_{\mathrm{stat}}(3)_{\mathrm{sys}} \cdot 10^{-18}\,\mathrm{cm}^2$ in [180], ρ_{I} is the ions' spatial density distribution determined via photodetachment tomography, ϕ_{L} is the time-dependent photon flux, V_{OH^-} is the sum of the axial and radial potential approximated by a harmonic and a r^6 potential respectively. The ion-ion heating rate T_{Heat}, is dependent on the ion-ion collision rate ν_{ii} [204] and $\bar{\epsilon}= 0.045(6)$ is the mean relative energy exchange per collision. The background loss rate without the presence of a laser beam is represented by $k_{\mathrm{bgd}} = 0.009(1)\,\mathrm{s}^{-1}$. A detailed derivation of this theoretical model is discussed in [168]. All the parameters described are determined via independent experimental measurements, thus providing a model free from any fit-parameters. As can be seen in Figure 3.3, the ion temperatures determined experimentally are in agreement with those expected from the theoretical description. The ion numbers are also in a reasonable agreement with the model, only deviating for very slow beam velocities or longer photodetachment times, where ion losses due to rf-induced heating become significant. The highest cooling efficiency is observed for $v_{\mathrm{PD}} = 1.0\ \mathrm{mm\ s}^{-1}$ where a final temperature of 2.2(8) K is achieved in less than four seconds. This is accompanied with an orders-of-magnitude increase in the relative phase-space density and Couloumb coupling parameter, as detailed in [168]. Thus, we attained ion temperatures lower than that obtained via the current state of the art techniques of anion cooling via cryogenic buffer gas. The observation of these novel dynamics would not have been feasible without a method to determine the temperature of the trapped ions as they interact with the laser beam.

In conclusion, in this chapter, we described a thermometry method for ions trapped in an octupole trap, by mapping the ions' temperature to their TOF to the detector. This diagnostic technique can be applied to determine the translational temperature of any ionic species trapped in a multipole ion trap. In addition to the published work, the validity and the limitations of this method are discussed along with an application scenario of the established characterization of the ion temperatures to demonstrate anion cooling via laser-induced forced evaporative processes. This TOF thermometry method is, henceforth, used to determine the ion temperatures in our trap for benchmarking experimental investigations involving anion-atom interactions.

CHAPTER 4

DYNAMICS OF MOLECULAR ANIONS WITH ATOMS

In this chapter, the collision dynamics between molecular anions and ultracold atoms in a hybrid atom ion trap are discussed, with a key focus on the associative electronic detachment reactive channels. Firstly, the motivation to study these ion-atom collision dynamics is briefly touched upon, followed by the description of the published work on exploring associative detachment in anion-atom reactions where a dipole-bound electron is involved to mediate the reaction between rubidium (Rb) and OH^-. Subsequently, the preliminary results on the preparation and interaction of Rb with hydrated hydroxide molecular anions, $OH^-(H_2O)$ are presented.

4.1 Insights on anion-neutral reaction dynamics

The attractive potential between ions and neutrals substantially exceeds the range of the van der Waals forces acting between two neutral species. Furthermore, many important ion-neutral reactions are exothermic and barrierless. Often this leads to high reaction rate coefficients [205], making ions important protagonists in the chemical network of diverse environments. They are present in a vast range of research fields, from organic chemistry [27, 206] over Earth's ionosphere to the interstellar medium [207, 118, 115]. Most of the ion-neutral reactions are particularly governed by their quantum states, blocking, opening, or promoting reactive processes to reveal diverse chemical phenomena [64].

A chemical process specific to anions is the associative electronic detachment (AED). Here, the excess electron is detached from the anion leading to the formation of a neutral molecule. This class of reactions is one of the main destruction mechanisms of anions in the interstellar medium (ISM) and plays a relevant role as an intermediate step in the creation of complex molecules [115, 116]. With the detection of water clusters and several anions, including OH^-, in the coma of comet Halley [208, 209], investigations into their reaction dynamics with other ionic and/or neutral species would provide important astrochemical insights.

The possibility of a strong dipole moment in these molecular anions facilitates their existence in hostile environments due to increased stability. Already in 1947, a minimum dipole moment required to bind an electron to a polar molecule enabling the formation of a stable anion was predicted by Fermi and Teller [210]. AED reactions forming a stable intermediate anionic complex with a dipole-bound electron, follow related dependencies on the dipole moment. In a collision complex, the dipole moment of the neutral core binding the excess electron changes according to the internuclear configuration. Reaching a stage, with a dipole moment below a critical value, results in the neutralization of the anionic complex by autodetaching the electron and creating a neutral molecule. The coupling of the quantum states of the intermediate dipole-bound anionic complex with the resultant neutral molecule and the electron detached into the continuum renders the theoretical calculations for modeling the AED reaction rather challenging. The core potential approximation chosen to predict the reaction dynamics in such systems is critical [85] and extensive experimental characterization of these AED reactive channels can provide benchmark data and a reference system to improve *ab initio* calculations on anion-neutral collisions.

A detailed experimental and theoretical investigation of the associative detachment reaction between hydroxide anions and rubidium atoms is presented in the following section. The chosen reaction partners provide a model system, to describe the dynamics of any alkali metal undergoing AED reaction with a closed shell anion.

4.2 Associative detachment in anion-atom reactions

As an extension to the work detailed in [162], we study the AED reaction between Rb atoms and OH^- anions for varying fractions of excited rubidium ($5^2P_{3/2}$) in the ensemble. Our experimental findings for the case of ground state rubidium ($5^2S_{1/2}$) are supported with *ab initio* calculations which explain the deviations from Langevin capture rate via the presence of steric effects. In addition to exploring these novel reaction dynamics, studying the reaction rate coefficients as a function of the fraction of excited rubidium in the atomic ensemble in a hybrid atom ion trap also helped us to quantify the ion losses that occur due to the reactive channels present in our system.

My contributions were in the characterization of the experimental setup. I performed the experimental measurements and the subsequent analysis for

determining the reaction rate coefficients and excited state fractions and also prepared the final plots and the manuscript (except the theoretical parts). I was also involved in the discussions regarding the theoretical investigations which were performed by our theory collaborator Dr. Milaim Kas (affl. Deutsches Elektronen-Synchrotron (DESY), Germany). The following manuscript [2] is published in the journal Nature Communications.
Title: **Associative detachment in anion-atom reactions involving a dipole-bound electron.**
Authors: **Saba Zia Hassan**, Jonas Tauch, Milaim Kas, Markus Nötzold, Henry López Carrera, Eric S. Endres, Roland Wester Matthias Weidemüller.
Published in: Nat. Commun. **13**, 818 (2022).
"This is an open-access article distributed under the terms of the Creative Commons CC BY license, which permits unrestricted use, distribution, and reproduction in any medium provided the original work is properly cited."

nature COMMUNICATIONS

ARTICLE

https://doi.org/10.1038/s41467-022-28382-w OPEN

Check for updates

Associative detachment in anion-atom reactions involving a dipole-bound electron

Saba Zia Hassan[1], Jonas Tauch[1], Milaim Kas[2,3], Markus Nötzold[4], Henry López Carrera[1,5], Eric S. Endres[1,4], Roland Wester[4] & Matthias Weidemüller[1]✉

Associative electronic detachment (AED) between anions and neutral atoms leads to the detachment of the anion's electron resulting in the formation of a neutral molecule. It plays a key role in chemical reaction networks, like the interstellar medium, the Earth's ionosphere and biochemical processes. Here, a class of AED involving a closed-shell anion (OH^-) and alkali atoms (rubidium) is investigated by precisely controlling the fraction of electronically excited rubidium. Reaction with the ground state atom gives rise to a stable intermediate complex with an electron solely bound via dipolar forces. The stability of the complex is governed by the subtle interplay of diabatic and adiabatic couplings into the autodetachment manifold. The measured rate coefficients are in good agreement with ab initio calculations, revealing pronounced steric effects. For excited state rubidium, however, a lower reaction rate is observed, indicating dynamical stabilization processes suppressing the coupling into the autodetachment region. Our work provides a stringent test of ab initio calculations on anion-neutral collisions and constitutes a generic, conceptual framework for understanding electronic state dependent dynamics in AEDs.

---

[1] Physikalisches Institut, Ruprecht-Karls-Universität Heidelberg, 69120 Heidelberg, Germany. [2] Département de Chimie, Faculté des Sciences, Université Libre de Bruxelles (ULB), 1050 Brussels, Belgium. [3] Deutsches Elektronen-Synchrotron (DESY), 22607 Hamburg, Germany. [4] Institut für Ionenphysik und Angewandte Physik, Universität Innsbruck, 6020 Innsbruck, Austria. [5] Present address: Universidad de Las Fuerzas Armadas ESPE, 171103 Sangolquí, Ecuador. ✉email: weidemueller@uni-heidelberg.de

Anions are ubiquitous in nature, from aqueous solution[1] and the earth's atmosphere[2] to astrochemical environments[3–5]. They are reactive species, very sensitive to their environment, and often essential intermediates in important chemical events[6]. An important reactive process, distinguishing reactions involving anions from those involving cations or neutrals, is associative electronic detachment (AED), $A + B^- \rightarrow AB + e^-$, which leads to the formation of a neutral molecule. The reaction is energetically allowed if the dissociation energy of AB is greater than the electron affinity of B. Given their universality, investigations of AED have led to profound understanding of phenomena in diverse chemical reaction networks. In the interstellar medium, AED is assumed to be one of the main destructive mechanisms of astrochemically relevant anions[7]. It serves as an intermediate step in the creation of complex molecules[5,8], contributes to the production of molecular hydrogen[9] and the formation of interstellar water[10]. Furthermore, AED also plays a critical role in the formation of prebiotic molecules[11–13]. Extensive theoretical studies on the dynamics of AED exist for various systems, including halogen anions colliding with hydrogen[14], the creation of hydroxyl molecules from O^- and hydrogen[15], the collisions of Li + $H^{-[}$[16], and the fundamental reaction H + $H^{-[}$[9,17]. In contrast, detailed experimental studies are limited to only few examples exploring reaction paths to the destruction of astrochemically relevant anions[2,7,9,17].

Our work presents a detailed experimental investigation on the AED reaction dynamics between hydroxyl anions (OH^-) and a cloud of laser-cooled ^{85}Rb atoms, in a hybrid atom-anion trap. The AED process in this system involving a closed-shell anion and a single active electron atom is characterized by the emergence of an intermediate dipole-bound complex. Unlike valence-bound anions where the electron is characterized by dense, localized and multiply occupied orbitals, the excess electron in a dipole-bound anion lies in a very diffuse, singly-occupied orbital[18–20]. Historically, dipole-bound anions went from just being a theoretical curiosity to becoming identified as important species in various chemical processes, e.g electron capture in neutral molecules[21,22], zwitterion chemistry which plays an important role in amino acids[23] and charge transfer processes[24,25]. In astrochemistry, dipole-bound anions have been invoked as important precursors to the formation of valence-bound anions[26], and as candidates for the explanation of diffuse interstellar bands[27,28]. For our system, the intermediate dipole-bound anion exhibits a stable ground state and a short-lived excited state, resulting in a vastly different dynamics of the AED reaction.

Over the last years, the study of controlled ion-neutral reactions has enabled insights into the collisional dynamics and the investigation of chemical phenomena at their most elementary level[29–32]. However, most work focused on cationic and neutral systems, leaving out important collisions and reactions involving negative ions[33]. Also, a comprehensive experimental study of the electronic state-dependence in controlled reactions is largely unexplored.

In our work, making use of state-of-the-art techniques for trapping of ions and atoms[31,34], we can precisely control the amount of excited rubidium, allowing us to explore the influence of the electronic state on the anion-neutral reaction dynamics. The observed experimental results are compared to predictions of the Langevin classical capture model[35] and ab initio calculations performed for the Rb–OH^- system[36,37]. As we show, the Langevin model fails to explain the reaction dynamics for both the ground and excited state. In contrast, the ab initio calculations, including steric effects, yield good quantitative agreement with the observed reaction rate coefficients for the ground state and provide a qualitative interpretation for the dynamics involving the excited state.

Results

Theoretical description of associative electronic detachment. The only energetically accessible loss channel for Rb in the ground state is the AED reaction $Rb(^2S) + OH^- \rightarrow RbOH + e^-$, as theoretically investigated in[36,37]. For excited Rb, there are additional loss channels, of which the AED channel dominates (see Supplementary Note 4). In order to understand the underlying mechanism involved in the measured loss processes, we apply a modified Langevin capture model which takes into account that the AED is energetically allowed only for a finite range of angles of approach. For the ground state complex, the crossing between the anionic and neutral the potential energy surface (PES) occurs only at short range and not at long or intermediate internuclear distances due to the weak binding of the dipolar intermediate complex[36,37]. The PESs of the ground and low-lying electronic excited states of the anion Rb–OH^- and neutral Rb–OH collisional complex have been calculated using ab initio methods (for details see Methods and Supplementary Note 1). A 1D cut of the PES at an exemplary collisional angle of $\theta = 80°$ is shown in the left panel of Fig. 1a. The region for which the energy of the anion is larger than the energy of the neutral (when the anion PES intersects the neutral one) is defined as the autodetachment region (gray shaded area).

The ground state of the intermediate complex Rb–OH^- (blue curve in Fig. 1a) is stable against autodetachment as its energy lies below the neutral one. It can be categorized as a dipole-bound state, despite its rather large detachment energy (≈0.3 eV)[38]. The autodetachment region can only be reached for a limited angular space in the repulsive part of the PES (see the two cases of $\theta = 80°$ and 0° in Fig. 1a, where the crossing is energetically inaccessible and accessible respectively). Thus, a much lower reaction rate than the upper bound given by the Langevin capture rate is to be expected.

More quantitatively, based on our ab initio calculations (see[36]), the reaction path for the AED reaction is shown in Fig. 1b. The reaction starts with the $Rb + OH^-$ reactants, with the excess electron occupying a valence-bound π-orbital. The shape of the HOMO changes drastically when the reaction proceeds to the formation of the Rb–OH^- intermediate complex exhibiting the typical halo shape of a dipolar bound complex. The stability of a dipole-bound anion primarily depends on the dipole moment of the core. The dipole moment of the Rb–OH decreases with decreasing interatomic distance R_{Rb} (as shown in the Supplementary Fig. 2). Thus, a crossing with the energy of the neutral state can only occur in the repulsive inner region of the PES (see Fig. 1a, right panel).

As the dipole moment increases with θ, the anionic states become stabilized beyond a critical threshold value, which defines the angular space fraction ρ, in which the AED reaction occurs (see Methods for details). For $\theta < 20°$ (dashed blue levels shown for $\theta = 0°$), the energy crossing is found below the entrance channel threshold opening the AED channel (blue dot in Fig. 1a right panel). For $\theta \gtrsim 20°$ (solid blue levels shown in Fig. 1b at R_c for $\theta = 80°$) the crossing becomes inaccessible. In this case, ρ is rather small, leading to a large deviation from the capture theory. The steep rising potential in the repulsive region, leads to a reaction probability highly sensitive to the ab initio methods and, in particular, to the effective core potential used[36,37]. As shown in Table 1, we find a reaction rate to be a factor of ten smaller than the Langevin rate employing the best available effective core potential for Rb. The calculation for the Langevin capture rate is described in Supplementary Note 3.

The electronic states of the dipole-bound intermediate complex, that are embedded into the autodetachement region, correlate to the excited entrance channel $Rb(^2P) + OH^-$ (red curves in Fig. 1a).

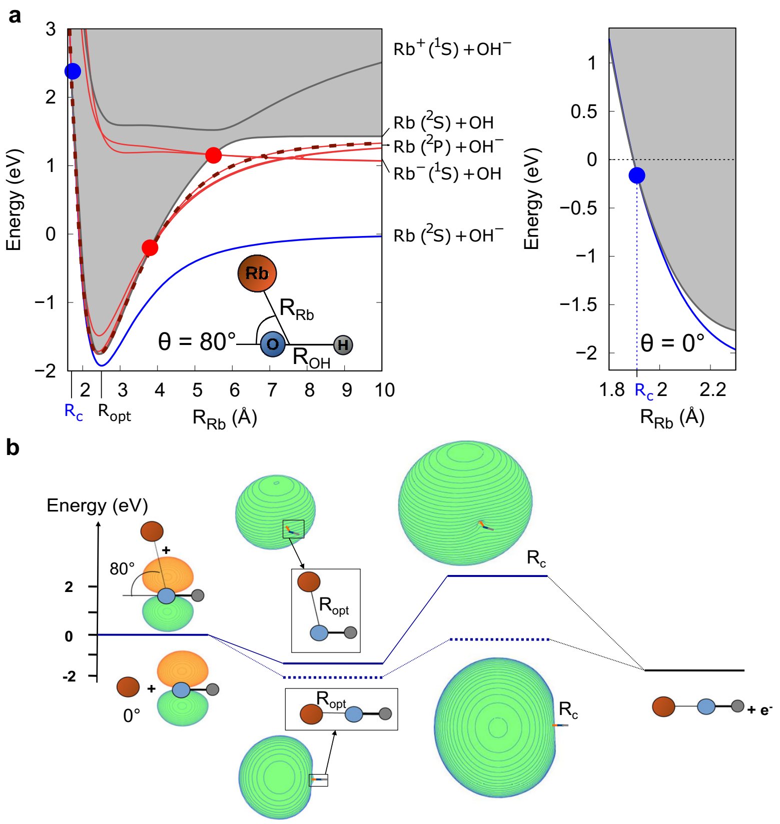

Fig. 1 Description of the Rb-OH$^-$ system. a Potential energy surfaces as a function of the distance R_{Rb} between the Rb atom and the center of mass of O-H (left panel). The angle θ between the OH axis and the Rb atom is chosen to be 80°. The diabatic crossing between the excited state RbOH$^-$ complex (red curves) and its neutral counterpart RbOH (gray curve), is indicated by the two red dots. The crossing for the ground state RbOH$^-$ complex occurs at the inner part of the potentials (blue dot). R_{opt} stands for the optimized R_{Rb} distance (minimum of the interaction well) and R_c corresponds to the distance at which the detachment occurs. The crossing in the repulsive region between the anionic and neutral PES for $\theta = 0°$ is shown in the right panel. **b** Reaction path for the AED reaction between ground state Rb and OH$^-$ shown for two different collisional angles: $\theta = 0°$ (dashed blue line) and $\theta = 80°$ (solid blue line). The zero corresponds to the energy of the Rb+OH$^-$ entrance channel. The orbital corresponding to the excess electron (highest occupied molecular orbital, HOMO) is shown.

Table 1 Comparison of results from the classical capture theory predictions (Langevin) and the ab initio calculations (modified capture model), to the experimentally obtained reaction rate coefficients (at 355 K).

	k_{GS} (10^{-9} cm^3 s^{-1})	k_{ES} (10^{-9} cm^3 s^{-1})
Langevin	4.3	7.2
Ab initio calculations	0.42	7.5
Experiment	0.85(7)	2.1(4)

k_{GS} and k_{ES} are the ground state and excited state reaction rate coefficients, respectively.

Since all possible pathways lead to an energetically accessible crossing into the autodetachment region, which ultimately leads to AED, the total loss rate is expected to be close to the capture rate. Due to the highly diabatic nature of the PESs, the dynamics of the AED reaction can be primarily described as following a single diabatic PES (red dashed curve in Fig. 1a left panel). The excited state of the dipole-bound intermediate complex is short-lived and undergoes spontaneous autodetachment.

However, for increasing collisional angles, the dipole moment increases and the excited state stabilizes similar to the ground state (see Supplementary Fig. 2). In particular, above a critical collisional angle, here $\theta > 150°$, the crossing into the autodetachment region occurs at an energy higher than that of the entrance channel. This critical collisional angle defines the accessible angular space ρ, for AED with an excited state rubidium and is significantly larger than the ground state case. The calculated loss rate is obtained using appropriate long-range interactions and features of the PES (see Methods). It is found to be close to the Langevin rate (see Table 1), which is explained by the cancellation of additional long-range interaction terms and the reduced accessible angular space.

Measurement of reaction rate coefficients. A mass-selected ensemble of hydroxyl anions OH$^-$ formed via electron attachment is loaded into an octupole radio-frequency wire trap, as schematically shown in Fig. 2a and described in detail in[39,40]. Multipole ion traps feature a large field-free region in the radial direction, thus reducing radio-frequency heating[41]. The hydroxyl ions occupy the vibrational ground state, as all higher vibrational states decay on a millisecond time scale. The kinetic temperature

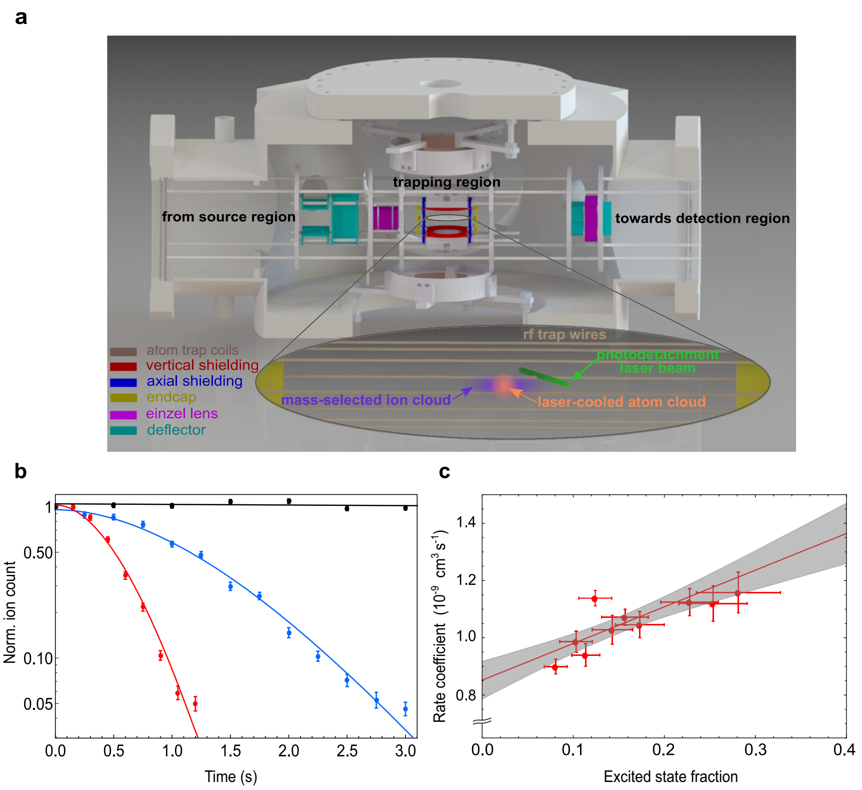

Fig. 2 Hybrid atom-ion system. a The experimental hybrid atom ion trap system. The OH^- ions (purple cloud) are created and loaded from the source chamber and trapped in an octupole radio-frequency (rf) wire trap. A far-threshold laser beam (green) is used to determine the ion density via photodetachment tomography. A laser-cooled cloud of ultracold Rb atoms (orange cloud) is overlapped with the ion cloud. As shown here, the spatial extent of the ion ensemble is significantly larger than that of the atomic cloud. After interaction with the laser or atoms, the time of flight of the ions are extracted onto the detector. **b** The detected normalized OH^- ion count after reaction with the laser-cooled rubidium atoms for excited state fractions of 0.10(2) and 0.28(5) (blue and red data points, respectively). The gray data points depict the ion losses without the presence of rubidium atoms. The ion losses are fitted by Eq. (1) (solid lines). The error bars represent the statistical errors. **c** Reaction rate coefficient as a function of the excited state fraction. The solid red line is a linear fit through the data points. The slope and intercept of the fit yields the reaction rate coefficient for the excited state and ground state rubidium interacting with OH^-, respectively. The gray shaded area represents the 1-σ range of statistical uncertainty.

is set to 355(10) K, via collisions with a pulse of helium buffer gas. The temperature of the ions is measured by mapping the ions' energy distribution to their time-of-flight (TOF) to the detector[40]. The ions' spatial distribution is mapped out by photodetachment tomography with a far-threshold laser[42].

Once the ions are trapped, they are overlapped with an ultracold cloud of rubidium atoms loaded into a dark spontaneous-force optical trap (dark-SPOT) configuration[43]. In the dark-SPOT version of a magneto-optical trap, a part of the repumping laser beam is spatially blocked. By changing the intensity of this laser beam, the fraction of atoms that are pumped back into the cooling cycle is controlled, thus providing control of the fraction of atoms in the excited ($Rb(^2P)$) and ground state ($Rb(^2S)$). After a given reaction time, the number of ions remaining are extracted onto a detector, thus yielding a loss rate dependent on the fraction of electronically excited rubidium in the ensemble.

The ion losses for two different excited state fraction of the atom ensemble, are shown in Fig. 2b. The evolution of the ion number in the ensemble, N_I, is expressed as:

$$N_I(t) = N_I^0 \cdot \exp\left(-\mathrm{k}\int_0^t \Phi_{IA}(t')dt'\right)\cdot \exp(-\mathrm{k}_{\mathrm{bgd}}t) \qquad (1)$$

where N_I^0 is the initial ion number, k is the reaction rate coefficient, Φ_{IA} is the spatial overlap between the ion and atom cloud (see Methods) and $\mathrm{k}_{\mathrm{bgd}}$ is the background ion loss rate without the presence of atoms. The ion losses are fitted by Eq. (1) yielding the reaction rate coefficient for the corresponding excited state fraction. By varying the amount of excited Rb in the atomic ensemble, a linear relationship between the reaction rate coefficients and excited state fractions is found as shown in Fig. 2c. From the intercept of a linear fit through the data points, the reaction rate coefficient for Rb in the ground state is obtained as $\mathrm{k}_{\mathrm{GS}} = 8.5(7)\times10^{-10}\,\mathrm{cm}^3\,\mathrm{s}^{-1}$ with the corresponding statistical uncertainty. The slope yields the reaction rate coefficient for excited state as $\mathrm{k}_{\mathrm{ES}} = 2.1(4)\times10^{-9}\,\mathrm{cm}^3\,\mathrm{s}^{-1}$. We estimate a systematic uncertainty of 40% and 60%, respectively, mainly due to the determination of the spatial overlap Φ_{IA} and parameters of the atom cloud.

Discussion

The experimentally observed reaction rate coefficients are compared with the predictions of the classical capture theory and our ab initio calculations (modified capture model) as shown in Table 1.

The reaction rate for the ground state channel obtained from the experimental results shows the expected deviation from the Langevin prediction due to steric effects determining the stability of the intermediate dipolar complex, as previously outlined. The dipole moment drops below the critical threshold only for certain angles of approach for the anion-neutral collision, rendering a substantially reduced angular space where the autodetachment region is accessible. The experimental results confirm our understanding of the AED reaction dynamics, where for the first time, the dominant influence of a dipole-bound state as a critical reaction intermediate is revealed.

In other alkali hydroxide anions, the autodetachment region is predicted to generally lie above the energy of the entrance channel[38]. In such cases, depending on the energy gap between the anionic state and neutral state, diffuseness of the dipole-bound electron, and the reduced mass of the system, the AED rate is essentially determined by the presence of non-adiabatic coupling of the discrete states with the continuum[16,44].

In general, alkali atoms when interacting with non-metal or halogen anionic species, will form complexes with large dipole moment due to the large difference in the electronegativity. These collisional complexes will most likely support dipole-bound excited states. Our results, thus provide a framework for probing the influence of stable dipole-bound states for future studies on anion-neutral reactions.

As shown in Table 1 for the excited state channel, the experimentally determined reaction rate deviates significantly from the capture model as well as the ab initio calculations. This indicates the presence of additional stabilization mechanisms, like, e.g., the presence of longer lived metastable intermediate states in combination with non-adiabatic couplings, not accounted for in the current theoretical model.

In conclusion, we investigate the electronic quantum state-dependent AED rates in the Rb–OH$^-$ system. Through control on the electronic configuration of the rubidium atom, the electronic state of the intermediate dipolar complex is altered and its influence on the collisional detachment process is revealed. The intermediate complex is a dipole-bound anion which exhibits a stable ground state but short-lived excited states. A unifying feature of the reaction dynamics for both the ground and excited state channels is the accessible angular space which governs the probability of the reaction to occur. For the ground state Rb interacting with OH$^-$, the experimentally observed rate deviations from the capture model predictions are explained via the steric effects. Due to the high sensitivity of the reaction rate coefficient on the subtle details of the structure of the intermediate complex, our measurements provide a stringent test for different effective core potential models. However, for the excited state, the measured loss rate is significantly lower than the ab initio and capture model predictions. A deeper theoretical investigation of the excited states of the dipole-bound Rb–OH$^-$ complex is needed to understand this discrepancy. Due to its similarity in the electronic structure of the intermediate complex to other alkali, alkali-earth hydroxides[38], and alkali with hydrated hydroxide[45], this work provides a general experimental framework to investigate state dependent alkali-anion reactions and opens new routes for the understanding of AED reactions.

Methods

- Determination of spatial overlap, $\Phi_{IA}(t)$ With an ion spatial density distribution constant in time (determined via ions' time-of-flight distribution), the evolution of spatial overlap between the ion and atom cloud is governed by the time-evolution of the atom cloud (loading behavior) $n_A(t) = n_A^0\left(1 - \exp\left(-t/\tau_A\right)\right)$, where n_A^0 is the peak atom density and τ_A is the loading time. The volume of the atom cloud governs the boundary of the interaction region. The overlap $\Phi_{IA}(t)$ can be determined as:

  $$\Phi_{IA}(t) = \int \bar{n}_I(x, y, z) \cdot n_A(x, y, z, t) dxdydz \tag{2}$$

  Here, $\bar{n}_I(x, y, z)$ is the unit-integral normalized OH$^-$ density and $n_A(x, y, z, t)$ is the time-dependent atom density distribution. The ion density distribution is determined via photodetachment tomography [46]. The potential landscape arising from the geometry of an octupole wire trap results in the ion density distribution radially proportional to r^{2n-2} (where $n = 4$), and axially represented by a Gaussian profile. The atom cloud exhibits a Gaussian density profile determined via saturation absorption imaging[47,48]. The spatial extent of the ion cloud is much larger than that of the atomic cloud. The number of excited atoms are imaged by fluorescence imaging while the total number of atoms are imaged via saturation absorption imaging. The ratio of the two gives the excited state fraction of the atom cloud.
- Theoretical method: The rate coefficients corresponding to the reaction involving Rb(^{2}P) and OH$^-$ have been obtained using a modified capture model that includes features of the spin-orbit PES (see Supplementary Note 2), along with the following assumptions:

  - Since the rubidium atom is present in its Rb(^{2}P$_{3/2}$) fine state in the trap, the collision with OH$^-$ can either proceed following the 6E$_{1/2}$ or 5E$_{1/2}$ spin-orbit PES of the Rb–OH$^-$ complex. In the first case, the reaction proceeds on a potential that exhibits a barrier (see Supplementary Fig. 4), in the second case the upper limit of the cross section is taken to be the capture cross section σ_Q obtained with the following long-range potential: $V(R) = \frac{-\alpha}{2R^4} + \frac{-Q}{2R^3} + \epsilon\left(\frac{b}{R}\right)^2$ where α and Q are the static polarizability (870 a.u.) and quadrupole moment (26 a.u.) of Rb in its ^{2}P state.
  - The detachment of the excess electron is assumed to be instantaneous when the autodetachment region is reached (sudden approximation).
  - The transition probability between adiabatic potentials have been calculated using the Landau–Zener formula[49].
  - Electronic detachment can only be avoided if the collision takes place along the 2E$_{1/2}$ PES (first excited states of the Rb–OH$^-$ complex) within the angular space $\rho = \frac{1}{2}(1 - cos(\theta_{\max}))$[36], where $\theta_{\max}$ is the collision angle for which it crosses the neutral curve above the energy in the entrance channel. We found $\theta_{\max} \approx 153^\circ$ (see Supplementary Fig. 3).
  - The electronic to kinetic energy transfer reaction rate is expected to be very small. This reaction has therefore been neglected (see Supplementary Note 4).

The total loss cross section from the Rb(^{2}P$_{3/2}$) + OH$^-$($^2\Sigma^+$) entrance channel is given by a sum of the loss from the 5E$_{1/2}$ and 6E$_{1/2}$ channels:

$$\sigma_{loss}(E_c) = \frac{1}{2}\sigma^{6\mathrm{E}_{1/2}}(E_c) + \frac{1}{2}\sigma^{5\mathrm{E}_{1/2}}(E_c) \tag{3}$$

The first and second term are obtained using the following expressions:

$$\sigma^{6\mathrm{E}_{1/2}}(E_c) = \left(1 - P_{NR}(E_c)(1-\rho)\right)\sigma_Q(E_c) \tag{4}$$

$$\sigma^{5\mathrm{E}_{1/2}}(E_c) = \left(1 - P_{NR}(E_c)(1-\rho)\right)\sigma_B(E_c) \tag{5}$$

where $(1-\rho)$ corresponds to the angular space where the crossing into the autodetachment region is avoided, P_{NR} is the Landau–Zener probability to exit through the non-reactive channels Rb(^{2}P$_{3/2}$) + OH$^-$($^1\Sigma^+$) or Rb(^{2}P$_{1/2}$) + OH$^-$($^1\Sigma^+$) (thus 1-P_{NR} is the probability to exit via the charge transfer channel), σ_Q is the capture cross section and $\sigma_B = \pi R_B^2(1 - U_B/E_c)$ is a classical cross section. The latter is given in terms of the largest impact parameters $b_{\max}$ for which the potential barrier is less than the collision energy E_c. $R_B = 34$ a.u. and $U_B = 4.5 \times 10^{-3}$ are the position and height of the potential barrier, respectively (see Supplementary Fig. 4). The rate constant is then obtained by averaging over a Maxwell–Boltzmann distribution:

$$k_{loss} = \sqrt{\frac{8}{\pi\mu(k_b T)^{3/2}}} \int \sigma_{loss}(E_c)\, E_c\, e^{\frac{-E_c}{k_b T}}\, dE_c \tag{6}$$

where μ is the reduced mass of Rb–OH$^-$ system.

Owing to the highly diabatic nature of the PES (i.e small Landau–Zener adiabatic transition probability, (see Supplementary Note 4)), the probability to exit through the charge transfer channel, P_{CT}, is very small, around 1.5% for the relevant collision energies. Therefore $P_{NR} \approx 98.5\%$ and the entire dynamics is controlled by ρ. For $\rho = 1$, $\sigma_{loss} = \frac{1}{2}(\sigma_B + \sigma_Q)$ which leads to a capture case where all collisions that overcome the centrifugal and potential barrier, resulting in AED. For $\rho = 0$, the 2E$_{1/2}$ state is stable against autodetachment (its energy lies below the neutral for all collision angles θ). The total loss is then given by $\sigma_{loss} = \frac{1}{2}(1 - P_{NR})(\sigma_B + \sigma_Q)$. Hence, associative detachment can only occur following the adiabatic states from the entrance channel for which the Landau–Zener probability is $(1 - P_{NR}) = 1.5 \times 10^{-2}$. With the factor of 0.5, the total loss becomes $\sigma_{loss} = 7.5 \times 10^{-3}(\sigma_B + \sigma_Q)$.

Data availability

The data that support the findings of this study are available from the authors upon request.

Code availability

The codes and analysis files that support the findings of this study are available from the authors upon request.

Received: 19 July 2021; Accepted: 27 December 2021;
Published online: 10 February 2022

References

1. Lambert, J. L. *Trace inorganics in water*, vol. 73 of *Adv. Chem. Ser.*, chap. 2, 18–26 (American Chemical Society, 1968).
2. Fehsenfeld, F. C., Albritton, D. L., Burt, J. A. & Schiff, H. I. Associative-detachment reactions of O^- and O_2^- by $O_2(^1\Delta_g)$. *Can. J. Chem.* **47**, 1793–1795 (1969).
3. Bierbaum, V. M. Anions in space and in the laboratory. *Proc. Int. Astron. Union* **7**, 383–389 (2011).
4. Herbst, E. Can negative molecular ions be detected in dense interstellar clouds? *Nature* **289**, 656–657 (1981).
5. Millar, T. J., Walsh, C. & Field, T. A. Negative ions in space. *Chem. Rev.* **117**, 1765–1795 (2017).
6. Simons, J. Theoretical study of negative molecular ions. *Annu. Rev. Phys. Chem.* **62**, 107–128 (2011).
7. Eichelberger, B., Snow, T. P., Barckholtz, C. & Bierbaum, V. M. Reactions of H, N, and O atoms with carbon chain anions of interstellar interest: An experimental study. *ApJ* **667**, 1283–1289 (2007).
8. Jerosimić, S. V., Gianturco, F. A. & Wester, R. Associative detachment (AD) paths for H and CN^- in the gas-phase: astrophysical implications. *Phys. Chem. Chem. Phys.* **20**, 5490–5500 (2018).
9. Kreckel, H. et al. Experimental Results for H_2 Formation from H^- and H and implications for first star formation. *Science* **329**, 69–71 (2010).
10. Plašil, R. et al. Isotopic effects in the interaction of O^- with D_2 and H_2 at low temperatures. *Phys. Rev. A* **96**, 1–8 (2017).
11. Moruzzi, J. L., Ekin, J. W. & Phelps, A. V. Electron production by associative detachment of O^- ions with NO, CO, and H_2. *J. Chem. Phys.* **48**, 3070–3076 (1968).
12. Snow, T. P. et al. Formation of gas-phase glycine and cyanoacetylene via associative detachment reactions. *Astrobiology* **9**, 1001–1005 (2009).
13. Nichols, C. M., Wang, Z.-C., Lineberger, W. C. & Bierbaum, V. M. Gas-phase reactions of deprotonated nucleobases with H, N, and O atoms. *J. Phys. Chem. Lett.* **10**, 4863–4867 (2019).
14. Gauyacq, J. P. Associative detachment and vibrational excitation in the e^--HF system. *J. Phys. B At. Mol. Phys.* **16**, 4049–4058 (1983).
15. Acharya, P. K., Kendall, R. A. & Simons, J. Associative electron detachment: $O^- + H \rightarrow OH + e^-$. *J. Chem. Phys.* **83**, 3888–3893 (1985).
16. Čížek, M., Dvor^ák, J. & Houfek, K. Associative detachment in Li + H^- collisions. *Eur. Phys. J. D* **72**, 66 (2018).
17. Miller, K. A. et al. Associative detachment of $H^- + H \rightarrow H_2 + e^-$. *Phys. Rev. A* **84**, 052709 (2011).
18. Desfrançois, C. et al. Prediction and observation of a new, ground state, dipole-bound dimer anion: The mixed water/ammonia system. *Phys. Rev. Lett.* **72**, 48–51 (1994).
19. Jordan, K. D. & Wang, F. Theory of dipole-bound anions. *Annu. Rev. Phys. Chem.* **54**, 367–396 (2003).
20. Lykke, K. R., Mead, R. D. & Lineberger, W. C. Observation of dipole-bound states of negative ions. *Phys. Rev. Lett.* **52**, 2221–2224 (1984).
21. Skurski, P. & Simons, J. An excess electron bound to urea. III. The urea dimer as an electron trap. *J. Chem. Phys.* **116**, 6118–6125 (2002).
22. Yuan, D.-F. et al. Observation of a π-type dipole-bound state in molecular anions. *Phys. Rev. Lett.* **125**, 073003 (2020).
23. Skurski, P. & Simons, J. An excess electron bound to urea. I. Canonical and zwitterionic tautomers. *J. Chem. Phys.* **115**, 8373–8380 (2001).
24. Vila, F. D. & Jordan, K. D. Theoretical study of the dipole-bound excited states of $I^-(H_2O)_4$. *J. Phys. Chem. A* **106**, 1391–1397 (2002).
25. Yandell, M. A., King, S. B. & Neumark, D. M. Decay dynamics of nascent acetonitrile and nitromethane dipole-bound anions produced by intracluster charge-transfer. *J. Chem. Phys.* **140**, 184317 (2014).
26. Sommerfeld, T. Dipole-bound states as doorways in (dissociative) electron attachment. *J. Phys. Conf. Ser.* **4**, 245–250 (2005).
27. Guthe, F., Tulej, M., Pachkov, M. V. & Maier, J. P. Photodetachment spectrum of l-$C_3H_2^-$: The role of dipole bound states for electron attachment in interstellar clouds. *ApJ* **555**, 466–471 (2001).
28. Simpson, M. et al. Influence of a Supercritical Electric Dipole Moment on the Photodetachment of C_3N^-. *Phys. Rev. Lett.* **127**, 043001 (2021).
29. Smith, W. W. et al. Experiments with an ion-neutral hybrid trap: cold charge-exchange collisions. *Appl. Phys. B* **114**, 75–80 (2014).
30. Côté, R. Chapter two—Ultracold hybrid atom-ion systems. vol. 65 of *Adv. At. Mol. Opt. Phys.*, 67–126 (Academic Press, 2016).
31. Puri, P. et al. Reaction blockading in a reaction between an excited atom and a charged molecule at low collision energy. *Nat. Chem.* **11**, 615–621 (2019).
32. Paliwal, P. et al. Determining the nature of quantum resonances by probing elastic and reactive scattering in cold collisions. *Nat. Chem.* **13**, 94–98 (2021).
33. Dörfler, A. D. et al. Long-range versus short-range effects in cold molecular ion-neutral collisions. *Nat. Commun.* **10**, 5429 (2019).
34. Tomza, M. et al. Cold hybrid ion-atom systems. *Rev. Mod. Phys.* **91**, 035001 (2019).
35. Langevin, P. A fundamental formula of kinetic theory. *Ann. Chim. Phys.* **5**, 245–288 (1905).
36. Kas, M., Loreau, J., Liévin, J. & Vaeck, N. Ab initio study of reactive collisions between Rb(^{2}S) or Rb(^{2}P) and $OH^-(1\Sigma^+)$. *J. Chem. Phys.* **144**, 204306 (2016).
37. Byrd, J. N., Michels, H. H., Montgomery, J. A. & Côté, R. Associative detachment of rubidium hydroxide. *Phys. Rev. A - At. Mol. Opt. Phys.* **88**, 032710 (2013).
38. Kas, M., Loreau, J., Liévin, J. & Vaeck, N. Ab initio study of the neutral and anionic alkali and alkaline earth hydroxides: Electronic structure and prospects for sympathetic cooling of OH^-. *J. Chem. Phys.* **146**, 194309 (2017).
39. Deiglmayr, J., Göritz, A., Best, T., Weidemüller, M. & Wester, R. Reactive collisions of trapped anions with ultracold atoms. *Phys. Rev. A - At. Mol. Opt. Phys.* **86**, 043438 (2012).
40. Nötzold, M. et al. Thermometry in a multipole ion trap. *Appl. Sci.* **10**, 5264 (2020).
41. Wester, R. Radiofrequency multipole traps: Tools for spectroscopy and dynamics of cold molecular ions. *J. Phys. B At. Mol. Opt. Phys.* **42**, 154001 (2009).
42. Hlavenka, P. et al. Absolute photodetachment cross section measurements of the O^- and OH^- anion. *J. Chem. Phys.* **130**, 061105 (2009).
43. Ketterle, W., Davis, K. B., Joffe, M. A., Martin, A. & Pritchard, D. E. High densities of cold atoms in a dark spontaneous-force optical trap. *Phys. Rev. Lett.* **70**, 2253–2256 (1993).
44. Simons, J. Semiquantum expressions for electronically nonadiabatic electron ejection rates. *J. Phys. Chem. A* **102**, 6035–6042 (1998).
45. Kas, M., Loreau, J., Liévin, J. & Vaeck, N. Reactivity of hydrated hydroxide anion clusters with H and Rb: An ab initio study. *J. Phys. Chem. A* **123**, 8893–8906 (2019).
46. Trippel, S. et al. Photodetachment of cold OH^- in a multipole ion trap. *Phys. Rev. Lett.* **97**, 193003 (2006).
47. Höltkemeier, B., Glässel, J., López-Carrera, H. & Weidemüller, M. A dense gas of laser-cooled atoms for hybrid atom-ion trapping. *Appl. Phys. B Lasers Opt.* **123**, 51 (2017).
48. Reinaudi, G., Lahaye, T., Wang, Z. & Guéry-Odelin, D. Strong saturation absorption imaging of dense clouds of ultracold atoms. *Opt. Lett.* **32**, 3143–3145 (2007).
49. Zener, C. Non-adiabatic crossing of energy levels. *Proc. R. Soc. A Math. Phys. Eng. Sci.* **137**, 696–702 (1932).

Acknowledgements

The authors would like to acknowledge Dr. Bastian Höltkemeier for his role in the realization of the experimental setup. This work is supported by the Austrian Science Fund (FWF) through Project No. I3159-N36 and Deutsche Forschungsgemeinschaft (DFG) under Project No. WE/2661/14-1. S.Z.H. acknowledges the support from IMPRS-QD fellowship and HGSFP. M.K. is grateful to the BMBF project MeSoX (Project No. 05K19GUE) for financial support.

Author contributions

R.W. and M.W. conceived the project, S.Z.H., J.T. and H.L.C. performed experimental design and implementation, S.Z.H., M.N. and E.E. analyzed the experimental results, M.K. performed the theoretical investigations, S.Z.H. and M.K. wrote the manuscript. All authors contributed to the editing and revision of the manuscript.

Funding

Open Access funding enabled and organized by Projekt DEAL.

Competing interests

The authors declare no competing interests.

Additional information

Supplementary information The online version contains supplementary material available at https://doi.org/10.1038/s41467-022-28382-w.

Correspondence and requests for materials should be addressed to Matthias Weidemüller.

Peer review information *Nature Communications* thanks the anonymous reviewers for their contribution to the peer review of this work. Peer reviewer reports are available.

Reprints and permission information is available at http://www.nature.com/reprints

Publisher's note Springer Nature remains neutral with regard to jurisdictional claims in published maps and institutional affiliations.

Open Access This article is licensed under a Creative Commons Attribution 4.0 International License, which permits use, sharing, adaptation, distribution and reproduction in any medium or format, as long as you give appropriate credit to the original author(s) and the source, provide a link to the Creative Commons license, and indicate if changes were made. The images or other third party material in this article are included in the article's Creative Commons license, unless indicated otherwise in a credit line to the material. If material is not included in the article's Creative Commons license and your intended use is not permitted by statutory regulation or exceeds the permitted use, you will need to obtain permission directly from the copyright holder. To view a copy of this license, visit http://creativecommons.org/licenses/by/4.0/.

© The Author(s) 2022

Supplementary Information

Associative detachment in anion-atom reactions involving a dipole-bound electron

Saba Zia Hassan[1], Jonas Tauch[1], Milaim Kas[2,3], Markus Nötzold[4], Henry López Carrera[1†], Eric S. Endres[1,4], Roland Wester[4], and Matthias Weidemüller[1*]

[1] *Physikalisches Institut, Ruprecht-Karls-Universität Heidelberg, 69120 Heidelberg, Germany*
[2] *Département de Chimie, Faculté des Sciences, Université Libre de Bruxelles (ULB), 1050 Brusseles, Belgium*
[3] *Deutsches Elektronen-Synchrotron (DESY), 22607 Hamburg, Germany*
[4] *Institut für Ionenphysik und Angewandte Physik, Universität Innsbruck, 6020 Innsbruck, Austria*
[*] *Corresponding author: weidemueller@uni-heidelberg.de*
[†] *Current address: Universidad de Las Fuerzas Armadas ESPE, 171103 Sangolquí, Ecuador*

December 15, 2021

Supplementary Note 1

Ab-initio potential energy surfaces

Multi-configuration approaches have been used in order to obtain the excited potential energy surfaces that correlate to the Rb($P_{3/2}$)+OH$^-$ entrance channel. We have accounted for the spin-orbit coupling using the state interacting method as implemented in the MOLPRO [1] program using the spin-orbit operator from the MDF effective core potential. A total of 6 interacting anionic states and 2 neutral states have been taken into account. A set of state averaged orbitals was obtained by performing multi-configuration calculation on selected configurations [2]. These orbitals were then used to perform configuration interaction using the internally contracted scheme (ic-MRCI) implemented in the MOLPRO program, including the Davidson correction (labelled +Q) [3].

The ic-MRCI+Q has been applied to a set of manually selected configurations, in the C_s point group. The selected configurations have been obtained from a separate SA-CASSCF calculation on the four A$'$ and two A$''$ low lying electronic states of the RbOH$^-$ molecular complex, taken in its optimized geometry (linear geometry). The active space covers $9a'$ and $3a''$ molecular orbitals (MO).

Singly excited configurations were found to be dominant contributors in the CI expansion. This is expected from electronic configurations consideration. The ground-state electronic configuration is $1a'^2 2a'^2 3a'^2 1a''^2 4a'^2 5a'^2 6a'^2 7a'^2 2a''^2 8a'^1$, where the $1a'$, $2a'$ and $3a'$ MOs correspond to the $1s_O$, $4s_{Rb}$ and $2s_O$ atomic orbital (AO), respectively, the $4a'$, $1a''$, $5a'$ and $6a'$, $7a'$, $2a''$ MOs are mainly formed by the $4p_{Rb}$ and $2p_O$ AOs, respectively, and the $8a'$ MO is mainly formed by the $5s_{Rb}$ AO and corresponds to the highest occupied MO (HOMO). In further discussion we will omit the $1a'^2 2a'^2 3a'^2 1a''^2 4a'^2 5a'^2 6a'^2$ inner shell, which will be labelled with brackets [], and only focus on the valence MOs. The first unoccupied MOs, $9a'$, $10a'$ and $3a''$ are mainly formed by the $5p_{Rb}$ AOs, the ground-state electronic configuration becomes $[]7a'^2 2a''^2 8a'^1 9a'^0 10a'^0 3a''^0$. The first four A$'$ and two A$''$ low lying excited states of the RbOH$^-$ molecular complex correlate to the following channels: Rb$^-$(^{1}S)+OH($^2\Pi$), Rb(^{2}S)+OH$^-$($^1\Sigma^+$) and Rb(^{2}P)+OH$^-$($^1\Sigma^+$). Their main electronic configuration correspond to single excitation relative to the ground-state configuration within the valence $7a'2a''8a'9a'10a'3a''$ MOs. The different electronic states along with their main electronic configurations are given in Supplementary Table 1. The dissociation channels at which they diabatically correlate are also depicted. It should be noted that these electronic excited states correspond to shape resonances of the RbOH+e^- collisional system.

Electronic states	**Main electronic config.**	**Dissociation Height**
X ^{2}A’	$[]7a'^2 2a''^2 8a'^1$	Rb(^{2}S)+OH$^-$($^1\Sigma^+$)
2 ^{2}A’⊕1 ^{2}A”	$[]7a'^2 2a''^2 8a'^0 9a'^1 \oplus []7a'^2 2a''^2 8a'^0 3a''^1$	Rb(^{2}P)+OH$^-$($^1\Sigma^+$)
3 ^{2}A’	$[]7a'^2 2a''^2 8a'^0 10a'^1$	
4 ^{2}A’⊕2 ^{2}A”	$[]7a'^1 2a''^2 8a'^2 \oplus []7a'^2 2a''^1 8a'^2$	Rb$^-$(^{1}S)+OH($^2\Pi$)

Supplementary Table 1: The main electronic configurations and dissociation channels of different electronic states are presented.

A particularly interesting feature of the Rb-OH$^-$ collisional complex is the drastic change in the binding nature of the excess electron along the reaction path. The excess electron is first localized on the hydroxyl anion, which is a typical closed shell valence-bound anion, characterized by a compact density, large detachment energies ($\approx$ 1.8 eV) and important electron correlation effects. When the reaction proceed, the Rb atom disturbs the electron cloud, the excess electron becomes more diffuse and less strongly bound where it is primary bound via dipole-charge interaction.

One of the usual difficulties one faces while using standard bound-state quantum chemistry approaches to calculated metastable states embedded in a continuum is that the wave function usually undergoes variational collapses to a neutral + free electron state where the excess electron occupies a very diffuse orbital. Various stabilization schemes can be used to tackle this problem. Here we found out that constraining the reference MCSCF wave function to single excited configurations avoids the convergence problems and allows us to obtain the resonance states even when using diffuse basis set. The potential energy surfaces (PESs) shown in the main text have been obtained with this manually selected MCSCF/ic-MRCI approach using the MDF ECP for Rb along with its *spdfg* companion basis set [4] supplemented by a set of $5s4p3d2fg$ even tempered diffuse functions and the AVQZ basis set for the O and H atom [5].

Using group theory consideration the four $^1\mathrm{A}'$ + two $^1\mathrm{A}''$ electronic states result in six interacting $\mathrm{E}_{1/2}$ spin-orbit (SO) states. The results are shown in Supplementary Figure 1 for $\theta = 80°$. The two insets show the behaviour near the potential well and at dissociation, lower and upper left panels, respectively. The PES of the neutral RbOH ground-state is shown in black line. Our calculation correctly reproduces the SO splitting of the $^2\mathrm{P}_{3/2}$ and $^2\mathrm{P}_{1/2}$ state of Rb, with a calculated value of 26.5 meV which is to be compared to experimental value 29.3 meV [6].

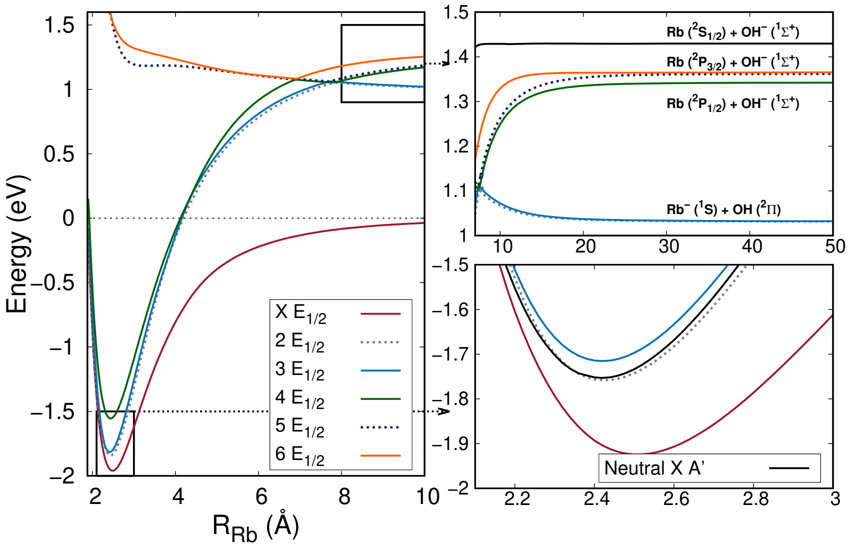

Supplementary Figure 1: Left panel: PESs of the low-lying excited states of the Rb-OH$^-$ molecular complex for $\theta = 80°$, including SO couplings. This leads to 6 interacting $\mathrm{E}_{1/2}$ states. The red curve and other solid colored lines correspond to the adiabatic potential of the ground- and excited-states of the Rb-OH$^-$ collision complex, respectively. The dashed lines correspond to the A” states in the non-relativistic picture. The upper right panel show the PESs of the excited states at dissociation where the relevant channels are depicted. The bottom right panel shows the PESs of the 3 lowest anionic states (red, dashed gray and blue curve) around the potential well alongside the neutral potential (black curve).

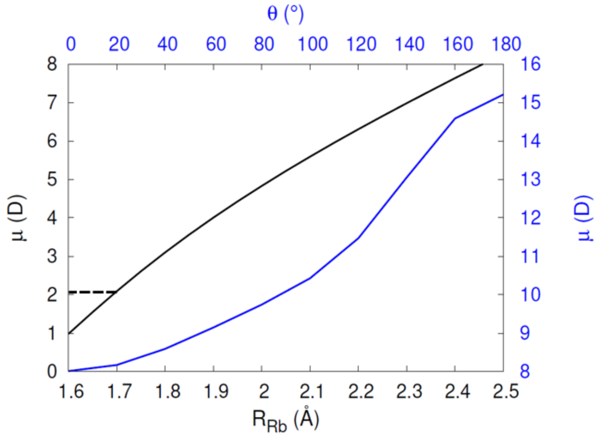

Supplementary Figure 2: Hartree-Fock calculation of the dipole moment of RbOH. The black curve shows the dipole moment μ as a function of internuclear distance $\mathrm{R_{Rb}}$ for $\theta = 0°$. The blue curve shows the dipole moment as a function of collisional angle θ for an optimized internuclear distance. The critical value of the dipole moment ensuring a stable intermediate dipolar complex is indicated by the dashed line.

Supplementary Note 2

Features of the potential energy surface

2.1 Potential well region

Our calculations show that the excited states of the $\mathrm{RbOH^-}$ complex, taken in its equilibrium geometry ($\theta = 0°$) are auto-detaching states, in other words, only the ground state has a positive vertical detachment energy (VDE). However, for larger values of θ dipole moment of the RbOH core increases, leading to a stabilization of the anion. This can be seen in Supplementary Figure 2, where the the Hartree-Fock dipole moment of the RbOH core is depicted as a function of $\mathrm{R_{Rb}}$ for $\theta = 0°$ (black) and as a function of θ at optimized $\mathrm{R_{Rb}}$ distance (blue). As a consequence, the VDE increases for increasing θ. This trend can be seen in Supplementary Figure 3 where the crossing point between the anionic first excited-state $2\mathrm{E}_{1/2}$ PES and the neutral PES is marked by a dot. In particular, for $\theta > 153°$ the crossing with the neutral PES occurs above the $\mathrm{Rb(^2P_{3/2})}$+$\mathrm{OH^-(^1\Sigma^+)}$ entrance channel energy. The later is taken as $E_c + T(\mu, J)$, where E_c and $T(\mu, J)$ are the collision energy and internal energy (vibration and rotation) of $\mathrm{OH^-}$ at $T = 355$K, respectively. This characterizes an accessible angular space where the auto-detachment from the $2\mathrm{E}_{1/2}$ is avoided.

2.2 Long and intermediate range

Although it is difficult to see in the Supplementary Figure 1, the $6\mathrm{E}_{1/2}$ state is repulsive at long range and attractive at intermediate distance, leading to a potential barrier around 14 Å. The barrier can be seen in Supplementary Figure 4 where the PESs for the $6\mathrm{E}_{1/2}$ state for various values of θ have been plotted. The barrier height is almost independent of θ and is about 4.5×10^{-3} eV high. This repulsive state can be related to the classical repulsive potential of a charge-quadrupole interaction [7]. We suspect the presence of a higher lying state, with a repulsive potential at intermediate and short range, that interacts with the $6\mathrm{E}_{1/2}$ state leading to an avoided crossing. We found this state

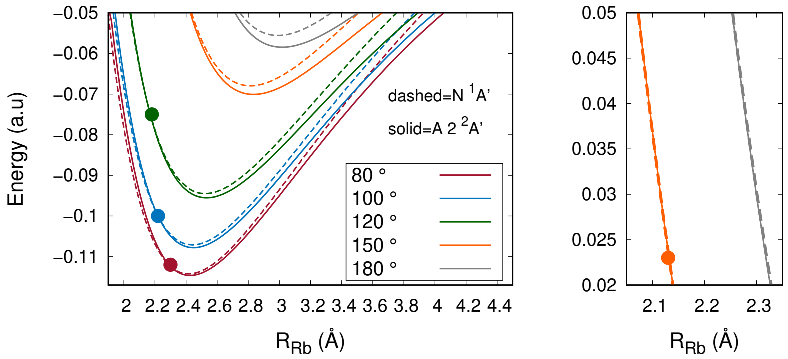

Supplementary Figure 3: PESs for the first excited state of the anion $RbOH^-$ ($2\,^2A'$ or $2\,E_{1/2}$, solid lines) and the ground state of the neutral RbOH molecular complex (dashed lines), for various collision angle θ. Note that the colors corresponds to various values of θ. The right panel shows a zoom-in of the PESs in the repulsive region. The zero energy is taken as the energy of the ground state entrance channel $Rb(^2S)+OH^-$.

to be mainly described by doubly excited electronic configurations, hence it corresponds to a Feshbach resonance of the $RbOH+e^-$ collisional complex. Our approach based on manually selected singly excited configurations is not adequate to describe this additional state. Unfortunately, due to the convergence problems pointed out above, adding even the minimum number of doubly excited configurations needed to describe this additional state results in variational collapses of the wave function. Therefore, specific methods would be needed.

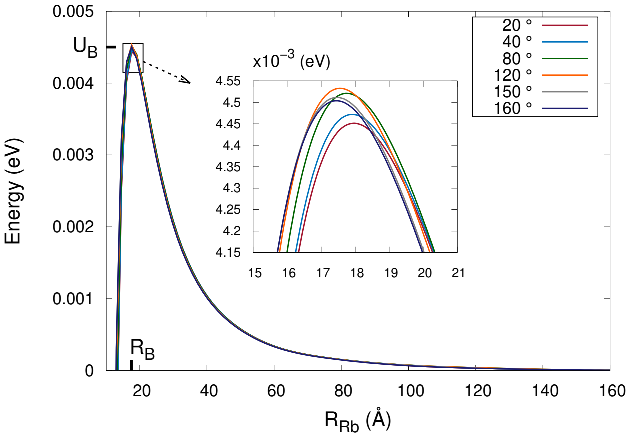

Supplementary Figure 4: Potential barrier along the $6E_{1/2}$ state for various values of θ. The distance R_B is the intermolecular distance R_{Rb} at the potential's maximum value U_B.

Supplementary Note 3

Determination of Langevin reaction rate

In the event of an atom-ion collision, the upper limit to collisional rate constants is given by the classical-mechanics based, Langevin capture model [8]. The long range interaction potential V(r) is dominated by the interaction between charge-induced dipole of the atom with the ion's charge such that:

$$V_{\text{int}}(r) = -\frac{C_4}{r^4} \tag{1}$$

where r is the interparticle separation and $C_4 = \frac{\alpha e^2}{(4\pi\epsilon_0)^2}$ [9]. Here α is the scalar polarizability of the neutral, e is the electron charge and ϵ_0 is the permittivity of free space.
By including the centrifugal potential into the effective potential of the collision complex, the Langevin reaction rate constant k_{L} can be derived as :

$$k_{\text{L}} = 2\pi\sqrt{\frac{C_4}{\mu}} = \frac{e}{2\epsilon_0}\sqrt{\frac{\alpha}{\mu}} \tag{2}$$

where all parameters are in S.I. units.
The scalar polarizabilities and the calculated reaction rate constants for excited and ground-state Rb are summarized as follows:

	α (a.u.) [10]	k_L (10^{-9} cm^3s^{-1})
Rb (^{2}P)	870	7.2
Rb (^{2}S)	318.6	4.3

Note: Conversion factor used for α (from atomic units to S.I. units) [10], 1 a.u. = 1.648773×10^{-41} $\text{C}\,\text{m}^2\,\text{V}^{-1}$.
The modified Langevin model that has been used to calculate the loss rate from the ground and excited state channel averages over the range of angles of approach for which the reaction is exoergic. There are some implicit assumptions in this model, which require some additional discussion

1. The present model assumes that no angle of approach is preferred. Steering effects, i.e. reorientation of the OH^- molecule due to intermolecular forces, start to play a role at low temperatures and would lead to an increase in the likelihood of a "head-on" collision of Rb-O-H, thus increasing the AED rate towards the Langevin rate. Although we do not expect these effects to be dominant in the temperature regime of our experiment, they might partially explain the underestimation of the measured rate coefficient by the *ab initio* calculation.

2. The population of rotational levels in OH^- may not follow a thermal distribution due to collisional cooling with the ultracold buffer gas. However, it has been shown that a lower rotational temperature would actually decrease the measured AED rate [11].

3. As suggested in [12], the presence of vibrational excited OH^- anions will strongly increase the AED loss. Using the dipole moment of OH^-, we find that the lifetime of $v = 1$ state, before radiative decay is on the order of couple of milliseconds, which in comparison to the complete timescale of the experiment ($\sim$ 10 seconds), makes the fraction of ions in the excited vibrational states negligible, as mentioned in the main text.

Supplementary Note 4

Excited-state loss channels

The interaction of hydroxyl anion with excited Rb (^{2}P) opens the following loss channels:

- **Associative electronic detachment (AED):**

$$\mathrm{Rb}(^2\mathrm{P}) + \mathrm{OH}^- \rightarrow \mathrm{RbOH} + \mathrm{e}^-$$

- **Electronic to kinetic energy transfer:**

$$\mathrm{Rb}(^2\mathrm{P}) + \mathrm{OH}^- \rightarrow \mathrm{Rb} + \mathrm{OH}^- + \mathrm{E}_{kin}$$

- **Charge-exchange reaction:**

$$\mathrm{Rb}(^2\mathrm{P}) + \mathrm{OH}^- \rightarrow \mathrm{Rb}^- + \mathrm{OH}$$

4.1 Electronic to kinetic energy transfer

In order to estimate the probability to exit through the electronic to kinetic energy transfer $\mathrm{Rb}(^2\mathrm{P}_{3/2})$+OH$^-$ → $\mathrm{Rb}(^2\mathrm{S})$+OH$^-$ channel, we have calculated the non-adiabatic coupling matrix elements (NACME) between the XE$_{1/2}$ and 2E$_{1/2}$ states, which link to entrance and exit channels. This has been done using the finite difference approach, implemented in MOLPRO. The results can be seen in Supplementary Figure 5. The coupling exhibit the typical bell-shape behaviour of non-crossing states with constant energy spacing. This coupling case can be described by the Rosen-Zener-Demkov model [13, 14] for which the coupling potential is modeled by a hyperbolic secant:

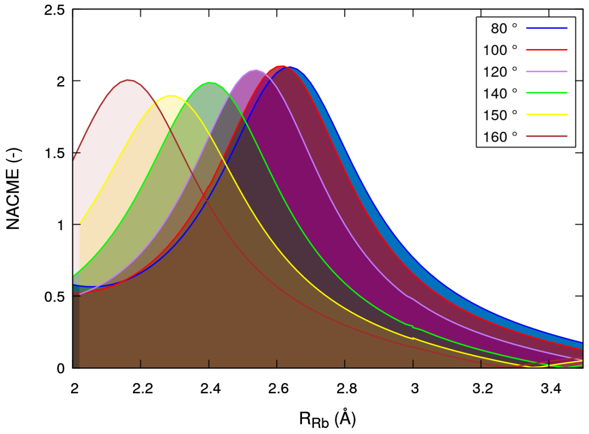

Supplementary Figure 5: Non-adiabatic coupling strength between the XE$_{1/2}$ and 2E$_{1/2}$ states of the Rb-OH$^-$ molecular complex for various θ.

$$V_{12}(\mathrm{R}_{\mathrm{Rb}}) = v_0 sech(\frac{\mathrm{R}_{\mathrm{Rb}} - \mathrm{R}_0}{\beta}) \tag{3}$$

and the probability transition between adiabatic states (in atomic units) is given by

$$P_{12} = sin^2(\pi v_0 \beta) sech^2(\frac{\pi \Delta E \beta}{2\sqrt{2E_k/\mu}}) \tag{4}$$

where ΔE is the energy difference between both non-crossing adiabatic states, E_k is the kinetic energy. The parameters β, $\mathrm{R}_{\mathrm{Rb0}}$ and v_0 were extracted by fitting our NACME calculation. The fitted values are $v_0 = 1.95$, $\mathrm{R}_{\mathrm{Rb0}} = 4.79$ and $\beta = 0.63$. With $\Delta E \approx 7 \times 10^{-3}, E_k \approx 0.056$ we found the non-adiabatic probability transition $P_{12} \approx 0.15\%$ for the relevant collision energies. This small probability is mainly due to the large reduced mass of the system and the larger energy gap between adiabatic states in comparison with the avoided crossing case. This justifies the neglect of the electronic to kinetic energy transfer channel in the dynamics.

4.2 Charge transfer channel

The probability for an adiabatic passage at the various avoided crossings (at $\mathrm{R}_{\mathrm{Rb}} \approx 8$ Å, 7 Å and 4 Å in Supplementary Figure 1, left panel) is estimated using the Landau-Zener formula:

$$P_{12} = exp(\frac{\pi(\Delta E)^2}{2\Delta F\sqrt{(2E_k/\mu)}}) \tag{5}$$

where ΔE and E_k are the energy gap and kinetic energy at the avoided crossing point respectively, μ is the reduced mass and ΔF is the difference in the slope between the two diabatic curves. We found the diabatic transition probability P_{12} to be close to one for the relevant collision energies. This is primarily due to the small energy gap between the adiabatic states. Typical value of P_{12} are found to be around 0.95.

The probability to exit via the charge transfer channel Rb^-+OH is given by $P_{CT} = 1 - P_{NR}$, where P_{CT} is obtained by summing the probabilities associated to different paths that lead to the non-reactive channel. Owing to the highly diabatic nature of the PES (*i.e* small Landau-Zener adiabatic transition probability, see above), P_{CT} is very small, around 1.5% for the relevant collision energies. Since the loss from the electronic to kinetic energy transfer channel is also found to be small, the AED reaction is predicted to be the dominant loss channel.

Supplementary References

[1] Berning, A., Schweizer, M., Werner, H.-J., Knowles, P. J. & Palmieri, P. Spin-orbit matrix elements for internally contracted multireference configuration interaction wavefunctions. *Mol. Phys.* **98**, 1823–1833 (2000).

[2] Knowles, P. J. & Werner, H.-J. Internally contracted multiconfiguration-reference configuration interaction calculations for excited states. *Theor. Chim. Acta* **84**, 95–103 (1992).

[3] Langhoff, S. R. & Davidson, E. R. Configuration interaction calculations on the nitrogen molecule. *Int. J. Quantum Chem.* **8**, 61–72 (1974).

[4] Lim, I. S., Schwerdtfeger, P., Metz, B. & Stoll, H. All-electron and relativistic pseudopotential studies for the group 1 element polarizabilities from K to element 119. *J. Chem. Phys.* **122**, 104103 (2005).

[5] Dunning, T. H. Gaussian basis sets for use in correlated molecular calculations. I. The atoms boron through neon and hydrogen. *J. Chem. Phys.* **90**, 1007 (1989).

[6] Sansonetti, J. E. Wavelengths, Transition Probabilities, and Energy Levels for the Spectra of Rubidium (Rb I through Rb XXXVII). *J. Phys. Chem. Ref. Data* **35**, 301 (2006).

[7] Mies, F. H. Molecular theory of atomic collisions: Fine-structure transitions. *Phys. Rev. A* **7**, 942–957 (1973).

[8] Langevin, P. A fundamental formula of kinetic theory. *Ann. Chim. Phys.* **5**, 245 (1905).

[9] Vogt, E. & Wannier, G. H. Scattering of ions by polarization forces. *Phys. Rev.* **95**, 1190–1198 (1954).

[10] Mitroy, J., Safronova, M. S. & Clark, C. W. Theory and applications of atomic and ionic polarizabilities. *J. Phys. B: At. Mol. Opt. Phys.* **43**, 202001 (2010).

[11] Kas, M., Loreau, J., Liévin, J. & Vaeck, N. Ab initio study of reactive collisions between Rb(^{2}S) or Rb(^{2}P) and OH$^-$($1\Sigma^+$). *J. Chem. Phys.* **144**, 204306 (2016).

[12] Byrd, J. N., Michels, H. H., Montgomery, J. A. & Côté, R. Associative detachment of rubidium hydroxide. *Phys. Rev. A - At. Mol. Opt. Phys.* **88**, 032710 (2013).

[13] Nikitin, E. E. Nonadiabatic transitions what we learned from old masters and how much we owe them. *Annu. Rev. Phys. Chem. 1999.* **50**, 1 (1999).

[14] Desouter-Lecomte, M. & Lorquet, J. C. Nonadiabatic interactions in unimolecular decay. II. Simplified formalism. *J. Chem. Phys.* **66**, 4006–4017 (1977).

4.3 Effect of hydration on hydroxide anions

The reaction rate coefficients determined for AED in the Rb-OH^- system provide critical insights into the feasibility of sympathetic cooling of the anions using ultracold atoms. As rubidium, even in its ground state undergoes an AED reaction with OH^-, this results in loss of ions before they can be cooled considerably via elastic collisions with the atoms. In the perspective of sympathetic cooling, the reactive collisions are thus termed "bad collisions" whereas the elastic collisions leading to anion cooling are considered to be "good collisions". The ratio of good-to-bad collisions influences the efficiency of anion sympathetic cooling.

This efficiency is also governed by the mass ratio ξ, i.e., the ratio of the mass of the coolant atom to the mass of the anionic species to be cooled. While it was long-established, that efficient ion cooling via atoms is limited to systems with $\xi < 1$, recent theoretical and experimental studies have opened new regimes of ion cooling in systems with $\xi > 1$ [67, 163, 164]. These insights motivated the investigation of collision dynamics between rubidium and hydrated hydroxide anions, $OH^-(H_2O)$, where a more favorable mass ratio is expected to increase the efficiency of anion sympathetic cooling via collisions with an ultracold buffer gas.

In this section, the preliminary results on the interactions between Rb and $OH^-(H_2O)$ are discussed as follows. Firstly, the production and preparation of the ion cloud are briefly discussed. Subsequently, the experimental results on the collisional dynamics of Rb and $OH^-(H_2O)$ molecular anions are shown.

4.3.1 Preparation of ion cloud

As discussed in Chapter 3, the argon gas seeded with water vapor used for the production of hydroxide anions also results in the production of hydrated hydroxide anions. A detailed experimental characterization for the production of different orders of hydrated hydroxide anions $OH^-(H_2O)_l$ (where $l \in \mathbb{N}$) is presented in [175]. After the production, the ions enter a Wiley-McLaren (WML) acceleration stage, which corrects the spread in the different starting positions of the ions to the first order. This allows distinguishing ions of different mass-to-charge ratios based on their different time of flights, with the WML improving the mass resolution. The heavier the mass of the ion, the later is its arrival time. Finally, a deflector before the trap and the entrance endcap can be independently adjusted for the final selection of the ion species of interest, for its loading, and subsequent trapping in the ion trap.

Depending on the ions' mass, charge, and the corresponding time of flight (TOF) to the detector, for the species whose TOF is known, (here, O^- and OH^-), one can determine the time where the hydrated anions are expected. In the case of OH^-, we also trapped O^- ions due to the small difference, in the mass-to-charge ratio between the two species, which makes it unfeasible to separate the ions in their time domain. Analogous to this system, we also expect to trap both $O^-(H_2O)$ and $OH^-(H_2O)$ ions. The simulated time of flight distributions of different ionic species are shown in Figure 4.1, after the extraction of ions onto the detector. The ions' TOF to the detector is estimated similarly to the ion extraction simulation discussed in Chapter 3.

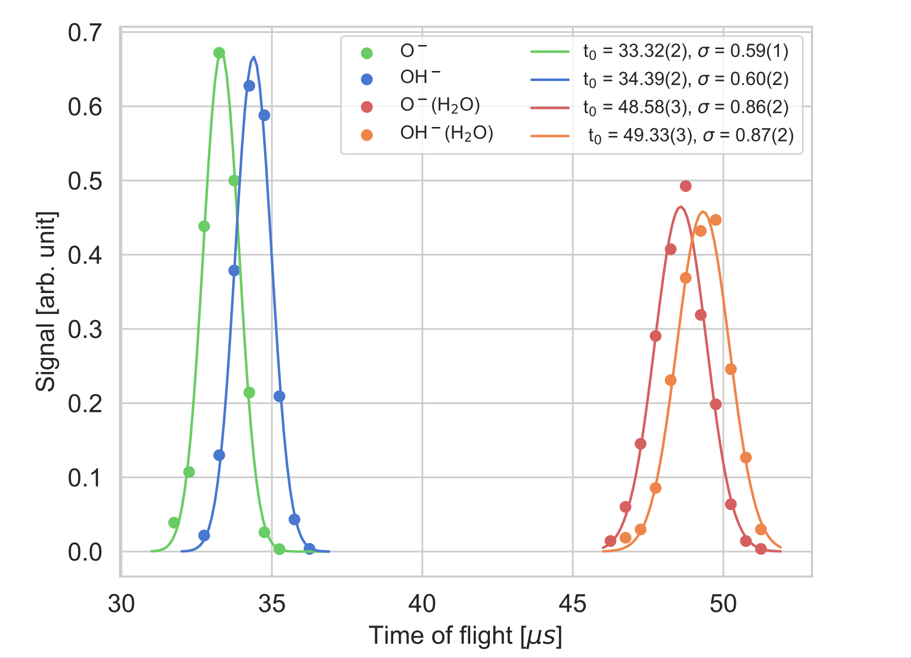

Figure 4.1: Simulated time of flight distributions (normalized) of O^- and OH^- and their hydrated counterparts $O^-(H_2O)$ and $OH^-(H_2O)$ are shown. The solid points correspond to the binned arrival time of an ion cloud extracted from the trap. The solid lines correspond to a Gaussian distribution fitted to the data points, centered about t_0 with a width of σ.

As expected, when the ions are loaded into the trap, in addition to the desired $OH^-(H_2O)$ ions, other ionic species with a similar mass-to-charge ratio also enter the trap. In our setup, in addition to $OH^-(H_2O)$ ions, we trapped O_2^- and $O^-(H_2O)$ anions with an electron affinity of 0.43 eV and 2.6 eV respectively [211]. A photodetachment laser beam with $\lambda = 450$ nm ($E_\gamma = 2.75$ eV) would thus detach the O_2^- and $O^-(H_2O)$ species while only the $OH^-(H_2O)$ ion species, which has an electron affinity of 2.95 eV, is retained in the trap. As the O_2^- anions were produced in large quantities, a high power photodetachment beam at $\lambda = 660$ nm ($E_\gamma = 1.88$ eV) is additionally used to increase the photodetachment rate. The measured time of flight distributions of the ions, due to their interactions with the various photodetachment laser beams are shown in Figure 4.2. It should be noted that the width of the symmetrical distribution (blue) is determined to be $\sigma = 0.973(3)\,\mu$s by fitting a Gaussian function to the measured data points. This is broader than the width expected from the simulation shown in Figure 4.1. The reason for the broadening of the width is attributed to the presence of other ionic species and will be discussed in the following section.

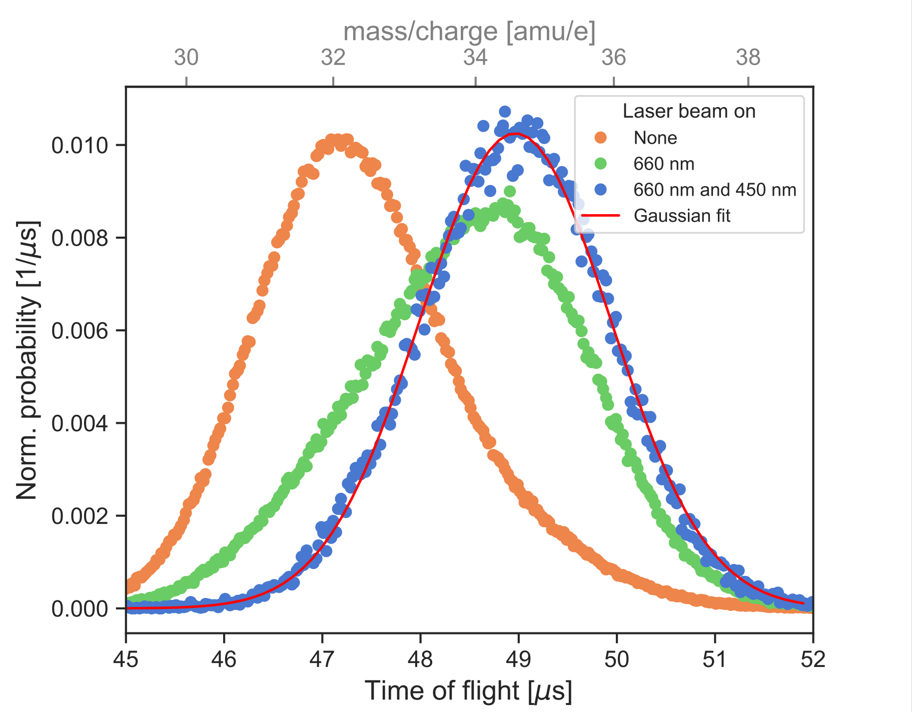

Figure 4.2: Ion separation via interaction with photodetachment (PD) laser beams. The experimentally measured normalized time of flight distribution for different ion clusters is shown. The orange distribution corresponds to an ion cloud comprising three ion species, O_2^-, $O^-(H_2O)$, and $OH^-(H_2O)$ (i.e., with no laser beam switched on). With the 660 nm laser beam ($E_\gamma = 1.88$ eV) switched on, the O_2^- ions are detached (green distribution). With an additional 450 nm photodetachment laser beam ($E_\gamma = 2.75$ eV), both O_2^- and $O^-(H_2O)$ anions are detached from the ion cloud (blue distribution). The asymmetry of the orange and green distribution points to the presence of different ion species present in the ion cloud, whereas a rather symmetrical distribution (blue), is observed with both the photodetachment laser beams on. The red solid curve is a Gaussian fit to the measured distribution. The secondary x-axis (top axis shown in gray) represents the ion's mass-to-charge ratio corresponding to its TOF to the detector.

4.3.2 Qualitative description of anion cooling via ultracold atoms

After an ensemble of $OH^-(H_2O)$ ions has been prepared as discussed in the previous section, the ions are now overlapped with an ultracold cloud of ^{85}Rb atoms, created at the center of the ion cloud. As a result of this overlap, the atoms and ions undergo different kinds of collisions. Our primary interests are, firstly the elastic collisions, which result in the sympathetic cooling of ions, and secondly, the reactive processes which are the main ion loss channels as seen in the $RbOH^-$ system. The trapped ions' translational temperature is mapped onto the ions' time of flight to the detector, where the variance of ions' TOF distribution is directly proportional to the temperature of trapped ions. The time of flight distributions of the ion cloud as a function of different interaction times with the atom cloud is shown in Figure 4.3.

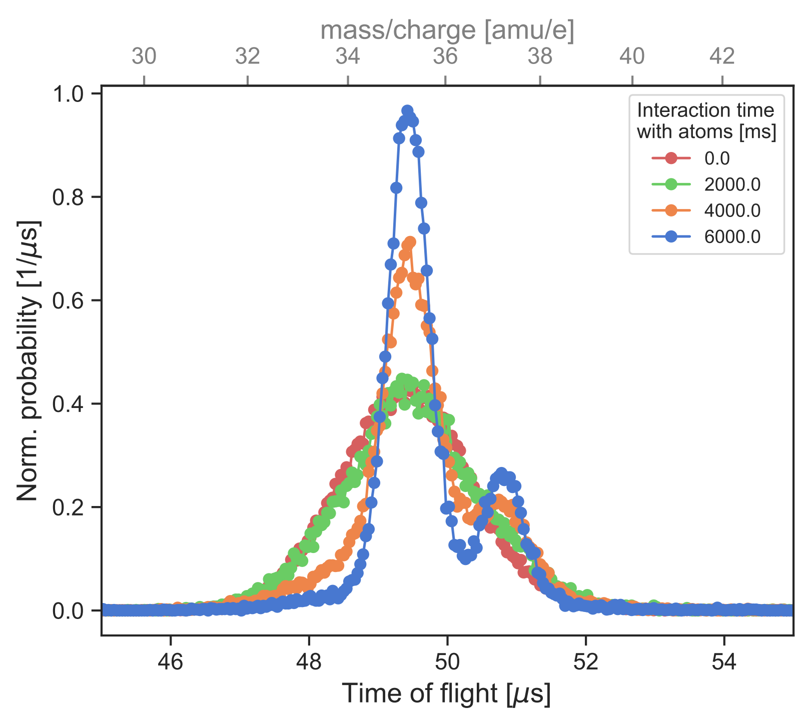

Figure 4.3: Overlap of $OH^-(H_2O)$ anions with ultracold Rb. The experimentally measured normalized time of flight distributions of the ions for different interaction times with the atom cloud are shown. The shrinking of the ions' time of flight distribution is caused by the sympathetic cooling of ions via ultracold atoms. However, the emergence of a shoulder or a second peak indicates the presence of other anionic species in the trap. The solid points are the experimentally measured distribution. The solid lines are a guide to the eye. The secondary x-axis (top axis shown in gray) represents the ion's mass-to-charge ratio corresponding to its TOF to the detector.

We see a clear shrinking of the ions' time of flight distribution, due to the sympathetic cooling of the ions with atoms. However, for longer interaction times with the atoms, one can also see a second peak arising in the form of a shoulder. This indicates the presence of other ionic species with a mass-to-charge similar to that of hydrated hydroxide anions.

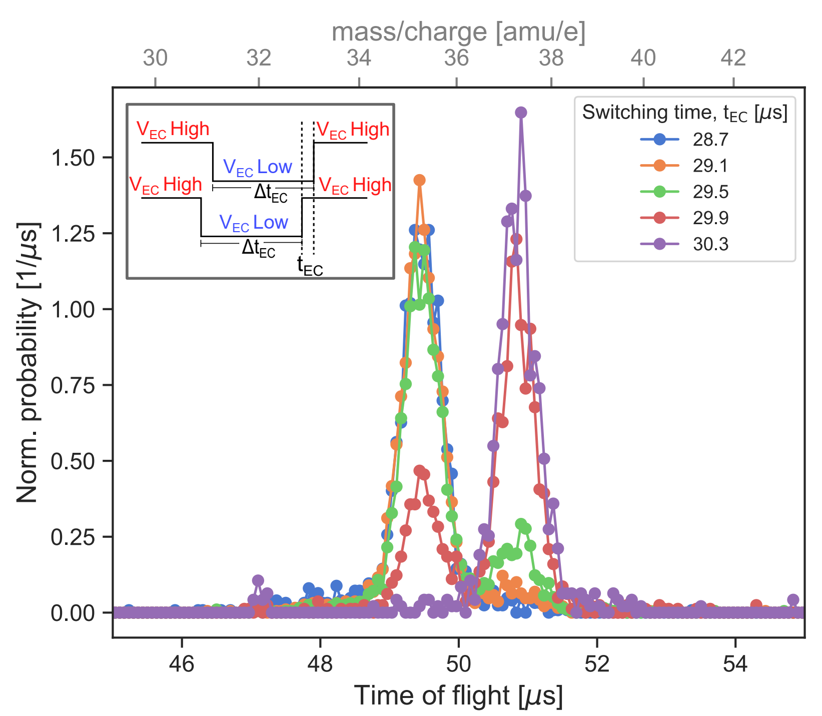

Figure 4.4: Scanning ion loading parameters. Ions' normalized time of flight distributions are shown for different switching times of the entrance endcap. The inset shows the schematic representation of the switching of the static potential V_{EC}, applied to the endcap. When V_{EC} is high, the ions cannot pass through the endcap into the trap, when V_{EC} is low, the ions can be loaded into the trap after which the endcap is at a higher trapping potential again at time t=t_{EC}. We vary this time parameter t_{EC} to change the loading of ions into the trap. The duration for which the endcap remains on a lower potential is given by Δt_{EC}, which remains the same for all the measurements. For a later time instance t_{EC}, we see the emergence of a second ion species, different from $OH^-(H_2O)$, which is loaded into the trap. The solid points are the experimentally measured distribution. The solid lines are a guide to the eye. The secondary x-axis (top axis shown in gray) represents the ion's mass-to-charge ratio corresponding to its TOF to the detector.

As previously discussed in Chapter 2, the ions are mass-selected by changing the times for which the potential on the endcap electrodes is switched on. If the shoulder in the time of flight distribution at longer interaction times, is a result of loading another ion species in the trap, it should be possible to modify the amplitude of this peak by scanning the switching timings for the entrance endcap. As the time of arrival for the two ionic species is too close and we could only see the emergence of the second peak in the presence of the atoms, we let the ion cloud interact with the atoms for 7000 ms for different switching times t_{EC}, which defines the point in time at which the endcap potential is switched from a loading (V_{EC} Low) to a trapping potential (V_{EC} High).

The resulting distributions are shown in Figure 4.4. It can be seen that it is possible to enhance/suppress the second peak by tuning the endcap parameters to selectively load ion species in the trap. Thus, it can be concluded that the second peak is not a cooling artifact but stems from a different ionic species created in the source. Though only water seeded in argon is used in the source, this second species might be created by ablation from the many Teflon and PEEK insulators used in the plasma discharge source. However, the exact source of this other ionic species in the trap could not be conclusively identified.

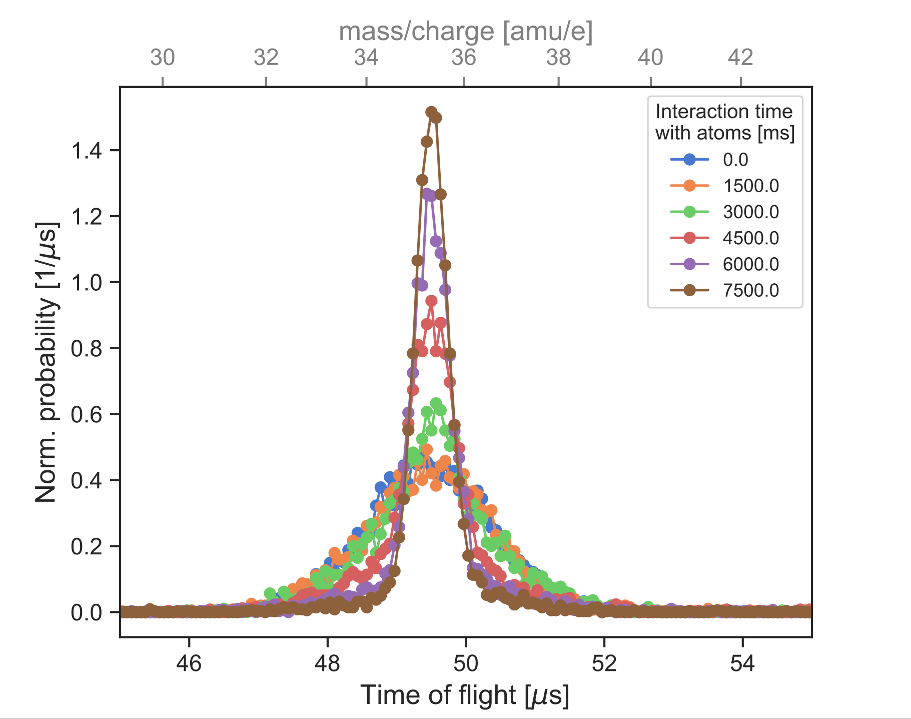

Figure 4.5: Sympathetic cooling of $OH^-(H_2O)$ with ultracold rubidium. The ions' normalized time of flight distributions are plotted for different interaction times with the ultracold atom cloud. The points are experimentally measured data points and the solid curves are a guide to the eye. The secondary x-axis (top axis shown in gray) represents the ion's mass-to-charge ratio corresponding to its TOF to the detector.

In order to minimize the number of ions of this other species that is loaded into the trap, we changed the switching timings of the deflector before the trap and the entrance endcap electrodes to maximize the loading of $OH^-(H_2O)$ anions into the trap. Subsequently, the ion cloud is again overlapped with the atom cloud for different interaction times. The ions' time of flight distributions are recorded as shown in Figure 4.5. A Gaussian fit to the ion distribution at $t = 0$ s gives the width as $\sigma = 0.893(8)\,\mu$s, which is now in agreement with the width expected from the simulations shown in Figure 4.1. The broadened TOF width seen in Figure 4.2 was a result of the presence of other ionic species.

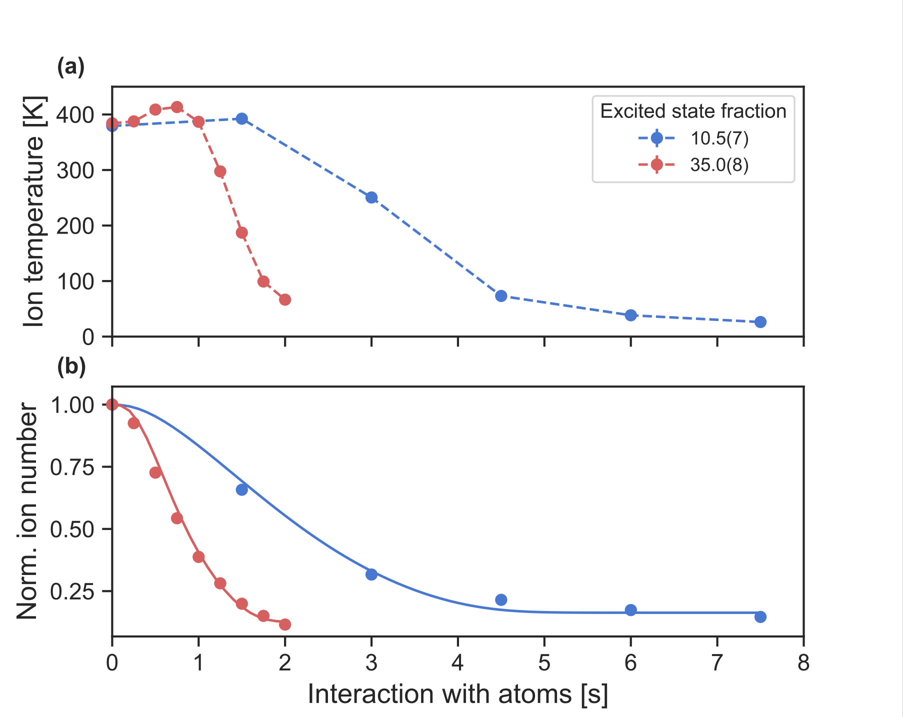

Figure 4.6: Anion-atom interactions in a hybrid atom-ion trap. (a) The ion temperature as a function of interaction time with the atom cloud is shown for two different excited state fractions of rubidium. The points are the experimentally measured data and the colored dashed lines are the guide to the eye. (b) The normalized ion numbers are plotted as a function of interaction time with the atom cloud for two different excited state fractions. The points are the experimentally measured data, fitted with Equation 4.1 represented with colored solid lines. The errors on the measured data points are Gaussian-propagated statistical errors and are smaller than the circular markers.

Nevertheless, the shrinking of the width of ions' time of flight distribution, seen in Figure 4.5, is a clear indicator of the $OH^-(H_2O)$ sympathetic cooling via collisions with an ultracold buffer gas. Using the thermometry technique established in our work [1], we obtain a linear mapping between the variance of ions' time of flight to the detector and the temperature of ions in the trap. This enables us to plot the temperature of the ions as a function of interaction time with the atoms for two different excited state fractions in Figure 4.6 (a). In both cases, we observe a decrease in the ions' temperature. For a higher excited state fraction, the ions cool down from 384(6) K to 67(3) K in two seconds, whereas for a lower excited state fraction, the final ion temperature attained in just under eight seconds is 26(3) K. This difference in the lowest temperature reached is due to the presence of additional loss channels present in the former case, which result in the loss of ions from the trap before they could be sufficiently cooled further via elastic collisions.

In our system, the direct associative electronic detachment between Rb and $OH^-(H_2O)$ leading to the production of $RbOH(H_2O)$ is unlikely as the autodetachment region is only accessible for collision energies much higher than that encountered in our system [165]. The dominant reaction channel in the Rb-$OH^-(H_2O)$ system is via indirect detachment where a vibrationally hot $RbOH^-$ is formed as an intermediate product which, depending on the energy distribution considerations, would be the final stable product for this reaction or alternatively results in the formation of the products $RbOH+H_2O+e^-$ due to rovibrationally induced electronic detachment [212]. However, in our current setup, we cannot distinguish the final products of a reaction process but can only observe the ion losses that are attributed to the sum of the possible reactive channels.

To estimate the reaction rate coefficient for these loss channels between Rb and $OH^-(H_2O)$ anions, the change in the number of ions as a function of interaction time with the atoms is determined and is shown in Figure 4.6 (b). The solid points are the experimentally measured data for two different excited state fractions. The solid lines represent the evolution of the ion numbers described as:

$$N_{\mathrm{I}}(t) = (1 - N_{\mathrm{off}}) \cdot \exp\left(-\kappa \int_0^t \Phi_{\mathrm{AI}}(t')dt'\right) \cdot \exp(-k_{\mathrm{bgd}} t) + N_{\mathrm{off}} \tag{4.1}$$

where N_{off} is the number of ions as $t \to \infty$, κ is the reaction rate coefficient, $\Phi_{AI}(t)$ is the time-dependent atom-ion overlap and k_{bgd} is the ions' background loss rate without the presence of atoms in the trap. As the ion density is directly proportional to the temperature of the ions, the latter is determined via the ions' time of flight distributions and then interpolated to determine the time-dependent ion density and thus, the ion-atom overlap via Equation 2.12. The offset seen in these measurements could possibly arise from the presence of other ion species. Despite tuning the trap loading parameters to minimize the loading of other anionic species into the trap, there could be still some ions from a mass different than $OH^-(H_2O)$ that were loaded into the trap. Though the number of these ions is relatively low to create a significant change in the ions' TOF distribution, they are still enough to result in an offset while observing the time-evolution of the ion numbers. This offset was also observed during the photodetachment tomography measurements with a photodetachment laser beam at $\lambda = 405\,\text{nm}$ ($E_\gamma = 3.06\,\text{eV}$) and was further accounted for while determining the ions' spatial density distributions. Since the photon energy is larger than the photodetachment threshold of the $OH^-(H_2O)$ anion, the ions that remain even after a long interaction time with the laser beam are assumed to be the other ionic species, which could not be separated from the $OH^-(H_2O)$ anion ensemble.

With these considerations, the preliminary reaction rate coefficient for the excited state fraction of 10.5(7)% is determined as $\kappa = 1.42(4) \cdot 10^{-9}\,\text{cm}^3\text{s}^{-1}$, which is marginally higher than that observed for Rb-OH^-. Taking into account the systematic errors, arising from the ion offset, uncertainty in the determination of the atom-ion overlap mainly due to ambiguities in saturation absorption imaging of the atom cloud and approximation of the ions' radial density distribution under the r^6 potential, it can be said that the reactive loss rates for the system Rb-$OH^-(H_2O)$ are on the same order of magnitude as the Rb-OH^-. However, while there was no appreciable anion sympathetic cooling observed for the case of the Rb-OH^- system, we observed a significant cooling for the Rb-$OH^-(H_2O)$ system due to a more favorable mass ratio of the latter. In order to achieve a quantitative understanding of the dynamics involved, systematic experimental investigations on determining the ground state and excited state reaction rate coefficients for the Rb-$OH^-(H_2O)$ system, with the possibility to distinguish different reactive channels, would be required. These measurements would reveal critical insights into both the reaction dynamics as well as the prospects of cooling the ions to even lower temperatures. Additionally, investigations on anion-neutral systems with $OH^-(H_2O)_l$ where $l > 1$ would also reveal interesting insights into the effect of hydration on the collisional dynamics in such systems where the influence of steric effects becomes more pronounced.

CHAPTER 5

DYNAMICS OF ATOMIC ANIONS WITH ATOMS

In this chapter, we investigate the dynamics of collisions between O^- atomic anions and rubidium atoms in a hybrid atom-ion trap. Firstly, a brief introduction to the state-dependent studies in the field of hybrid systems is motivated followed by the description of our published work on electronic quantum state-dependent anion-neutral interactions. Subsequently, with the insights from our published work, we discuss the implications of our results on the sympathetic cooling of these atomic anions via laser-cooled ultracold rubidium.

5.1 Hybrid systems for state-dependent studies

Over the last years, rapid technological advances have facilitated the co-trapping of ions and atoms combining the principles of radio-frequency traps and magneto-optical or optical dipole traps respectively, into a single hybrid atom-ion trapping system [54]. Using the distinct features of both its subsystems, such hybrid traps provide a platform to not only pursue fundamental research on ion-neutral collisions dynamics but also open up new frontiers in the field of quantum technologies [63, 64, 213, 214].

The control and range for tunability of interactions render these hybrid systems ideal tools to study cold and controlled ion-neutral collisions with energies ranging from room temperature down to less than 1 K [68, 215, 216, 217]. From investigating the influence of spin- or charge-exchange processes to the effect of electronically excited systems, these results enable an insight into quantum state-dependent collisions and the investigation of chemical phenomena in their most elementary level [66, 75, 76, 191, 218, 219].

While cations are extensively studied in hybrid atom-ion traps, the experimental studies of ion-atom interactions involving anions in such systems are rather limited. In our previous work detailed in Chapter 4, we expanded the understanding of associative electronic detachment dynamics in a hybrid system where rubidium atoms and hydroxide anions are co-trapped in one single setup. In addition to different dynamics at work for distinct electronic states of the neutral, we also identified the AED reaction as a major loss channel rendering the sympathetic cooling of OH^- molecular anion rather inefficient. Improving the mass ratio of the system by changing the anionic species, and investigating the Rb-$OH^-(H_2O)$ system, we were able to qualitatively demonstrate the sympathetic cooling of molecular anions with an ultracold buffer gas. Since, the reactive processes were the main ion loss channels in the above systems, to observe an efficient anion sympathetic cooling we pursued to identify a system where the detachment loss processes are suppressed. [220].

Theoretical investigations suggest that the molecular complex Rb-O^- has several electronic excited states that are stable against autodetachment (their corresponding anionic potential energy curves lie below the neutral one). Hence, from the ground state entrance channel Rb ($S_{1/2}$) + O^-, all the possible paths avoid the autodetachment region. Since the non-adiabatic induced detachment can be ruled out, due to compact valence-bound orbitals and the large mass of the systems, the associative electronic detachment rates should be very small. This is in agreement with the trend observed for other alkali monoxide systems where all the four relevant electronic ground states were found to be stable against autodetachment [221, 222]. In addition to OH^- anions, atomic O^- anions are also trapped in our system in large quantities, enabling us to experimentally investigate the electronic quantum state-dependent detachment processes in Rb-O^-. These results are discussed in the following section.

5.2 Quantum state-dependent detachment processes

We present an experimental investigation on the quantum state-dependent anion-neutral detachment processes. Different processes leading to the loss of anion's excess electron are identified for both ground state and excited state rubidium. The rate coefficient for these detachment loss processes is estimated as a function of the excited state fraction of rubidium. Since the only energetically feasible channel for the ground state is the associative electronic detachment reaction, the experimental findings are supported via potential energy surfaces describing the AED reaction between O^- anion and rubidium atom in its ground state.

My contributions were in the stabilization and optimization of the experimental setup for data acquisition, where I performed all the experimental measurements used in this work. With the techniques established from the previous work,

I analyzed the data acquired and quantified the detachment loss rates between rubidium atoms and O^- anions co-trapped in a hybrid atom ion trap. I also prepared the final figures and the manuscript, except for the theoretical parts which were written together with Dr. Milaim Kas. (affl. Deutsches Elektronen-Synchrotron (DESY), Germany). Reproduced from [3], with the Permission of AIP Publishing.
Title: **Quantum state-dependent anion-neutral detachment processes**
Authors: **Saba Zia Hassan**, Jonas Tauch, Milaim Kas, Markus Nötzold, Roland Wester, and Matthias Weidemüller.
Published in: J. Chem. Phys. **156**, 094304 (2022).

The Journal of Chemical Physics

Quantum state-dependent anion–neutral detachment processes

Cite as: J. Chem. Phys. **156**, 094304 (2022); https://doi.org/10.1063/5.0082734
Submitted: 17 December 2021 • Accepted: 08 February 2022 • Accepted Manuscript Online: 08 February 2022 • Published Online: 01 March 2022

Saba Zia Hassan, Jonas Tauch, Milaim Kas, et al.

View Online Export Citation CrossMark

ARTICLES YOU MAY BE INTERESTED IN

The dynamics of CO production from the photolysis of acetone across the whole $S_1 \leftarrow S_0$ absorption spectrum: Roaming and triple fragmentation pathways
The Journal of Chemical Physics **156**, 094303 (2022); https://doi.org/10.1063/5.0080904

Optimal control of photodissociation of phenol using genetic algorithm
The Journal of Chemical Physics **156**, 094305 (2022); https://doi.org/10.1063/5.0081282

Do not forget the Rydberg orbitals
The Journal of Chemical Physics **156**, 100901 (2022); https://doi.org/10.1063/5.0084574

Webinar
Interfaces: how they make or break a nanodevice
March 29th – Register now
Zurich Instruments

AIP Publishing

J. Chem. Phys. **156**, 094304 (2022); https://doi.org/10.1063/5.0082734

© 2022 Author(s).

The Journal of Chemical Physics ARTICLE scitation.org/journal/jcp

Quantum state-dependent anion–neutral detachment processes

Cite as: J. Chem. Phys. **156**, 094304 (2022); doi: 10.1063/5.0082734
Submitted: 17 December 2021 • Accepted: 8 February 2022 •
Published Online: 1 March 2022

Saba Zia Hassan,[1,a)] Jonas Tauch,[1] Milaim Kas,[2,3] Markus Nötzold,[4] Roland Wester,[4,b)] and Matthias Weidemüller[1,c)]

AFFILIATIONS

[1] Physikalisches Institut, Ruprecht-Karls-Universität Heidelberg, 69120 Heidelberg, Germany
[2] Deutsches Elektronen-Synchrotron (DESY), 22607 Hamburg, Germany
[3] Department of Mathematics, Universität Hamburg, 20146 Hamburg, Germany
[4] Institut für Ionenphysik und Angewandte Physik, Universität Innsbruck, 6020 Innsbruck, Austria

[a)] Author to whom correspondence should be addressed: hassan@physi.uni-heidelberg.de
[b)] Electronic mail: roland.wester@uibk.ac.at
[c)] Electronic mail: weidemueller@uni-heidelberg.de

ABSTRACT

The detachment loss dynamics between rubidium atoms (Rb) and oxygen anions (O^-) are studied in a hybrid atom–ion trap. The amount of excited rubidium present in the atomic ensemble is actively controlled, providing a tool to tune the electronic quantum state of the system and, thus, the anion–neutral interaction dynamics. For a ground state Rb interacting with O^-, the detachment induced loss rate is consistent with zero, while the excited state Rb yields a significantly higher loss rate. The results are interpreted via *ab initio* potential energy curves and compared to the previously studied Rb–OH^- system, where an associative electronic detachment reactive loss process hinders the sympathetic cooling of the anion. This implies that with the loss channels closed for ground-state Rb and O^- anion, this system provides a platform to observe sympathetic cooling of an anion with an ultracold heavy buffer gas.

Published under an exclusive license by AIP Publishing. https://doi.org/10.1063/5.0082734

I. INTRODUCTION

Anion–neutral reactions play a key role in diverse fields ranging from organic chemistry studying S_N2 reactions[1–3] to Earth's atmosphere[4–6] and the interstellar medium.[7,8] Over the last years, many techniques were developed to study anion–neutral chemistry, including flow and drift tubes,[9–11] crossed beam apparatus,[12–14] guided ion beams,[15–17] and ion traps.[18–20]

Recent developments in the field of hybrid atom–ion traps have further facilitated the study of cold and controlled ion–neutral reactions.[21] These works demonstrate the influence of the nuclear spin configuration[22,23] or the valence orbital on reaction rates, as well as deviations from classical capture models at low collision energies.[24,25] With a large amount of control and tunability, these hybrid traps provide a platform for investigating the dynamics of ion–neutral systems.

A class of ion–neutral interactions unique to anionic systems are electronic detachment processes. Due to the small binding energy of the electron, these detachment processes are frequently observed and can occur via different channels.[26–28] One of the most extensively studied processes is the associative electronic detachment (AED) reaction.[28–30] Here, the excess electron is detached from the reaction complex to stabilize the formation of a neutral molecule. This class of reactions is one of the main destruction mechanisms of anions in the interstellar medium and plays a relevant role as an intermediate step in the creation of other molecules.[7,31–33]

The system Rb–OH^- has been of particular interest for theoretical and experimental studies while investigating AED reactions.[29,30,34,35] A recent comprehensive study on this system[36] investigates the dynamics of electronic quantum-state dependent AED reaction, where the reaction proceeds via a dipole-bound intermediate complex. In the case of an excited state rubidium, an unstable intermediate is formed, but for a ground state rubidium, this complex is stable. The probability that the reaction takes place is determined by the crossing between the anionic and neutral potential energy curves (PECs). The important implications of these results were to identify the effective core potentials (ECPs) suitable to investigate such anion–neutral collisional dynamics and also to quantify AED reaction as the main loss channel in the Rb–OH^- system. The latter is of key consequence in determining the feasibility of sympathetic cooling of the anion via collisions with the ultracold buffer gas of laser-cooled rubidium atoms. Sympathetic cooling of atomic and molecular ions to ultracold temperatures via a neutral buffer gas has paved way for multiple areas of research particularly in cation–atom systems[21] but is not as extensively investigated in anion–atom systems. In the Rb–OH^- system, there is a finite probability, even for Rb in its ground state to undergo AED with OH^-, making the cooling of the molecular anion rather inefficient. It can be inferred that limiting the loss from both the ground and excited state channels is crucial to observing sympathetic cooling.[37]

In order to study a system where the detachment loss channels are potentially suppressed, we extend our work to investigate the electronic quantum state-dependent detachment reactions between Rb atoms and O^-. With a mass ratio quite similar to Rb–OH^-, the cooling dynamics in this system will also be primarily influenced by the presence of reactive processes. Based on the electron affinity of Rb (0.49 eV[38]) and O (1.46 eV[39]), the only energetically possible channel for ground state rubidium interacting with O^- is the AED process where $Rb + O^- \rightarrow RbO + e^-$.

Analogous to the Rb–OH^- case, in addition to AED, several channels open for the reaction of O^- with excited state Rb, which has an energy of ~1.6 eV higher than Rb in its ground state. As a result, the following loss channels are also energetically accessible:

- Penning detachment (PD),
$$Rb^* + O^- \rightarrow Rb + O + e^-.$$
- Charge transfer (CT),
$$Rb^* + O^- \rightarrow Rb^{*-} + O.$$
- Electronic to kinetic energy transfer (leading to loss of the ion from the trap),
$$Rb^* + O^- \rightarrow Rb + O^- + E_{\mathrm{kin}}.$$

Here, the loss channels PD and CT are exo-energetic, corresponding to an energy difference of $\Delta E \approx -0.14$ eV and $\Delta E \approx -0.63$ eV, respectively. For Rb–OH^- system, these channels were shown to be negligible in comparison to AED. However, these results cannot be straightforwardly extrapolated to the Rb–O^- system. In particular, the Penning detachment reaction channel, closed in the Rb–OH^- case, is an additional loss channel that will compete with AED and is likely to be comparable with the latter.[26] Together, all these channels contribute to the ion losses from the trap.

In this work, we experimentally investigate the electronic quantum state-dependent detachment processes between Rb atoms and O^- anions in a hybrid atom–ion trap, where the fraction of electronically excited rubidium in the atom ensemble is precisely controlled. The atom-induced ion losses are measured as a function of this excited state fraction, which yields a loss rate coefficient for ground state and excited state rubidium interacting with O^-. The possible loss channels are discussed, and the measured experimental results are interpreted via *ab initio* potential energy surfaces describing the most relevant AED process. Finally, the implications of these results on the sympathetic cooling of O^- ions in such hybrid atom–ion traps are discussed.

II. EXPERIMENT

The experimental setup uses a hybrid atom–ion trap as shown in Fig. 1(a). The ions are produced in a plasma discharged source, from a mixture of argon gas and water vapor. The time of flight of ions depends on the mass to charge ratio and is separated in the time domain as they traverse through the Wiley–Mclaren spectrometer. The ions are then mass-selected to only load the O^- ions into the octupole radio-frequency wire-trap. The multipole trap configuration provides a nearly field-free region, which decreases ion heating caused by collisions in the radio-frequency field. The use of wires in place of the conventionally used thicker cylindrical rods provides the optical access needed for cooling or diagnostic laser beams. In order to ensure stable trapping of O^- ions, a peak-to-peak radio-frequency voltage of 340 V is chosen at an angular frequency of $\omega = 2\pi \cdot 6.8$ MHz. The trapped ions are then thermalized for 200 ms with a pulse of the helium buffer gas at room temperature. The length of the buffer gas is chosen such that ions exhibit a thermal behavior in their time-of-flight distribution. The temperature of the ions is determined by mapping their temperature to their time of flight during extraction from the trap. The temperature of the ion cloud, after interaction with the helium buffer gas, is estimated to be 370(12) K. Since the time-of-flight distribution is well-described by a Gaussian distribution with no high-energy tails, we conclude that the energy distribution of the trapped ions is thermal. A more detailed description of the setup including an explanation of the used thermometry method can be found in Ref. 40. The same method is also used to measure the ion temperature after interaction with the rubidium atoms. The spatial distribution of the ions is determined via photodetachment tomography via a far-threshold laser beam.[41] In the axial direction, the ions exhibit a Gaussian distribution due to the harmonic trapping potential in this direction. Radially, the spatial distribution of ions is governed by the r^6 radial potential of an octupole trap.

Once the ions are loaded in the trap and thermalized with the helium buffer gas pulse, a laser-cooled cloud of ultracold ^{85}Rb atoms is created at the center of the ion cloud. The energy level scheme is shown in Fig. 1(b). The atoms are loaded from a 2D magneto-optical trap into a dark spontaneous-force trap (darkSPOT). In this configuration, the intensity of the repumper laser beam is suppressed, thus reducing the number of atoms pumped into the cooling cycle and increasing the number of atoms in the ground state F = 2. Therefore, by tuning the intensity of the repumper laser beam, the number of atoms pumped into the cooling cycle can be controlled. This is quantified as the excited state fraction, defined as the ratio of number of atoms in the excited state ($F' = 4 + F' = 3$) to the total number of atoms ($F' = 4 + F' = 3 + F = 3 + F = 2$). The former is determined via fluorescence imaging and the latter is determined via saturation absorption imaging.[42] The control on the amount of excited rubidium provides a tool to investigate the electronic state-dependent reaction dynamics of this system.

Published under an exclusive license by AIP Publishing

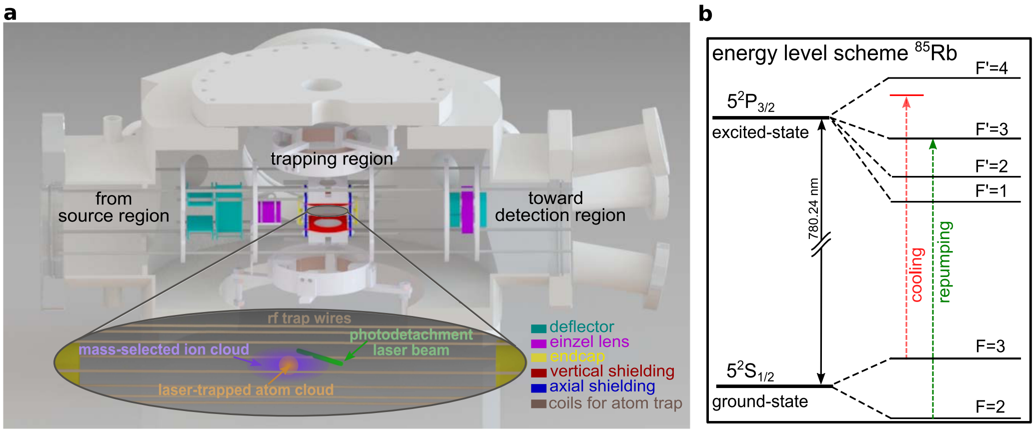

FIG. 1. (a) Hybrid atom–ion trap setup. The ions are produced in the source chamber and loaded into the radio-frequency ion trap. The trap electrodes are shown in different colors. The spatial distribution of the trapped ion cloud (purple cloud) is performed via photodetachment tomography with a far-threshold laser beam (shown in green). The ions are concentrically overlapped with a laser-cooled ^{85}Rb atom cloud (orange). After interaction with the atoms, the ions are guided toward the detector and their temperature is extracted from their time of flight to the detector. (b) Energy level scheme for ^{85}Rb. The cooling and repumper transitions are shown in red and green, respectively. In the darkSPOT configuration, the population of the state F = 2 is increased by spatially reducing the intensity of the repumper laser beam. This provides a tool to control the electronic state configuration of the atomic ensemble, by changing the amount of rubidium present in the excited state $5^2P_{3/2}$ or the ground state $5^2S_{1/2}$.

III. DETERMINATION OF RATE COEFFICIENTS

Once the loading of the atoms in the trap (at the center of the ion cloud) starts, the atoms and ions undergo elastic and reactive collisions. The elastic collisions transfer kinetic energy from the hotter species, resulting in the sympathetic cooling of the ions. In this case, O^- anions are cooled sympathetically via elastic collisions with ultracold rubidium. The reactive collisions result in the loss of the anions due to the formation of rubidium monoxide. The ion number and their time-of-flight distribution are recorded for different interaction times with the atom cloud. The time $t = 0$ represents the start of the loading of the atoms in the trap.

The overlap $\Phi(t)$ between the two clouds depends on their density distribution and is defined as

$$\Phi(t) = \int_0^t \rho_{\mathrm{ion}}(x,y,z,T(t))\rho_{\mathrm{atom}}(x,y,z,t)dxdydz. \tag{1}$$

Here, ρ_{atom} and ρ_{ion} are the time-dependent density distributions of the atom and ion cloud, respectively. The time-dependence of the atom cloud distribution is described as

$$\rho_{\mathrm{atom}}(t) = \rho_{\mathrm{atom},0}(1 - \exp(-t \cdot L)), \tag{2}$$

where $\rho_{\mathrm{atom},0}$, the peak atom density, and L, the loading rate, are the fit parameters obtained by fitting the measured data to Eq. (2). The measured loading of the atom cloud and its corresponding fit and fit parameters are shown in Fig. 2(a). The atom density distribution is experimentally determined via saturation absorption imaging. The initial density distribution of ions (at $t = 0$) is determined via photodetachment tomography. This density distribution is dynamically altered due to elastic collisions with the atoms. As the ion temperature changes, the spatial distribution of ions also evolves accordingly. The ion temperature after interaction with the atom cloud is shown in Fig. 2(b) (purple points). The interpolation of the ion temperature as a function of the interaction time is calculated (purple curve), representing the time-evolution of the density distribution of ions. After the time-dependent density distributions of the atom and ion cloud are estimated, the overlap is calculated via Eq. (1), and the evolution of the ion number $N_{\mathrm{i}}(t)$ is described as

$$N_{\mathrm{i}}(t) = N_0 \cdot \exp\left(-k\int_0^t \Phi(t')dt'\right)\exp(-k_{\mathrm{pd}}t). \tag{3}$$

Here, N_0 is the initial number of ions at $t = 0$, k is the reactive rate coefficient, and k_{pd} is the background photodetachment loss. The photodetachment threshold of O^- (≈1.46 eV) is lower than that of the cooling light needed for cooling ^{85}Rb (≈1.6 eV). The ion loss rate due to the photodetachment of the anion is determined via an independent measurement (blue points in Fig. 2(c)], where the atoms are not loaded into the trap but the cooling (and repumping) laser beams are switched on. An exponential fit to the ion number recorded after the interaction time with these laser beams yields the photodetachment rate k_{pd} [blue curve in Fig. 2(c)]. With all these parameters pre-determined, the measured ion losses due to the varying interaction time with the atoms [red points in Fig. 2(c)] are fitted with Eq. (3) [red curve in Fig. 2(c)], yielding the reaction rate coefficient k for a given excited state fraction.

As previously mentioned, by tuning the intensity of the repumper laser beam, it is possible to vary the amount of excited rubidium in the atomic ensemble, i.e., the excited state fraction. The reaction rate coefficient, k, is determined for various excited state fractions, and the observed dependency is plotted in Fig. 3. From a linear fit (green line) through the experimentally measured data (black points), the reaction rate coefficient in the case of an excited state rubidium interacting with O^- anion is measured as $k_{\mathrm{es}} = (1.8 \pm 0.1) \cdot 10^{-9}$ cm^3 s^{-1}. In the case of a system with ground state

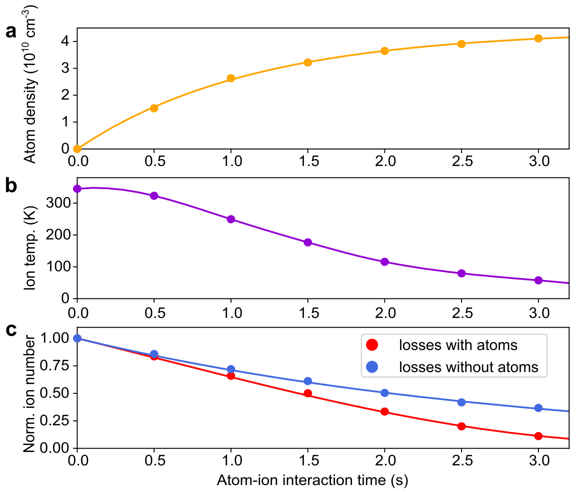

FIG. 2. Temporal evolution of atom density, ion temperature, and normalized ion number are shown. The statistical errors of the measured data (points) are smaller than their point size. (a) The measured time-evolution of the atom density is shown (orange points). This is fitted with the function in Eq. (2) yielding the atom cloud loading rate, $L = 0.87(3)$ s^{-1}, and the peak atom density, $\rho_{\text{atom},0} = 4.42(5) \cdot 10^{10}$ cm^{-3} (orange curve). (b) The measured time-evolution of the ion temperature due to interaction with an ultracold buffer gas is shown (purple points). The interpolation function for the ion temperature as a function of the interaction time (purple curve) provides the corresponding change in the density distribution of ions. (c) The measured normalized ion losses as a function of the atom–ion interaction time. Here, the background loss rate, $k_{\text{pd}} = 0.339(6)$ s^{-1}, is determined without the presence of atoms (blue points), fitted with an exponential decay function (blue curve). For an exemplary excited state fraction of 0.113(5), the ion losses with the atoms (red points) fitted with Eq. (3) (red curve) yield the reaction rate coefficient $k = 1.95(4) \cdot 10^{-10}$ cm^3 s^{-1}. The uncertainty due to systematic errors is estimated to be ~40%.

rubidium, the extrapolation of the fit to zero (fit intercept) yields the reaction rate coefficient as $k_{\text{gs}} = (-0.8 \pm 3.1) \cdot 10^{-11}$ cm^3 s^{-1}. The systematic errors are estimated at ~40% and attributed to the errors in the characterization of the atom cloud diagnostics via fluorescence imaging and saturation absorption imaging.

IV. INTERPRETATION

Experimental results show that the loss rate coefficient for the ground state Rb interacting with O$^-$ is consistent with zero. As discussed earlier, the AED channel is the only energetically possible loss channel in the Rb–O$^-$ system, where Rb is in the ground state. AED reactions occur if the potential energy curves for the anionic and neutral systems cross, thus enabling a transition between the two systems. If such crossings are not energetically accessible, the detachment can only be triggered through non-adiabatic couplings,[43] for which the rate of electron detachment is several orders of magnitude smaller than for the former mechanism.[44]

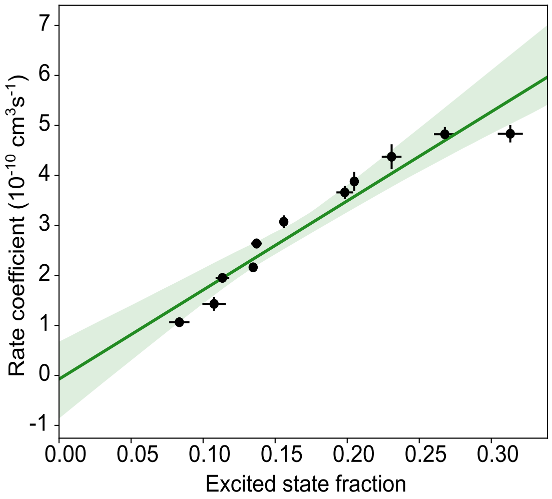

FIG. 3. Electronic state-dependent reaction dynamics. The reaction rate coefficients for different electronic configurations of the atomic ensemble are plotted as a function of the corresponding excited state fractions of the atom cloud. The experimentally measured data (black points) is fitted with a linear function (green line). The error bars of the data points represent the Gaussian propagated statistical errors. The slope (intercept) of the linear fit yields the reaction rate coefficient of O$^-$ interacting with excited (ground) state rubidium. The green shaded region shows the 95% confidence bands of the true fit.

In order to confirm if such crossings are present along the ground state reaction path, the potential energy curves (PECs) that correlate with the entrance channel Rb(^{2}S) + O$^-$ have been calculated using *ab initio* methods. All calculations have been performed with the MOLPRO program.[45] The Davidson corrected multi-reference configuration interaction with single and double (MRCISD + Q) method[46] is applied to a set of state-averaged molecular orbitals obtained using the complete active space self-consistent approach (CASSCF). The active space includes 6 σ and 2 π orbitals, corresponding to valence orbitals and inner-valence shells of the Rb atom (4*s* and 4*p* orbitals). The multiconfiguration Dirac-Fock (MDF) electron core potential and the corresponding *spdf* segmented valence basis set,[47] augmented by a set of 3s, 2p, and 1d even-tempered diffuse functions, have been used to describe the 28 core electrons and the 9 outer electrons of Rb, respectively. The oxygen atom has been described by the quadruple zeta augmented valence correlation-consistent Dunning basis sets[48] (AVQZ). The calculated PECs are depicted in Fig. 4. The main panel shows the four molecular RbO$^-$ states that correlate with the ground state entrance channel Rb(^{2}S) + O$^-$: $^1\Sigma^+$, $^3\Sigma^+$, $^1\Pi$, and $^3\Pi$. Their energy ordering follows the trend seen in other alkali oxides.[49,50] All anionic states are valence bound states that are all stable against autodetachment, i.e., their respective detachment energies (energy gap between anion and neutral PECs at their respective minimum) are positive. This is predicted to be about 1.2 eV, as compared to about 0.3 eV for the case of Rb–OH$^-$,[30] and the AED reaction is predicted to be exo-energetic ($\Delta E \approx -1.1$ eV). In addition, no crossing between anion and neutral PECs can be seen along the reaction path. Due to the large reduced mass and rather large detachment energies, the non-adiabatic detachment rate is expected to be orders of magnitude smaller than the Langevin rate of $4.4 \cdot 10^{-9}$ cm^3 s^{-1}.[51] This is in

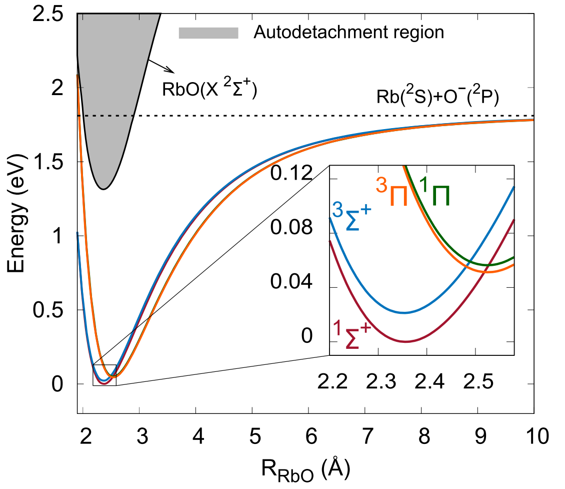

FIG. 4. The main panel shows the potential energy curves (PECs) describing the four molecular states that correlate with the Rb (^{2}S) + O$^-$ ground state channel (colored lines) and the neutral ground state RbO (black line). The smaller inset shows the anion PECs around the potential well. The dashed line corresponds to the energy at the ground state entrance channel.

agreement with the previously determined negligible rate coefficient for the ground state.

The collisions of O$^-$ with excited Rb lead to losses with a measured rate coefficient of $k_{es} = (1.8 \pm 0.1) \cdot 10^{-9}$ cm^3 s^{-1}. Even considering the systematic error of 40%, this value is significantly lower than the Langevin rate of $7.4 \cdot 10^{-9}$ cm^3 s^{-1}. Such a discrepancy was also observed in the previous work investigating the Rb–OH$^-$ case.[36] These results indicate the presence of other processes in the system, which suppress the coupling into the autodetachment manifold. The reduced loss rate from the excited channel could be explained by the presence of higher-lying excited states that are stable against autodetachment, thus providing reaction paths that avoid the loss channels. In addition, some dynamical stabilization processes may occur, leading to non-unity detachment probability when the autodetachment region is reached. This could result in an overall reduced loss rate. A thorough theoretical investigation of the stability of the higher-lying excited states against autodetachment is needed to quantitatively explain the observed deviation for the excited state.

V. CONCLUSION

We have measured electronic quantum state-dependent loss rates in a hybrid ion–atom trap involving ultracold Rb atoms and trapped O$^-$ anions. The energetically allowed electron detachment processes are identified as associative electronic detachment (AED) for the ground state Rb(^{2}S) + O$^-$ channel and AED, charge-transfer, and Penning detachment for the excited state Rb(^{2}P) + O$^-$ channel. A detailed theoretical description of the structure, dynamics, and stability of the excited state of the Rb–O$^-$ system and an experimental framework to distinguish these different loss channels is required. In this work, we observed a vanishingly small loss rate for the reaction with Rb in its ground state. The potential energy curves are calculated using *ab initio* methods. The AED channel is predicted to be exo-energetic. However, all anionic states are found to be stable against autodetachment, and no crossings into the autodetachment region are seen, supporting the experimentally observed vanishing rate coefficient. For reactions involving excited Rb, a rate significantly lower than the Langevin rate is observed, indicating the presence of dynamical stabilization processes. This discrepancy is similar to the one observed in the Rb–OH$^-$ case.

From the results obtained for the ground state rate coefficient, it can be inferred that it is possible to minimize the O$^-$ ion losses by confining rubidium atoms only in their ground state, for example, in a dipole trap. Additionally, a far-detuned dipole trap would also suppress photodetachment losses, which would result in a higher number of elastic collisions, resulting in a more efficient sympathetic cooling of the ions.

Besides the atom-to-ion mass ratio, the key properties that govern the dynamics of ion sympathetic cooling in the trap are the ion–ion thermalization rate, the atom–ion elastic collision rate, and the atom–ion reactive collision rate. The ratio of atom–ion elastic to reactive collision rate is critical in determining the cooling efficiency.[52,53] Considering the measured loss rate, this elastic to reactive collision ratio is estimated to be an order of magnitude larger in the Rb–O$^-$ system as opposed to the Rb–OH$^-$ system,[36] making it feasible to observe anion sympathetic cooling in this system. The first signatures of anion sympathetic cooling are already seen in this work [see Fig. 2(b)] and will be further investigated in the future.

ACKNOWLEDGMENTS

We acknowledge the support from the Austrian Science Fund (FWF) under Project No. I3159-N36 and Deutsche Forschungsgemeinschaft (DFG) under Project No. WE/2661/14-1. S.Z.H. acknowledges the support from the HGSFP fellowship. M.K. is grateful to the BMBF project MeSoX (Project No. 05K19GUE) for financial support.

AUTHOR DECLARATIONS

Conflict of Interest

The authors have no conflicts to disclose.

DATA AVAILABILITY

The data that support the findings of this study are available from the corresponding author upon reasonable request.

REFERENCES

[1] M. L. Chabinyc, S. L. Craig, C. K. Regan, and J. I. Brauman, "Gas-phase ionic reactions: Dynamics and mechanism of nucleophilic displacements," Science **279**, 1882–1886 (1998).

[2] S. Schmatz, "Quantum dynamics of gas-phase S$_N$2 reactions," ChemPhysChem **5**, 600–617 (2004).

[3] J. Mikosch, S. Trippel, C. Eichhorn, R. Otto, U. Lourderaj, J. X. Zhang, W. L. Hase, M. Weidemüller, and R. Wester, "Imaging nucleophilic substitution dynamics," Science **319**, 183–186 (2008).

Published under an exclusive license by AIP Publishing

[4] S. G. Ard, J. J. Melko, B. Jiang, Y. Li, N. S. Shuman, H. Guo, and A. A. Viggiano, "Temperature dependences for the reactions of $O_2{}^-$ and O^- with N and O atoms in a selected-ion flow tube instrument," J. Chem. Phys. **139**, 144302 (2013).

[5] N. S. Shuman, D. E. Hunton, and A. A. Viggiano, "Ambient and modified atmospheric ion chemistry: From top to bottom," Chem. Rev. **115**, 4542–4570 (2015).

[6] M. S. Ugelow, J. L. Berry, E. C. Browne, and M. A. Tolbert, "The impact of molecular oxygen on anion composition in a hazy archean earth atmosphere," Astrobiology **20**, 658–669 (2020).

[7] T. J. Millar, C. Walsh, and T. A. Field, "Negative ions in space," Chem. Rev. **117**, 1765–1795 (2017).

[8] E. Yurtsever, M. Satta, R. Wester, and F. A. Gianturco, "On the formation of interstellar CH^- anions: Exploring mechanism and rates for CH_2 reacting with H^-," J. Phys. Chem. A **124**, 5098–5108 (2020).

[9] C. H. DePuy, J. J. Grabowski, and V. M. Bierbaum, "Chemical reactions of anions in the gas phase," Science **218**, 955–960 (1982).

[10] A. A. Viggiano, R. A. Morris, J. S. Paschkewitz, and J. F. Paulson, "Kinetics of the gas-phase reactions of Cl^- with CH_3Br and CD_3Br: Experimental evidence for nonstatistical behavior?," J. Am. Chem. Soc. **114**, 10477–10482 (1992).

[11] V. M. Bierbaum, "Go with the flow: Fifty years of innovation and ion chemistry using the flowing afterglow," Int. J. Mass Spectrom. **377**, 456–466 (2015).

[12] R. L. Champion, L. D. Doverspike, M. S. Huq, D. Scott, and Y. Wang, "Reactive scattering and electron detachment for collisions of halogen negative ions with HCl, DCl, and HBr," J. Chem. Phys. **88**, 5475–5480 (1988).

[13] M. A. Huels, R. L. Champion, L. D. Doverspike, and Y. Wang, "Charge transfer and electron detachment for collisions of H^- and D^- with H," Phys. Rev. A **41**, 4809–4815 (1990).

[14] S. Živanov, M. Čížek, J. Horáček, and M. Allan, "Electron spectra for associative detachment in low-energy collisions of Cl^- and Br^- with H and D," J. Phys. B: At., Mol. Opt. Phys. **36**, 3513–3531 (2003).

[15] E. Haufler, S. Schlemmer, and D. Gerlich, "Absolute integral and differential cross sections for the reactive scattering of $H^- + D_2$ and $D^- + H_2$," J. Phys. Chem. A **101**, 6441–6447 (1997).

[16] K. Rempala and K. M. Ervin, "Collisional activation of the endoergic hydrogen atom transfer reaction $S^-(^2P) + H_2 \rightarrow SH^- + H$," J. Chem. Phys. **112**, 4579–4590 (2000).

[17] L. A. Angel, M. K. Dogbevia, K. M. Rempala, and K. M. Ervin, "Gas-phase hydrogen atom abstraction reactions of S^- with H_2, CH_4, and C_2H_6," J. Chem. Phys. **119**, 8996–9007 (2003).

[18] D. Gerlich, "Ion-neutral collisions in a 22-pole trap at very low energies," Phys. Scr. **1995**, 256–263.

[19] R. Wester, "TUTORIAL: Radiofrequency multipole traps: Tools for spectroscopy and dynamics of cold molecular ions," J. Phys. B: At., Mol. Opt. Phys. **42**, 154001 (2009).

[20] D. Hauser, S. Lee, F. Carelli, S. Spieler, O. Lakhmanskaya, E. S. Endres, S. S. Kumar, F. Gianturco, and R. Wester, "Rotational state-changing cold collisions of hydroxyl ions with helium," Nat. Phys. **11**, 467–470 (2015).

[21] M. Tomza, K. Jachymski, R. Gerritsma, A. Negretti, T. Calarco, Z. Idziaszek, and P. S. Julienne, "Cold hybrid ion-atom systems," Rev. Mod. Phys. **91**, 035001 (2019).

[22] A. Kilaj, H. Gao, D. Rösch, U. Rivero, J. Küpper, and S. Willitsch, "Observation of different reactivities of *para* and *ortho*-water towards trapped diazenylium ions," Nat. Commun. **9**, 2096 (2018).

[23] T. Sikorsky, Z. Meir, R. Ben-Shlomi, N. Akerman, and R. Ozeri, "Spin-controlled atom-ion chemistry," Nat. Commun. **9**, 920 (2018).

[24] F. H. J. Hall and S. Willitsch, "Millikelvin reactive collisions between sympathetically cooled molecular ions and laser-cooled atoms in an ion-atom hybrid trap," Phys. Rev. Lett. **109**, 233202 (2012).

[25] P. Puri, M. Mills, I. Simbotin, J. A. Montgomery, R. Côté, C. Schneider, A. G. Suits, and E. R. Hudson, "Reaction blockading in a reaction between an excited atom and a charged molecule at low collision energy," Nat. Chem. **11**, 615–621 (2019).

[26] R. S. Berry, "Odyssey and oddity: Photo- and collision processes you would not expect," Phys. Chem. Chem. Phys. **7**, 286–290 (2005).

[27] A. Midey, I. Dotan, J. V. Seeley, and A. A. Viggiano, "Reactions of small negative ions with $O_2(a\ ^1\Delta_g)$ and $O_2(X^3\Sigma_g^-)$," Int. J. Mass Spectrom. **280**, 6–11 (2009).

[28] H. Bruhns, H. Kreckel, K. Miller, M. Lestinsky, B. Seredyuk, W. Mitthumsiri, B. L. Schmitt, M. Schnell, X. Urbain, M. L. Rappaport, C. C. Havener, and D. W. Savin, "A novel merged beams apparatus to study anion-neutral reactions," Rev. Sci. Instrum. **81**, 013112 (2010).

[29] J. N. Byrd, H. H. Michels, J. A. Montgomery, and R. Côté, "Associative detachment of rubidium hydroxide," Phys. Rev. A **88**, 032710 (2013).

[30] M. Kas, J. Loreau, J. Liévin, and N. Vaeck, "*Ab initio* study of the neutral and anionic alkali and alkaline earth hydroxides: Electronic structure and prospects for sympathetic cooling of OH^-," J. Chem. Phys. **146**, 194309 (2017).

[31] J. L. Moruzzi, J. W. Ekin, and A. V. Phelps, "Electron production by associative detachment of O^- ions with NO, CO, and H_2," J. Chem. Phys. **48**, 3070–3076 (1968).

[32] H. Kreckel, H. Bruhns, M. Cizek, S. C. Glover, K. A. Miller, X. Urbain, and D. W. Savin, "Experimental results for H_2 formation from H^- and H and implications for first star formation," AIP Conf. Proc. **1642**, 388–391 (2015).

[33] R. Plašil, T. D. Tran, Š. Roučka, P. Jusko, D. Mulin, I. Zymak, S. Rednyk, A. Kovalenko, P. Dohnal, J. Glosík, K. Houfek, J. Táborský, and M. ČíŽek, "Isotopic effects in the interaction of O^- with D_2 and H_2 at low temperatures," Phys. Rev. A **96**, 062703 (2017).

[34] M. Kas, J. Loreau, J. Liévin, and N. Vaeck, "*Ab initio* study of reactive collisions between $Rb(^2S)$ or $Rb(^2P)$ and $OH^-(^1\Sigma^+)$," J. Chem. Phys. **144**, 204306 (2016).

[35] J. Deiglmayr, A. Göritz, T. Best, M. Weidemüller, and R. Wester, "Reactive collisions of trapped anions with ultracold atoms," Phys. Rev. A **86**, 043438 (2012).

[36] S. Z. Hassan, J. Tauch, M. Kas, M. Nötzold, H. López-Carrera, E. S. Endres, R. Wester, and M. Weidemüller, "Associative detachment in anion-atom reactions involving a dipole-bound electron," Nat. Commun. **13**, 818 (2022).

[37] M. Kas, J. Loreau, J. Liévin, and N. Vaeck, "Cold reactive and nonreactive collisions of Li and Rb with C_2^-: Implications for hybrid-trap experiments," Phys. Rev. A **99**, 042702 (2019).

[38] P. Frey, F. Breyer, and H. Holop, "High resolution photodetachment from the rubidium negative ion around the $Rb(5p_{1/2})$ threshold," J. Phys. B: At. Mol. Phys. **11**, L589–L594 (1978).

[39] S. J. Cavanagh, S. T. Gibson, M. N. Gale, C. J. Dedman, E. H. Roberts, and B. R. Lewis, "High-resolution velocity-map-imaging photoelectron spectroscopy of the O^- photodetachment fine-structure transitions," Phys. Rev. A **76**, 052708 (2007).

[40] M. Nötzold, S. Z. Hassan, J. Tauch, E. Endres, R. Wester, and M. Weidemüller, "Thermometry in a multipole ion trap," Appl. Sci. **10**, 5264 (2020).

[41] P. Hlavenka, R. Otto, S. Trippel, J. Mikosch, M. Weidemüller, and R. Wester, "Absolute photodetachment cross section measurements of the O^- and OH^- anion," J. Chem. Phys. **130**, 061105 (2009).

[42] B. Höltkemeier, J. Glässel, H. López-Carrera, and M. Weidemüller, "A dense gas of laser-cooled atoms for hybrid atom-ion trapping," Appl. Phys. B **123**, 51 (2017).

[43] M. Čížek, J. Dvořák, and K. Houfek, "Associative detachment in $Li + H^-$ collisions," Eur. Phys. J. D **72**, 66 (2018).

[44] J. Simons, "Theoretical study of negative molecular ions," Annu. Rev. Phys. Chem. **62**, 107–128 (2011).

[45] H. Werner, P. J. Knowles, G. Knizia, F. R. Manby, M. Schütz, P. Celani, T. Korona, R. Lindh, A. Mitrushenkov, G. Rauhut, K. R. Shamasundar, T. B. Adler, R. D. Amos, A. Bernhardsson, A. Berning, D. L. Cooper, M. J. O. Deegan, A. J. Dobbyn, F. Eckert, E. Goll, C. Hampel, A. Hesselmann, G. Hetzer, T. Hrenar, G. Jansen, C. Köppl, Y. Liu, A. W. Lloyd, R. A. Mata, A. J. May, S. J. McNicholas, W. Meyer, M. E. Mura, A. Nicklass, D. P. O'Neill, P. Palmieri, D. Peng, K. Pflüger, R. Pitzer, M. Reiher, T. Shiozaki, H. Stoll, A. J. Stone, R. Tarroni, T. Thorsteinsson, and M. Wang, MOLPRO, version 2012.1, a package of *ab initio* programs, 2012.

[46] P. J. Knowles and H.-J. Werner, "Internally contracted multiconfiguration-reference configuration interaction calculations for excited states," Theor. Chim. Acta **84**, 95–103 (1992).

[47] I. S. Lim, P. Schwerdtfeger, B. Metz, and H. Stoll, "All-electron and relativistic pseudopotential studies for the group 1 element polarizabilities from K to element 119," J. Chem. Phys. **122**, 104103 (2005).

Published under an exclusive license by AIP Publishing

[48] T. H. Dunning, "Gaussian basis sets for use in correlated molecular calculations. I. The atoms boron through neon and hydrogen," J. Chem. Phys. **90**, 1007 (1989).

[49] B. Mintz, B. Chan, M. B. Sullivan, T. Buesgen, A. P. Scott, S. R. Kass, L. Radom, and A. K. Wilson, "Structures and thermochemistry of the alkali metal monoxide anions, monoxide radicals, and hydroxides," J. Phys. Chem. A **113**, 9501–9510 (2009).

[50] C. W. Bauschlicher, H. Partridge, and L. G. M. Pettersson, "Franck-Condon factors for photodetachment from LiO^-, NaO^-, and KO^-," J. Chem. Phys. **99**, 3654–3658 (1993).

[51] P. Langevin, "A fundamental formula of kinetic theory," Ann. Chim. Phys. **5**, 245–288 (1905).

[52] B. Höltkemeier, P. Weckesser, H. López-Carrera, and M. Weidemüller, "Buffer-gas cooling of a single ion in a multipole radio frequency trap beyond the critical mass ratio," Phys. Rev. Lett. **116**, 233003 (2016).

[53] B. Höltkemeier, P. Weckesser, H. López-Carrera, and M. Weidemüller, "Dynamics of a single trapped ion immersed in a buffer gas," Phys. Rev. A **94**, 062703 (2016).

Published under an exclusive license by AIP Publishing

5.3 Sympathetic cooling of atomic anions

From the investigations into the quantum state-dependent detachment processes between Rb and O^-, we infer that the detachment loss channels for the case of ground-state rubidium are negligible. In this section, we discuss the implications of the above findings in the context of sympathetic cooling of anions via an ultracold buffer gas. Firstly, we demonstrate the cooling dynamics for different relative overlaps between the atom and the ion cloud, followed by a discussion of the different types of collisions that occur in the system. These results were presented in detail in [168], and offer comprehensive complementary insights to the following discussion.

Despite a similar atom-to ion mass ratio as compared to the Rb-OH^- system, the ratio of elastic to reactive collisions in the Rb-O^- system is significantly larger than the former. This makes it feasible to experimentally observe the sympathetic cooling of O^- anions via ultracold buffer gas, Rb.

Once the ions are loaded into the trap, they are thermalized to a temperature of 370(16) K via collisions with a pulse of helium gas at room temperature. This thermal ensemble of ions is then overlapped with an ultracold atom cloud. By moving the atom cloud, along the axial trapping direction, the overlap between the two clouds can be changed. The results for the observed sympathetic cooling of O^- and the corresponding ion losses for two different relative axial positions Δz, of the atom-ion clouds are shown in Figure 5.1 (a). For almost concentric atom-ion clouds, i.e., $\Delta z = -0.3$ mm the ions cool to a final temperature of 30(2) K in three seconds. For $\Delta z = 1.45$ mm, after five seconds of interaction time, the final temperature reached is 90(6) K. The higher temperature is a consequence of the smaller total overlap between ions and atoms, resulting in fewer cooling collisions. Assuming the ion-ion thermalization rate is always much greater than the ion-atom elastic or reactive collision rate, the change in the temperature of the ion ensemble T_I, is described as [168]:

$$\begin{aligned} \dot{T}_\mathrm{I} = \kappa_\mathrm{el} \left\langle \frac{\Delta E}{E} \right\rangle \int_{-\infty}^{\infty} \Bigg\{ \Bigg[\underbrace{\left(\frac{3}{2} k_\mathrm{B} T_\mathrm{A} + \xi V_\mathrm{eff}(x,y) \right)}_{\langle E_\mathrm{A}(r) \rangle} - \left(\frac{7}{3} k_\mathrm{B} T_\mathrm{I} - V_{\mathrm{O}^-}(x,y,z) \right) \Bigg] \\ \cdot \rho_\mathrm{I}(x,y,z,T_\mathrm{I}) \rho_\mathrm{A}(x,y,z,t)\, dx\, dy\, dz \Bigg\} + \underbrace{\left(\frac{3}{7} \right) \left(\frac{1}{3} \right) T_\mathrm{I} \bar{\epsilon} \nu_{ii}(T_\mathrm{I})}_{T_\mathrm{Heat}} \end{aligned} \tag{5.1}$$

Here, κ_el is the ion-atom elastic collision rate-coefficient based on the Langevin scattering model [223], $\left\langle \frac{\Delta E}{E} \right\rangle$ is the mean relative energy exchange, and $\langle E_\mathrm{A}(r) \rangle$ is the radius-dependent mean atom energy [164], which depends on the atom cloud temperature T_A, atom-ion mass ratio ξ and effective radial potential $V_\mathrm{eff}(x,y)$.

The trapping potential V_{O^-} is determined experimentally via photodetachment tomography, ρ_I and ρ_A are the spatial density distributions for the ion and the atom cloud respectively. The ion-ion heating rate T_{Heat}, is the same as described in Section 3.4.

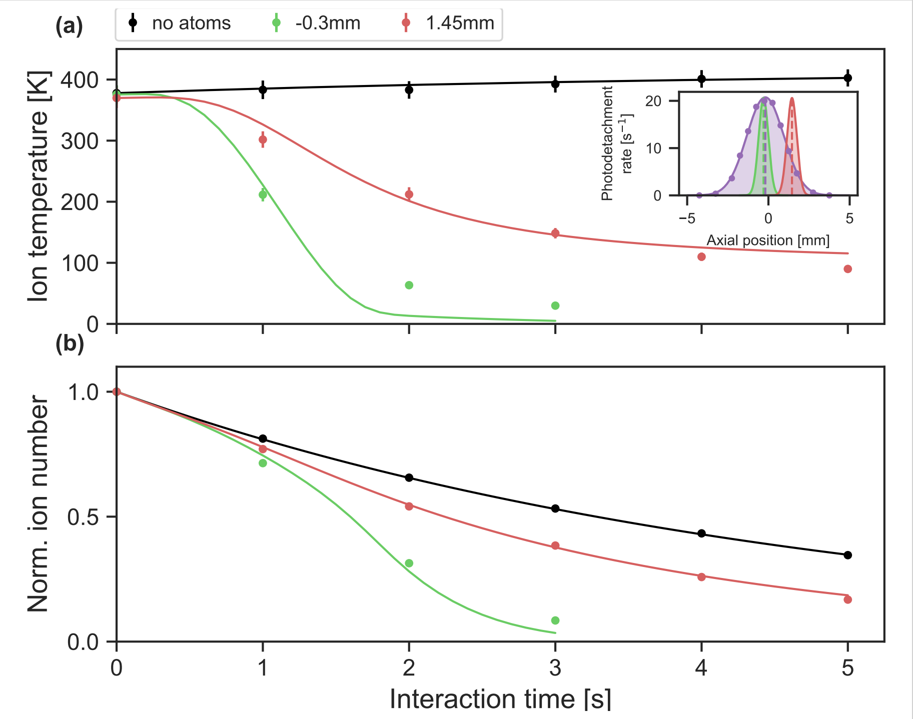

Figure 5.1: Cooling dynamics between O^- anions with rubidium for different relative positions between the atom-ion cloud. The measurements to account for the photodetachment losses due to cooling lasers are recorded without the presence of atoms and are shown in black. (a) The evolution of the ion temperature as a function of interaction time with the atoms is shown. The inset shows the relative positioning of the atom-ion clouds in the axial direction. The ions' spatial density distribution is shown in purple, along with an illustrated atom distribution centered at −0.3 mm (green) and 1.45 mm (red) relative to the center of the ion cloud. (b) The time evolution of the normalized ion number is shown. The points are the experimentally measured data and the solid curves represent the numerical solution corresponding to Equation 5.1 and Equation 5.2. Figure adapted from [168].

The time-evolution of the number of ions N_I shown in Figure 5.1 (b), is described as follows (including the temperature-dependent ion density distribution):

$$\dot{N}_I = \kappa_r N_I \int_{-\infty}^{\infty} \rho_I(x,y,z,T_I(t))\rho_A(x,y,z,t)\,dx\,dy\,dz - k_{\text{bgd}} N_I \tag{5.2}$$

where κ_r and k_{bgd} are reaction rate coefficient (in cm^3 s^{-1}) and the background loss rate (in s^{-1}) respectively.

By numerically solving the two coupled differential equations, Equation 5.1 and Equation 5.2, the O^- anion sympathetic cooling dynamics are described. A detailed description of the procedure for the experimental measurements and the derivation for the thermodynamic model is explained in [168].

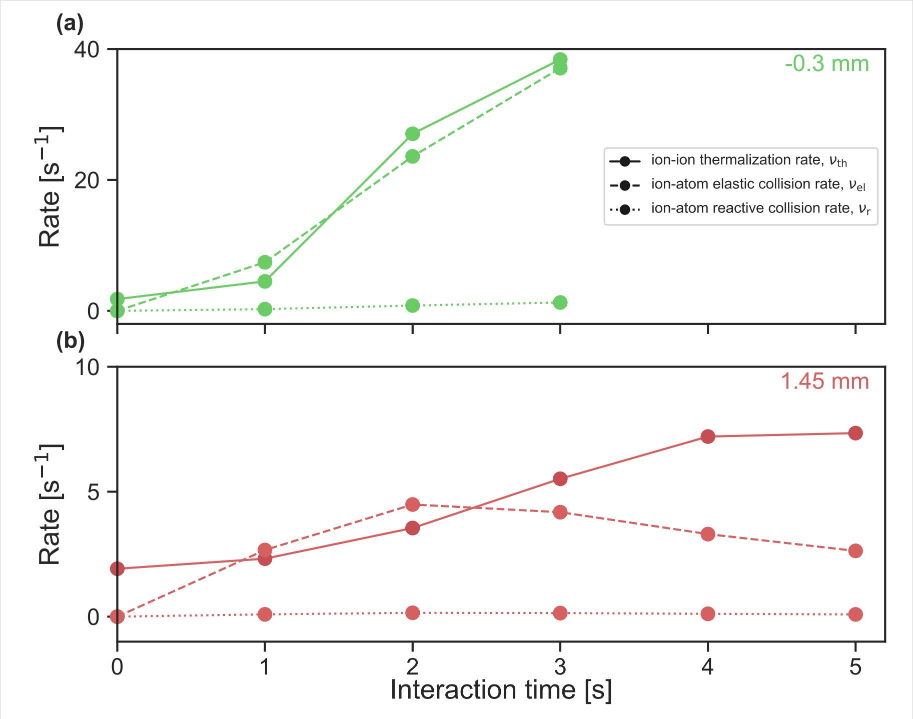

Figure 5.2: Rates of different relevant collisions that occur in the Rb-O^- system for two different atom-ion overlap configurations. (a) The atom-ion clouds are almost concentrically placed, with a relative axial displacement of $\Delta z = -0.3$ mm. It can be seen that the ion-ion thermalization rate (solid lines) and the ion-atom elastic collision rate (dashed lines) are on the same order of magnitude. The ion-atom reactive collision rate is also shown (dotted lines). In contrast, as shown in (b) for a relative axial displacement of $\Delta z = 1.45$ mm a clear separation between the two rates is seen. The points are the experimentally measured data, while the lines (solid, dashed, and dotted) are a guide to the eye. Figure adapted from [168].

It can be seen in Figure 5.1, that the derived thermodynamic model can explain the observed cooling dynamics reasonably well for the larger axial displacement between the atom-ion cloud, but significant deviations occur from the thermodynamic model for smaller displacements, i.e., for $\Delta z = -0.3$ mm particularly for longer interaction times. The deviation of the model can be explained by analyzing the timescales or rates of different types of collisions that occur in the system for two varying relative atom-ion overlaps, as shown in Figure 5.2. The ion-ion thermalization rate ν_{th}, is calculated as [168]:

$$\nu_{\mathrm{th}} = \frac{n_{\mathrm{I}} e^4 \log\Lambda_{\mathrm{ii}}}{12\epsilon_0^2 \sqrt{\pi^3 m (k_{\mathrm{B}} T_{\mathrm{I}})^3}} \tag{5.3}$$

where n_{I} is the ion number density, $\log\Lambda_{\mathrm{ii}}$ is the Coulomb logarithm, ϵ_0 is the vacuum permittivity and m is the mass of the ion. The ion-atom elastic collision rate ν_{el}, and reactive collision rate ν_{r} are described as follows:

$$\begin{aligned} \nu_{\mathrm{el}} &= \kappa_{\mathrm{el}} \int_{-\infty}^{\infty} \rho_{\mathrm{I}}(x,y,z,T_{\mathrm{I}}(t))\rho_{\mathrm{A}}(x,y,z,t)\,dxdydz \\ \nu_{\mathrm{r}} &= \kappa_{\mathrm{r}} \int_{-\infty}^{\infty} \rho_{\mathrm{I}}(x,y,z,T_{\mathrm{I}}(t))\rho_{\mathrm{A}}(x,y,z,t)\,dxdydz \end{aligned} \tag{5.4}$$

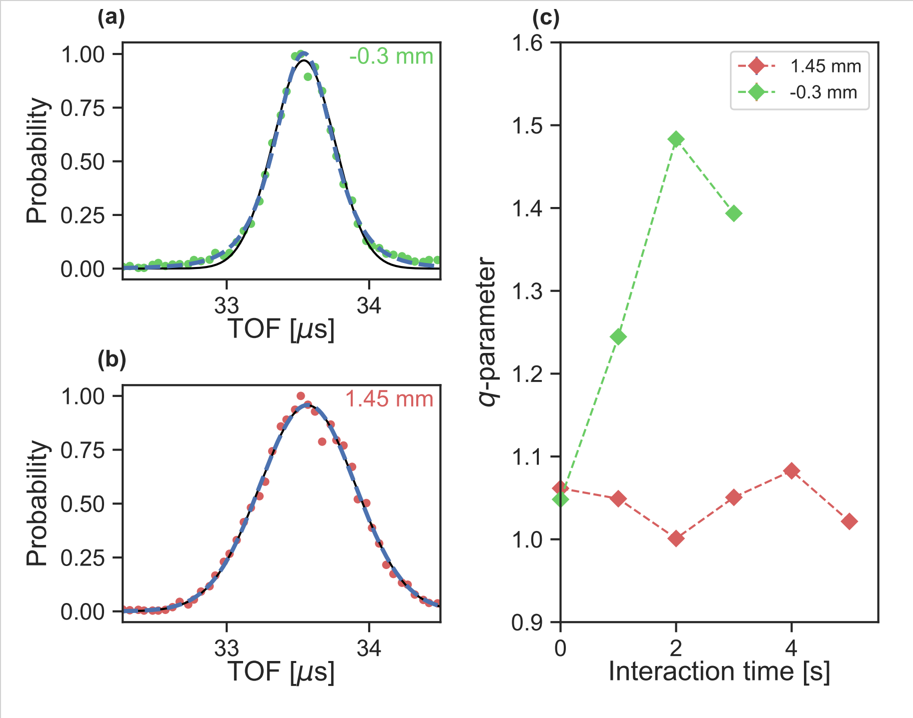

Figure 5.3: Resultant normalized TOF distributions for the two atom-ion relative displacements. (a) For $\Delta z = -0.3$ mm, after an interaction time of three seconds, shown in green, and (b) for $\Delta z = 1.45$ mm, after an interaction time of five seconds, shown in red. The black solid lines correspond to the Gaussian fit, whereas the blue dashed lines correspond to a Tsallis fit (as defined by Equation 5.5). The deviation, seen in the wings in (a), between the Gaussian and the Tsallis fit represents the deviation of the ion distribution from a thermal behavior. (c) The evolution of the Tsallis q-parameter as a function of time is shown. For $q \to 1$, the ion ensemble is said to be thermal whereas, for $q > 1$, the ensemble is said to be non-thermal.

The high atom-ion elastic collision rate for $\Delta z = -0.3$ mm, results in the breakdown of our thermodynamical model which assumes that the ion-ion thermalization rate is significantly higher than the rates of other processes in the system. As seen in Figure 5.2 (a), the ion-ion thermalization rate and the atom-ion elastic collision rate in this case are rather similar and unlike in Figure 5.2 (b) for $\Delta z = 1.45\,\mathrm{mm}$, no clear separation between the two time-scales (or rates) can be observed. This explains the deviation of the experimentally measured data from the model, for $\Delta z = -0.3\,\mathrm{mm}$, as our ion distribution is no longer thermal. This non-thermalicity of the ion distributions is also seen in their corresponding time-of-flight (TOF) distributions as shown in Figure 5.3 (a) and (b) for $\Delta z = -0.3\,\mathrm{mm}$ and $\Delta z = 1.45\,\mathrm{mm}$ respectively. The deviation from the thermal distribution is quantified by fitting the data with the following Tsallis fit [224, 225]:

$$\rho_{\mathrm{TOF}}(t) = A \cdot \left[1 + (1-q)\left(-\frac{(t-t_0)^2}{2\sigma_{\mathrm{TOF}}^2}\right)\right]^{\left(\frac{1}{1-q}\right)} \tag{5.5}$$

where q is the shaping parameter and σ_{TOF} is the width of the TOF distribution. For $q \to 1$, the ions exhibit a thermal distribution, and deviations from this regime represents the emergence of non-thermal regimes where the assumptions for the validity of our thermodynamic models breaks down [164], as seen for the case of $\Delta z = -0.3\,\mathrm{mm}$. The time-evolution of this q-parameter is shown in Figure 5.3 (c).

With these experimental investigations on the electronic quantum state-dependent detachment losses between Rb and O^-, we gained insights into the feasibility of the anion's sympathetic cooling in the system. By minimizing the fraction of excited rubidium in the atomic ensemble, we observed anion cooling to a final temperature of 30(2) K. The ions' radial potential could be well-approximated with a r^6 potential and the measured experimental data was reasonably described via a thermodynamic model, for the case when the ion-ion thermalization rate is greater than the atom-ion elastic or reactive collision rate. The photodetachment of the O^- anions due to the atom cooling lasers was the major loss channel in this system. A possible solution to circumvent this problem would be to confine Rb atoms in a dipole trap, which would not only suppress the ground-state detachment losses but would additionally suppress the photodetachment losses due to the lower photon energies of the laser beams used for dipole traps.

In conclusion, the hybrid atom ion traps, provide an ideal platform to study the sympathetic cooling of both molecular and atomic anions via ultracold atoms. With the right combination of the atom-anion species, ensuring a favorable mass ratio for efficient anion cooling, as well as by suppressing the reactive loss channels, it is possible to observe anion sympathetic cooling to the current state of the art regime of cryogenic temperatures.

CHAPTER 6

SYNOPSIS

Summary & Outlook

This work started with the aim to investigate the novel dynamics that occur in anions during their interaction with ultracold atoms in a hybrid atom-ion trap. In this chapter, the insights derived from the motivation, methods and results presented in this thesis are summarized. The important conclusions and their implications on the study of anion-neutral interactions and the future prospects of anion cooling to the ultracold regime are discussed.

The omnipresence of anions in varied environments has motivated several theoretical and experimental investigations on not only the fundamental and structural properties of anions but also on studies of their interaction dynamics with charged and neutral particles. Recent technological advancements in the hybrid trapping of atoms and ions in the same experimental apparatus have led to enormous developments in the field of exploring cation-neutral interactions [54, 56]. Some of these works include sympathetic cooling of a single ion in a BEC [63], rotational cooling in Coulomb-crystallized molecular ions [193], electronically excited state-dependent reactions [64, 68], and observation of Feschbach resonances in the ultracold s-wave regime which, until recently, had rather been elusive [226].

Motivated by the success of hybrid atom-ion traps in elucidating the cation-neutral interaction processes, the idea of combining anions and ultracold atoms in such a hybrid system was developed as a natural consequence. In the earlier experiments, hydroxide OH^- anions trapped in an octupole radio-frequency wire trap were combined with rubidium atoms in a magneto-optical trap [162]. Investigatory studies on anion-neutral associative electronic detachment reactions were discussed in the context of anion sympathetic cooling via an ultracold buffer gas. The experimental setup was later modified to trap atoms in a darkSPOT configuration to achieve high atom densities up to 10^{11} $\mathrm{cm}^3\mathrm{s}^{-1}$ and the flexibility to tune the electronic state configuration of the atomic system [171, 179].

Anion-atom diagnostics

Within the framework of this thesis, the key focus was on the investigations of the anion-neutral elastic and reactive collision processes. In order to model these dynamics, various diagnostic methods to characterize our atomic and anionic systems were employed, which were discussed in Chapter 2. The imaging of the high-density atomic cloud, via the well-established method of saturation absorption imaging, provided information on the time-evolution of the atom density and the total atom numbers [166, 181]. The number of atoms in the excited state was determined by imaging the atoms' fluorescence onto another CCD camera. The ratio of the number of atoms in the excited state to the total number of atoms gives the excited-state fraction for the rubidium atom cloud. For the anion ensemble, the spatial density distribution in both the axial and radial direction is determined via far-threshold photodetachment tomography [167, 180]. The ions' axial distribution is governed by the harmonic potential created by the static voltages on the trap's electrodes, whereas in the radial direction the ions' spatial distribution is influenced by the r^6 potential of an octupole trap.

This previously established technique provided insights into the ions' spatial distribution, but the information on the temperature of the ions in the trap was still missing. Although the ions in the trap are initialized with a room temperature buffer gas, it is well-known in the field of ion-trapping that rf-field induced micromotion may result in the heating of the ion ensemble during elastic processes. This renders the temperature determination of trapped ions in a multipole ion trap non-trivial, thus prompting a need for a thermometry method to determine trapped ions' translational temperature. Doppler spectroscopy is one possible thermometry method for translational temperature determination but requires the feasibility to address multiple electronic transitions, rarely found in anions. However, these are very time-consuming methods and require prior knowledge about the anion's spectroscopic properties.

With this motivation, we developed a time-efficient thermometry technique, discussed in Chapter 3, which can be used to determine the translational temperature of any anionic species trapped in a multipole ion trap. In our simulations, we use OH^- anions as an example case for the thermometry method and the results are published in [1].

We start by providing a detailed description of the experimental system with a focus on the octupole wire ion trap. A qualitative description of the potential landscape of the trap's electrodes during loading, trapping, and extraction of the ions onto the detector is provided. Traditionally, multipole ion traps employ the use of ideal cylindrical rods or hyperbolic rods due to their mechanical strength and durability. However, the optical access the wires provide is pivotal for the use of laser beams to overlap the trapped ions with ultracold atoms.

To determine the dynamics of ions trapped in a radio-frequency ion trap, an adiabatic approximation is used which provides a pseudo-static effective potential and the electric fields the ions experience in such traps [138]. The energy distributions of trapped ions, in three traps involving cylindrical rods, hyperbolic rods, and cylindrical wires are simulated in COMSOL Multiphysics 5.4 software [227]. It uses a finite-element method for the calculation of static potentials and rf fields in ideal multipole traps (with infinitely long wires and no endcaps). It was observed that for sufficiently high voltage, it is possible for the traps with cylindrical rods and wires to match the effective potential created via the use of hyperbolic rods. The discrepancy in the effective potential increases as one goes radially farther away from the center. Since in our system, the ions are initialized by a room temperature helium buffer gas pulse, and the ions mostly traverse in the inner regions of the trap, the influence of the observed deviations is minimal as long as the voltage is high enough to ensure stable trapping.

To further investigate the influence of the trap geometries on the temperature of the ions, the thermalization of the OH^- ensemble with a helium buffer gas at 293 K, was investigated with a Monte-Carlo approach. The mean speed of the ions $\bar{v}$ was calculated, in a molecular dynamics simulation, for each trap configuration, and the temperature of the ion ensemble T_I is given as:

$$T_\mathrm{I} = \frac{\pi m \bar{v}^2}{8 k_\mathrm{B}} \tag{6.1}$$

It was shown that the choice of rod geometry does not significantly alter the energy distribution or the temperature observed for the ion ensemble, as long as the voltages are scaled accordingly. However, the temperature observed is significantly larger than that of the buffer gas used which is attributed to the heating effects induced by the rf-field.

To characterize the temperature determination of trapped ions in our system, a 3D model of the setup including the endcap and shielding electrodes was used to simulate the potential landscape created. Following the Monte-Carlo approach, the energy distribution of OH^- ions, undergoing elastic collisions with a homogeneously distributed helium buffer gas, is calculated. The simulated data is represented via a Maxwell-Boltzmann as well as a Tsallis distribution, for comparing the ions' distribution in different energy regions. In the low to mid energy region, the ions' energy can be well described via a thermal distribution whereas in the high-energy region, non-thermal behavior emerges which is then better described via a Tsallis distribution.

The ions' spatial distribution in the axial direction is experimentally measured and compared to the ones obtained via simulations. While a deviation between the Gaussian and Tsallis distributions was seen near the peak of the ion distribution, no significant deviation near the wings was observed. This shows that the influence of the high energy tails representing the Tsallis-like behavior is negligible at the room temperature-like conditions. In our work, the temperatures are estimated via thermal ion distribution, and minor deviations from the thermal behavior, if any, are not taken into account. It is noteworthy to add that, particularly at lower ion temperatures, it is possible to observe a significantly non-thermal behavior and a more extensive characterization of the ion cloud's energy distribution via Tsallis statistics would be needed.

Two additional effects were also characterized during the scope of this work. One was the determination of the surface charges that accumulate on the printed circuit boards used in the trap assembly. These charges can change the effective potential that the ions experience and must therefore be accounted for. The photodetachment tomography measurements for a certain voltage on the endcap were performed and the surface charges were adjusted until the simulated ion distribution matches the measured data. Once the distributions match, the potential landscape used for subsequent simulations is then modified accordingly. Another effect arises due to the symmetry-breaking of the potential, which results in the regions of local potential minima which we term "pockets" [228]. This effect is more pronounced at lower temperatures as the ions spend more time in the local minima, resulting in an increased ion density in those regions.

Taking these effects into consideration, the temperature of the ions in the trap is mapped onto their time of flight to the detector. This provides a calibration curve as well as establishes a linear relationship between the variance of the ions' TOF distribution measured experimentally and the temperature of trapped ions. With this, a time-efficient and reliable thermometry technique was developed for our system. Further, the results of this work are applicable to any anionic species stored in a multipole trap.

In addition to the published work, an analytical description of the linear mapping between the ion temperature and their TOF is discussed in Section 3.3. A one-dimensional case is considered where ions, starting at the same position with velocities sampled from a thermal distribution, are directed towards a detector. Accounting for the turn-around time of the ions and the time of flight incurred due to different acceleration stages, we show that a linear relationship between the ions' TOF and their velocity exists. This idea can be extended to any extraction potential by approximating it as a sum of several linear accelerating stages and the linearity between ions' TOF variance and their translational temperature is conserved.

In Section 3.4, we demonstrate the application of this thermometry method by determining the temperature of OH^- anions as they undergo forced evaporative cooling via a far-threshold photodetachment beam. The hotter ions at the periphery of the ion ensemble in the trap are dynamically removed via a laser beam moving at a chosen speed towards the center of the trap. The remaining ions then rethermalize to a colder temperature. The initial position of the laser beam always remains the same and the effective interaction time of the ions with the laser beam is determined by the beam's final position. The ions' TOF distribution is recorded and with the mapping established, a final temperature of 2.2(8) K is obtained for a beam speed of $v_{\mathrm{PD}} = 1.0\ \mathrm{mm\ s^{-1}}$. The experimental data are represented by a full thermodynamical model, with all the parameters like the trapping potential, ion-ion heating rate, etc. pre-determined without any fitting parameters. The time-evolution of the ion temperature obtained experimentally via the TOF thermometry method and the temperature from the theoretical model are found to be in reasonable agreement with one another. With these measurements, the technique of forced evaporative cooling proposed decades ago in [92], is experimentally demonstrated for the first time and temperatures below those obtained via cryogenic buffer gas, are reported. This technique presents a novel case of the anion-photon interactions, where any anionic species can be cooled to the Kelvin regime via laser-induced forced evaporative cooling.

Investigations on anion-atom interactions

With the diagnostic methods, we have the temporal evolution of the spatial density distribution of the atom and ion cloud determined, including the possibility to map the temperature evolution of the ions as they undergo interaction with other particles. Employing these tools one can model the anion-atom collisions as they are overlapped in a hybrid atom-ion trap. Once the ions and atoms are overlapped, the elastic collisions result in the cooling of ions and the reactive collisions result in the loss of ions from the system due to different possible reaction channels. For molecular anions, another kind of inelastic collisions are additionally possible, where the ions undergo cooling in their internal (rotational and vibrational) degree of freedom, but in this work, we limit ourselves to investigating the interplay between elastic and reactive collisions in the anion-atom system.

In Chapter 4, we investigated the dynamics of the molecular anions interacting with ultracold Rb. The first ion species of interest was the OH^-, as it is one of the simplest and most well-studied molecular anions. Preliminary investigations on the Rb-OH^- system were performed in [162] and the reactive collisions were studied in the context of anion sympathetic cooling, where the reaction rate for the associative electronic detachment (AED) process was derived. It was conjectured that by limiting the interaction between the ions and the atoms in the MOT, cooling the ion via "good" elastic collisions with the neutral partner might still be feasible. The system of Rb-OH^- has also been a point of interest for several theoretical investigations, where the choice of different effective core potentials led to divergent results for AED between OH^- and rubidium in its electronic ground state [84, 85, 86]. While the earlier theory [84] predicted this channel to be closed (as long as the ions are in their vibrational ground state), the recent theoretical investigations in [85, 86] predicted a finite probability for AED reaction to occur even for rubidium in its electronic ground state. In our system, we ascertain that the ions undergo thermalization with a helium buffer gas at room temperature which ensures that the ions are in their vibrational ground state. So while the former theory would predict AED reaction to being suppressed as long as the amount of excited rubidium in the atomic ensemble is low enough, the latter theory suggests appreciable ion losses due to AED even for the case of Rb in its ground state.

The darkSPOT configuration in the current setup provides a possibility to tune the electronic state of the neutral collision partner to experimentally investigate the ion losses incurred due to the AED reaction channel. The key focus was to identify and quantify these reactive loss channels to further the understanding of anion sympathetic cooling. As it is rightfully said, *"Beauty lies in the eyes of the beholder"*, what started as an investigatory study into the "bad" reactive loss processes, revealed novel interaction dynamics between a closed-shell anion OH^- and an alkali metal atom Rb and formed the basis of the work published in [2]. The reactive collisions between OH^- and Rb in its electronic ground state (^2S) and excited state (^2P) were theoretically and experimentally studied at 355(10) K. It was observed that of all the different reactive processes that are energetically feasible, AED is the most likely process to occur in the system resulting in the formation of a neutral molecule via $\text{Rb} + OH^- \rightarrow \text{RbOH} + e^-$.

The potential energy surfaces as a function of the distance between the Rb atom and the center of mass of OH^- anion were calculated, and the crossing points between the anionic and neutral curves were investigated to determine the probability of the occurrence of the AED reaction. For ground-state rubidium, when the angle of approach between the atom and anion is $\theta \geq 20°$, then the crossing becomes inaccessible, while for $\theta < 20°$, the crossing is found below the energy of the entrance channel, and the AED reaction proceeds in such a configuration. The dipole moment of the Rb-OH system decreases with decreasing inter-atomic distance but increases with increasing θ. For higher angles of approach, the dipole moment is high enough to support a stable anionic state. But for certain angles of approach, the crossing occurs at a short range, as the electron is bound to the intermediate complex primarily via weak dipolar forces. Due to these steric influences, the expected reaction rate is much lower than that predicted by the Langevin capture rate. For excited state rubidium, a reaction rate close to the Langevin rate is expected, since in this case a short-lived dipole-bound intermediate complex is formed and it is shown that all possible potential energy surfaces pertaining to the excited state rubidium lead to a crossing into the autodetachment region.

Experimentally, we measure the ion losses as a function of interaction time with the atomic cloud. We determine the reaction rate coefficient κ for a certain fraction of excited Rb in the atomic ensemble as discussed in Chapter 2. It is to be noted that tomographic scans for different anion-atom interaction times showed no appreciable change in the OH^- ions' spatial density distribution, thus the ion-atom overlap is calculated with an ion distribution constant in time. The measurements are repeated for varying excited state configurations of the rubidium and a linear dependency between the excited state fraction and the corresponding reaction rate coefficient is established yielding the AED reaction coefficient between OH^- and rubidium in the ground state and excited state. For ground-state Rb, our experimental findings are in agreement with the *ab initio* calculations. As expected, a reaction rate much lower than the Langevin reaction rate is observed, highlighting the influence of steric effects in the formation of a stable intermediate dipolar complex and in mediating the AED reaction. However, for the excited state case, the deviation of the experimentally observed reaction rate coefficient from that obtained via both the Langevin capture model and *ab initio* calculations, hints at the presence of other dynamical stabilization processes that are not taken into account in the current study. In this work, we expanded the understanding of AED reaction dynamics and demonstrated the dominant influence of a dipole-bound state in mediating the reaction process.

The finite reaction rate observed for the ground state Rb interacting with OH^-, also showed that the AED reaction rates in the system are enough to induce significant ion losses and thus, suppress efficient anion sympathetic cooling via elastic collisions with a Rb buffer gas. This motivated the study of collision dynamics in Rb and hydrated hydroxide $OH^-(H_2O)$ anions, presented in Section 4.3, where a smaller atom-to-ion mass ratio, provides more favorable conditions for efficient sympathetic cooling of the molecular anions, via a localized ultracold buffer gas [163, 164, 170].

We described the process of ion cloud preparation and selection of $OH^-(H_2O)$ anionic species in the trap, which was then overlapped with an ultracold rubidium cloud. For an excited state fraction of 10.5(7)%, a final temperature of 26(3) K is attained in less than eight seconds and a reaction rate coefficient of $\kappa = 1.42(4) \cdot 10^{-9}\ \mathrm{cm^3 s^{-1}}$ is determined. However, an offset in the ion number is observed which hints at the presence of other anionic species in the trap. This is also confirmed by the offset seen in photodetachment tomography, where for a very long interaction time with the far-threshold laser beam all $OH^-(H_2O)$ anions should have been photodetached. The source of the other species could not be conclusively determined and introduces an additional source of systematic error in the determination of the reaction rate coefficient in the system. Nevertheless, it can be safely said that, within the systematics of our system, the reaction rate is comparable to that in the Rb-OH^- system, but a favorable mass ratio of the Rb-$OH^-(H_2O)$ system results in an efficient cooling of the anions via collisions with ultracold Rb buffer gas.

The ratio of elastic-to-reactive collisions, in the anion-atom interactions, can be increased by suppressing the reactive losses. Theoretical investigations on O^- with alkali metals showed that these alkali monoxide systems support electronic ground states that are stable against autodetachment [221, 222]. In our experimental setup, due to similarity in their mass-to-charge ratio, in addition to OH^-, O^- anions are also efficiently trapped. Thus, with slight changes in the ion loading and trapping procedure, it was possible to create an ion cloud consisting only of O^- anions. The dynamics of these trapped atomic anions with ultracold Rb atoms are presented in Chapter 5. The dependence of the electron detachment processes on the electronic quantum state of the neutral was investigated, with the focus to find a system where the reactive losses with ground state rubidium are suppressed. The experimental results were supplemented with relevant potential energy surfaces and encapsulated in the published work in [3].

Different loss channels for O^- interacting with Rb in its electronic ground state (^2S) and excited state (^2P) were identified. Depending on anion-neutral energetics, for the ground state Rb, the only reactive process found to be energetically possible is the AED. In the case of the excited state Rb, in addition to AED, other loss processes like Penning detachment, charge transfer, and electronic to kinetic energy transfer are also found to be energetically feasible. Since in our system we cannot distinguish between the reaction products (and hence the reaction channels), we only observe the total loss due to the different channels.

Similar to the Rb-OH^- system, the ion losses were measured for varying interaction times with the Rb atoms, and for different configurations of the excited state fraction in the atomic ensemble. The time evolution of the ions' density distribution was estimated in accordance with the interpolation function for the ion temperature, and the ion-atom overlap was calculated. With the knowledge of these parameters, the reaction rate coefficient for each configuration was determined. A linear fit through the reaction rate coefficients as a function of the excited state fraction provided the reaction rates for the case of the ground state and excited state rubidium interacting with O^-. A rate coefficient consistent with zero was found in the case of ground state Rb. This was further supported via the calculated potential energy surfaces where the four molecular states pertaining to the ground state channel were found to be stable against autodetachment. For the excited state rubidium, a reaction rate lower than the Langevin rate but similar to the Rb-OH^- case was found, hinting again at the presence of other processes that suppress the coupling into the autodetachment region.

With suppressed reactive losses, it was possible to observe sympathetic cooling of O^- anions during its interaction with Rb atoms. The results for different axial displacements (thus, varying degrees of overlap) between the two clouds were studied and shown in Section 5.3. The excited-state fraction in the atom ensemble was minimized and for nearly concentric atom-ion clouds, a final temperature of 30(2) K was attained in three seconds. The final temperature attained was limited by the ion losses induced by the cooling light used for the atom trapping. The evolution of ion temperature and number were represented via a thermodynamical model. The main assumption of the model is that the ion-ion thermalization rate is significantly higher than the ion-atom elastic or reactive collision rate. It was shown that this assumption holds valid for the case of higher relative axial displacement between the two clouds and the ions' temporal evolution is well-represented by the thermodynamical model, which breaks down for the case of nearly concentric clouds due to the emergence of non-thermal behavior.

During the framework of this thesis, we could resolve and understand the different dynamics prevalent in the anion-neutral collisions, when the two species are co-trapped in a hybrid atom-ion trap. The key focus was on the feasibility of the anion sympathetic cooling via ultracold rubidium, which paved the way for the exploration of reactive collisions involving molecular as well as atomic anions revealing interaction novel dynamics, presented in the published works.

Outlook on future experiments

The hybrid atom-ion traps present themselves as a platform to study ion-atom interaction processes. For molecular anions, a system with a more favorable atom-to-ion mass ratio can be employed to explore the prospects of anion sympathetic cooling. With very few technical modifications, higher orders of hydrated hydroxides, $OH^-(H_2O)_l$ where $l > 1$, can be trapped in the system. An improved mass ratio and the conjectured low reactive losses would provide favorable conditions for anion cooling via ultracold Rb. Investigations on the reactive collisions and comparisons with OH^- anions would reveal insights into the effect of hydration on gas-phase reactions [165]. In higher-order clusters, the study of specific isomers and their influence on the reactivity of the system can be probed via photodetachment methods. Interaction of C_2^- anions with lighter alkali atoms, like Li is also a system of interest from the perspective of sympathetic cooling, where the ground-state reactive channels are predicted to be closed. This provides a pre-cooling technique for the Doppler cooling of these anions as proposed in [91] but would require major experimental modifications [220]. Additionally, with suppressed reactive losses, it is also possible to probe the internal (vibrational and/or rotational) states of the molecular anions, in such hybrid systems [192].

In the case of atomic O^- anions, we identified Rb-O^- as a system where the loss channels for the ground state atom are suppressed. Thus, trapping atoms in a far-threshold dipole trap would not only eliminate the excited-state reactive loss channels but also the ion losses incurred via the cooling lasers. This would increase the lifetime of the ions in the trap and improve the elastic-to-reactive collision ratio, critical for sympathetic cooling.

Experimental investigations of the reaction dynamics of these anions are also of pivotal importance in the context of quantum chemistry research. The possibility to differentiate the reaction channels is an additional technical feature that could improve the experimental work on exploring the reaction dynamics. Improved theoretical models, providing detailed insights into the stability of the excited states, and accounting for possible non-adiabatic effects in such systems can bridge the gap between the theoretical and experimental results.

It is evident that with our work on the anion-neutral collisions, we have only scratched the surface of a plethora of anionic systems whose interactions with other neutral (or charged) species possess rich and novel dynamics. Investigations into these systems would not only provide insights for fundamental physics and chemistry research to build up new technologies but would also reveal answers to questions pertaining to the formation and destruction channels of particles in the Universe and about our life on Earth, as we know it.

BIBLIOGRAPHY

[1] M. Nötzold, S. Z. Hassan, J. Tauch, et al. “Thermometry in a Multipole Ion Trap”. Appl. Sci. **10**(15), 5264 (2020).

[2] S. Z. Hassan, J. Tauch, M. Kas, et al. “Associative detachment in anion-atom reactions involving a dipole-bound electron”. Nat. Commun. **13**(1), 818 (2022).

[3] S. Z. Hassan, J. Tauch, M. Kas, et al. “Quantum state-dependent anion–neutral detachment processes”. J. Chem. Phys. **156**(9), 094304 (2022).

[4] W. Ketterle. “Nobel lecture: When atoms behave as waves: Bose-Einstein condensation and the atom laser”. Rev. Mod. Phys. **74**, 1131 (2002).

[5] D. van Delft and P. Kes. “The discovery of superconductivity”. Phys. Today **63**(9), 38 (2010).

[6] P. Kapitza. “Viscosity of Liquid Helium below the λ-Point”. Nature **141**(3558), 74 (1938).

[7] J. F. Allen and A. D. Misener. “Flow of Liquid Helium II”. Nature **141**(3558), 75 (1938).

[8] D. D. Osheroff, R. C. Richardson, and D. M. Lee. “Evidence for a New Phase of Solid He^3”. Phys. Rev. Lett. **28**, 885 (1972).

[9] A. Ashkin. “Atomic-Beam Deflection by Resonance-Radiation Pressure”. Phys. Rev. Lett. **25**, 1321 (1970).

[10] A. Ashkin. “Trapping of Atoms by Resonance Radiation Pressure”. Phys. Rev. Lett. **40**, 729 (1978).

[11] W. D. Phillips, J. V. Prodan, and H. J. Metcalf. “Laser cooling and electromagnetic trapping of neutral atoms”. J. Opt. Soc. Am. B **2**(11), 1751 (1985).

[12] S. Chu. “Nobel Lecture: The manipulation of neutral particles”. Rev. Mod. Phys. **70**, 685 (1998).

[13] C. N. Cohen-Tannoudji. “Nobel Lecture: Manipulating atoms with photons”. Rev. Mod. Phys. **70**, 707 (1998).

[14] J. Weiner, V. S. Bagnato, S. Zilio, and P. S. Julienne. “Experiments and theory in cold and ultracold collisions”. Rev. Mod. Phys. **71**, 1 (1999).

[15] G. K. Campbell and W. D. Phillips. “Ultracold atoms and precise time standards”. Philos. Trans. R. Soc. A **369**(1953), 4078 (2011).

[16] X. Zhang and J. Ye. “Precision measurement and frequency metrology with ultracold atoms”. Natl. Sci. Rev. **3**(2), 189 (2016).

[17] F. Sorrentino, G. Ferrari, N. Poli, et al. “Laser cooling and trapping of atomic strontium for ultracold atom physics, high-precision spectroscopy and quantum sensors”. Mod. Phys. Lett. B **20**(21), 1287 (2006).

[18] J. Ye, S. Blatt, M. M. Boyd, et al. “Precision Measurement Based on Ultracold Atoms and Cold Molecules”. Int. J. Mod. Phys. D **16**(12b), 2481 (2007).

[19] M. Lewenstein, A. Sanpera, and V. Ahufinger Ultracold Atoms in Optical Lattices: Simulating quantum many-body systems (Oxford Scholarship Online: December 2013, 2012).

[20] J. Eisert, M. Friesdorf, and C. Gogolin. “Quantum many-body systems out of equilibrium”. Nat. Phys. **11**(2), 124 (2015).

[21] I. Bloch, J. Dalibard, and S. Nascimbène. “Quantum simulations with ultracold quantum gases”. Nat. Phys. **8**(4), 267 (2012).

[22] C. Gross and I. Bloch. “Quantum simulations with ultracold atoms in optical lattices”. Science **357**(6355), 995 (2017).

[23] F. Schäfer, T. Fukuhara, S. Sugawa, et al. “Tools for quantum simulation with ultracold atoms in optical lattices”. Nat. Rev. Phys. **2**(8), 411 (2020).

[24] K.-A. B. Soderberg, N. Gemelke, and C. Chin. “Ultracold molecules: vehicles to scalable quantum information processing”. New J. Phys. **11**(5), 055022 (2009).

[25] I. I. Ryabtsev, K. Y. Mityanin, I. I. Beterov, et al. “Quantum Information Processing on the Basis of Single Ultracold Atoms in Optical Traps”. Optoelectron. Instrum. Data Process. **56**(5), 510 (2020).

[26] W. Hofstetter and T. Qin. “Quantum simulation of strongly correlated condensed matter systems”. J. Phys. B: At. Mol. Opt. Phys. **51**(8), 082001 (2018).

[27] Y. Wang, F. Dolde, J. Biamonte, et al. “Quantum Simulation of Helium Hydride Cation in a Solid-State Spin Register”. ACS Nano **9**(8), 7769 (2015).

[28] E. Zohar, J. I. Cirac, and B. Reznik. “Quantum simulations of gauge theories with ultracold atoms: Local gauge invariance from angular-momentum conservation”. Phys. Rev. A **88**, 023617 (2013).

[29] C. Gardiner and P. Zoller The Quantum World of Ultra-Cold Atoms and Light Book I: Foundations of Quantum Optics (Imperial College Press, 2014).

[30] D. Browne, S. Bose, F. Mintert, and M. Kim. “From quantum optics to quantum technologies”. Prog. Quantum. Electron. **54**, 2 (2017). Special issue in honor of the 70th birthday of Professor Sir Peter Knight FRS.

[31] F. Penning. “Die glimmentladung bei niedrigem druck zwischen koaxialen zylindern in einem axialen magnetfeld”. Physica **3**(9), 873 (1936).

[32] H. Dehmelt. “Radiofrequency Spectroscopy of Stored Ions I: Storage”. Adv. At. Mol. Opt. **3**, 53 (1968).

[33] H. Dehmelt. “Experiments with an Isolated Subatomic Particle at Rest (Nobel Lecture)”. Angew. Chem. Int. Ed. **29**(7), 734 (1990).

[34] W. Paul. “Electromagnetic Traps for Charged and Neutral Particles (Nobel Lecture)”. Angew. Chem. Int. Ed. **29**(7), 739 (1990).

[35] W. Neuhauser, M. Hohenstatt, P. Toschek, and H. Dehmelt. “Optical-Sideband Cooling of Visible Atom Cloud Confined in Parabolic Well”. Phys. Rev. Lett. **41**, 233 (1978).

[36] D. J. Wineland, R. E. Drullinger, and F. L. Walls. “Radiation-Pressure Cooling of Bound Resonant Absorbers”. Phys. Rev. Lett. **40**, 1639 (1978).

[37] W. Neuhauser, M. Hohenstatt, P. E. Toschek, and H. Dehmelt. “Localized visible Ba^+ mono-ion oscillator”. Phys. Rev. A **22**, 1137 (1980).

[38] D. J. Wineland. “Nobel Lecture: Superposition, entanglement, and raising Schrödinger’s cat”. Rev. Mod. Phys. **85**, 1103 (2013).

[39] M. Steck and Y. A. Litvinov. “Heavy-ion storage rings and their use in precision experiments with highly charged ions”. Prog. Part. Nucl. Phys. **115**, 103811 (2020).

[40] D. Müll, F. Grussie, K. Blaum, et al. “Metastable states of Si^- observed in a cryogenic storage ring”. Phys. Rev. A **104**, 032811 (2021).

[41] O. Novotný, P. Wilhelm, D. Paul, et al. “Quantum-state-selective electron recombination studies suggest enhanced abundance of primordial HeH^+”. Science **365**(6454), 676 (2019).

[42] H. Kreckel, O. Novotný, and A. Wolf. “Astrochemical studies at the Cryogenic Storage Ring”. Phil. Trans. R. Soc. A. **377**(2154), 20180412 (2019).

[43] L. S. Brown and G. Gabrielse. “Precision spectroscopy of a charged particle in an imperfect Penning trap”. Phys. Rev. A **25**, 2423 (1982).

[44] H. Loh, K. C. Cossel, M. C. Grau, et al. “Precision Spectroscopy of Polarized Molecules in an Ion Trap”. Science **342**(6163), 1220 (2013).

[45] S. Willitsch. “Coulomb-crystallised molecular ions in traps: methods, applications, prospects”. Int. Rev. Phys. Chem. **31**(2), 175 (2012).

[46] D. Zhang and S. Willitsch. “Cold ion chemistry”. arXiv: Chemical Physics, arXiv:1703.07133v1 (2017).

[47] G. Z. K. Horvath, R. C. Thompson, and P. L. Knight. “Fundamental physics with trapped ions”. Contemp. Phys. **38**(1), 25 (1997).

[48] M. G. Kozlov, M. S. Safronova, J. R. Crespo López-Urrutia, and P. O. Schmidt. “Highly charged ions: Optical clocks and applications in fundamental physics”. Rev. Mod. Phys. **90**, 045005 (2018).

[49] M. Müller, K. Hammerer, Y. L. Zhou, et al. “Simulating open quantum systems: from many-body interactions to stabilizer pumping”. New J. Phys. **13**(8), 085007 (2011).

[50] C. Schneider, D. Porras, and T. Schaetz. “Experimental quantum simulations of many-body physics with trapped ions”. Rep. Prog. Phys. **75**(2), 024401 (2012).

[51] J. P. Home, D. Hanneke, J. D. Jost, et al. “Complete Methods Set for Scalable Ion Trap Quantum Information Processing”. Science **325**(5945), 1227 (2009).

[52] J. M. Amini, H. Uys, J. H. Wesenberg, et al. “Toward scalable ion traps for quantum information processing”. New J. Phys. **12**(3), 033031 (2010).

[53] A. Bermudez, T. Schaetz, and M. B. Plenio. “Dissipation-Assisted Quantum Information Processing with Trapped Ions”. Phys. Rev. Lett. **110**, 110502 (2013).

[54] M. Tomza, K. Jachymski, R. Gerritsma, et al. “Cold hybrid ion-atom systems”. Rev. Mod. Phys. **91**, 035001 (2019).

[55] S. Schmid, A. Härter, and J. H. Denschlag. “Dynamics of a Cold Trapped Ion in a Bose-Einstein Condensate”. Phys. Rev. Lett. **105**, 133202 (2010).

[56] A. Härter and J. H. Denschlag. “Cold atom–ion experiments in hybrid traps”. Contemp. Phys. **55**(1), 33 (2014).

[57] R. Côté. “Chapter Two - Ultracold Hybrid Atom–Ion Systems”. Adv. At. Mol. Opt. **65**, 67 (2016).

[58] W. W. Smith, O. P. Makarov, and J. Lin. “Cold ion–neutral collisions in a hybrid trap”. J. Mod. Opt. **52**(16), 2253 (2005).

[59] Grier, Andrew T. and Cetina, Marko and Oručević, Fedja and Vuletić, Vladan. “Observation of Cold Collisions between Trapped Ions and Trapped Atoms”. Phys. Rev. Lett. **102**, 223201 (2009).

[60] F. H. J. Hall, M. Aymar, N. Bouloufa-Maafa, et al. “Light-Assisted Ion-Neutral Reactive Processes in the Cold Regime: Radiative Molecule Formation versus Charge Exchange”. Phys. Rev. Lett. **107**, 243202 (2011).

[61] W. M. Itano, J. C. Bergquist, J. J. Bollinger, and D. J. Wineland. “Cooling methods in ion traps”. Physica Scripta **T59**, 106 (1995).

[62] C. Zipkes, S. Palzer, L. Ratschbacher, et al. “Cold Heteronuclear Atom-Ion Collisions”. Phys. Rev. Lett. **105**, 133201 (2010).

[63] C. Zipkes, S. Palzer, C. Sias, and M. Köhl. “A trapped single ion inside a Bose–Einstein condensate”. Nature **464**(7287), 388 (2010).

[64] L. Ratschbacher, C. Zipkes, C. Sias, and M. Köhl. “Controlling chemical reactions of a single particle”. Nat. Phys. **8**(9), 649 (2012).

[65] W. G. Rellergert, S. T. Sullivan, S. Kotochigova, et al. “Measurement of a Large Chemical Reaction Rate between Ultracold Closed-Shell ^{40}Ca Atoms and Open-Shell ^{174}Yb^{+} Ions Held in a Hybrid Atom-Ion Trap”. Phys. Rev. Lett. **107**, 243201 (2011).

[66] S. T. Sullivan, W. G. Rellergert, S. Kotochigova, and E. R. Hudson. “Role of Electronic Excitations in Ground-State-Forbidden Inelastic Collisions Between Ultracold Atoms and Ions”. Phys. Rev. Lett. **109**, 223002 (2012).

[67] K. Ravi, S. Lee, A. Sharma, et al. “Cooling and stabilization by collisions in a mixed ion–atom system”. Nat. Commun. **3**(1), 1126 (2012).

[68] P. Puri, M. Mills, I. Simbotin, et al. “Reaction blockading in a reaction between an excited atom and a charged molecule at low collision energy”. Nat. Chem. **11**(7), 615 (2019).

[69] F. H. Hall, P. Eberle, G. Hegi, et al. “Ion-neutral chemistry at ultralow energies: dynamics of reactive collisions between laser-cooled Ca^{+} ions and Rb atoms in an ion-atom hybrid trap”. Mol. Phys. **111**(14-15), 2020 (2013).

[70] F. H. Hall, M. Aymar, M. Raoult, et al. “Light-assisted cold chemical reactions of barium ions with rubidium atoms”. Mol. Phys. **111**(12-13), 1683 (2013).

[71] S. Haze, S. Hata, M. Fujinaga, and T. Mukaiyama. “Observation of elastic collisions between lithium atoms and calcium ions”. Phys. Rev. A **87**, 052715 (2013).

[72] R. Côté and A. Dalgarno. “Ultracold atom-ion collisions”. Phys. Rev. A **62**, 012709 (2000).

[73] S. Haze, M. Sasakawa, R. Saito, et al. “Cooling Dynamics of a Single Trapped Ion via Elastic Collisions with Small-Mass Atoms”. Phys. Rev. Lett. **120**, 043401 (2018).

[74] D. Gerlich. “Ion-neutral collisions in a 22-pole trap at very low energies”. Physica Scripta **T59**, 256 (1995).

[75] T. Sikorsky, Z. Meir, R. Ben-shlomi, et al. “Spin-controlled atom–ion chemistry”. Nat. Commun. **9**(1), 920 (2018).

[76] T. Sikorsky, M. Morita, Z. Meir, et al. “Phase Locking between Different Partial Waves in Atom-Ion Spin-Exchange Collisions”. Phys. Rev. Lett. **121**, 173402 (2018).

[77] H. A. Fürst, N. V. Ewald, T. Secker, et al. "Prospects of reaching the quantum regime in Li–Yb^+ mixtures". J. Phys. B: At. Mol. Opt. Phys. **51**(19), 195001 (2018).

[78] C. Chin, R. Grimm, P. Julienne, and E. Tiesinga. "Feshbach resonances in ultracold gases". Rev. Mod. Phys. **82**, 1225 (2010).

[79] Tomza, Michał and Koch, Christiane P. and Moszynski, Robert. "Cold interactions between an Yb^+ ion and a Li atom: Prospects for sympathetic cooling, radiative association, and Feshbach resonances". Phys. Rev. A **91**, 042706 (2015).

[80] K. Jachymski and A. Negretti. "Quantum simulation of extended polaron models using compound atom-ion systems". Phys. Rev. Res. **2**, 033326 (2020).

[81] H. Hirzler, E. Trimby, R. S. Lous, et al. "Controlling the nature of a charged impurity in a bath of Feshbach dimers". Phys. Rev. Res. **2**, 033232 (2020).

[82] H. Doerk, Z. Idziaszek, and T. Calarco. "Atom-ion quantum gate". Phys. Rev. A **81**, 012708 (2010).

[83] R. Gerritsma, A. Negretti, H. Doerk, et al. "Bosonic Josephson Junction Controlled by a Single Trapped Ion". Phys. Rev. Lett. **109**, 080402 (2012).

[84] J. N. Byrd, H. H. Michels, J. A. Montgomery, and R. Côté. "Associative detachment of rubidium hydroxide". Phys. Rev. A **88**, 032710 (2013).

[85] M. Kas, J. Loreau, J. Liévin, and N. Vaeck. "Ab initio study of reactive collisions between $Rb(^2S)$ or $Rb(^2P)$ and $OH^-(^1\Sigma^+)$". J. Chem. Phys. **144**(20), 204306 (2016).

[86] M. Kas, J. Loreau, J. Liévin, and N. Vaeck. "Ab initio study of the neutral and anionic alkali and alkaline earth hydroxides: Electronic structure and prospects for sympathetic cooling of OH^-". J. Chem. Phys. **146**(19), 194309 (2017).

[87] A. Kellerbauer, A. Fischer, and U. Warring. "Measurement of the Zeeman effect in an atomic anion: Prospects for laser cooling of Os^-". Phys. Rev. A **89**, 043430 (2014).

[88] G. Cerchiari, A. Kellerbauer, M. S. Safronova, et al. "Ultracold Anions for High-Precision Antihydrogen Experiments". Phys. Rev. Lett. **120**, 133205 (2018).

[89] M.-j. Wan, D.-h. Huang, Y. Yu, and Y.-g. Zhang. “Laser cooling of the OH^- molecular anion in a theoretical investigation”. Phys. Chem. Chem. Phys. **19**, 27360 (2017).

[90] P. Yzombard, M. Hamamda, S. Gerber, et al. “Laser Cooling of Molecular Anions”. Phys. Rev. Lett. **114**, 213001 (2015).

[91] S. Gerber, J. Fesel, M. Doser, and D. Comparat. “Photodetachment and Doppler laser cooling of anionic molecules”. New J. Phys. **20**(2), 023024 (2018).

[92] A. Crubellier. “Theory of laser evaporative cooling of trapped negative ions. I. Harmonically bound ions and RF traps”. J. Phys. B: At. Mol. Opt. Phys. **23**(20), 3585 (1990).

[93] G. Cerchiari, P. Yzombard, and A. Kellerbauer. “Laser-Assisted Evaporative Cooling of Anions”. Phys. Rev. Lett. **123**, 103201 (2019).

[94] G. B. Andresen, M. D. Ashkezari, M. Baquero-Ruiz, et al. (ALPHA Collaboration). “Evaporative Cooling of Antiprotons to Cryogenic Temperatures”. Phys. Rev. Lett. **105**, 013003 (2010).

[95] S. Schippers, E. Sokell, F. Aumayr, et al. “Roadmap on photonic, electronic and atomic collision physics: II. Electron and antimatter interactions”. J. Phys. B: At. Mol. Opt. Phys. **52**(17), 171002 (2019).

[96] S. Iida, S. Kuma, H. Tanuma, et al. “State-Selective Observation of Radiative Cooling of Vibrationally Excited C_2^-”. J. Phys. Chem. Lett. **11**(24), 10526 (2020).

[97] C. Meyer, A. Becker, K. Blaum, et al. “Radiative Rotational Lifetimes and State-Resolved Relative Detachment Cross Sections from Photodetachment Thermometry of Molecular Anions in a Cryogenic Storage Ring”. Phys. Rev. Lett. **119**, 023202 (2017).

[98] H. T. Schmidt, G. Eklund, K. C. Chartkunchand, et al. “Rotationally Cold OH^- Ions in the Cryogenic Electrostatic Ion-Beam Storage Ring DESIREE”. Phys. Rev. Lett. **119**, 073001 (2017).

[99] C. Krantz, O. Novotný, A. Becker, et al. “Single-particle detection of products from atomic and molecular reactions in a cryogenic ion storage ring”. Nucl. Instrum. Methods Phys. Res. A: Accel. Spectrom. Detect. Assoc. Equip. **851**, 92 (2017).

[100] C. Krantz, F. Berg, K. Blaum, et al. "The Cryogenic Storage Ring and its application to molecular ion recombination physics". J. Phys.: Conf. Ser. **300**, 012010 (2011).

[101] H. T. Schmidt, R. D. Thomas, M. Gatchell, et al. "First storage of ion beams in the Double Electrostatic Ion-Ring Experiment: DESIREE". Rev. Sci. Instrum. **84**(5), 055115 (2013).

[102] R. von Hahn, A. Becker, F. Berg, et al. "The cryogenic storage ring CSR". Rev. Sci. Instrum. **87**(6), 063115 (2016).

[103] M. Germann, X. Tong, and S. Willitsch. "Observation of electric-dipole-forbidden infrared transitions in cold molecular ions". Nat. Phys. **10**(11), 820 (2014).

[104] O. Lakhmanskaya, M. Simpson, and R. Wester. "Vibrational overtone spectroscopy of cold trapped hydroxyl anions". Phys. Rev. A **102**, 012809 (2020).

[105] R. L. Champion, L. D. Doverspike, D. M. Scott, and Y. Wang. "Fundamental processes in low energy collisions of alkali anions and atoms". AIP Conf. Proc.; (United States) **158**(1), 536 (1987).

[106] B. Mant, E. Yurtsever, L. González-Sánchez, et al. "Vibrational quenching of CN^-in collisions with He and Ar". J. Chem. Phys. **154**(8), 084305 (2021).

[107] G. Ganteför, K. H. Meiwes-Broer, and H. O. Lutz. "Photodetachment spectroscopy of cold aluminum cluster anions". Phys. Rev. A **37**, 2716 (1988).

[108] L. González-Sánchez, S. Gómez-Carrasco, A. M. Santadaría, et al. "Collisional Quantum Dynamics for $MgH^-(^1\Sigma^+)$ With He as a Buffer Gas: Ionic State-Changing Reactions in Cold Traps". Front. Chem. **7:64** (2019).

[109] M. A. Cordiner, S. B. Charnley, J. V. Buckle, et al. "Discovery of Interstellar Anions in Cepheus and Auriga". Astrophys. J. **730**(2), L18 (2011).

[110] T. J. Millar. "Astrochemistry". Plasma Sources Sci. Technol. **24**(4), 043001 (2015).

[111] R. C. Fortenberry. "Interstellar Anions: The Role of Quantum Chemistry". J. Phys. Chem. A **119**(39), 9941 (2015).

[112] J. Simons. "Molecular Anions". J. Phys. Chem. A **112**(29), 6401 (2008).

[113] V. M. Bierbaum. "Anions in Space and in the Laboratory". Proc. Int. Astron. Union **7**(S280), 383–389 (2011).

[114] H. Kreckel, P. Herwig, D. Schwalm, et al. "Metastable states of diatomic hydrogen anions". J. Phys.: Conf. Ser. **488**(1), 012034 (2014).

[115] T. J. Millar, C. Walsh, and T. A. Field. "Negative Ions in Space". Chem. Rev. **117**(3), 1765 (2017).

[116] V. Vuitton, P. Lavvas, R. Yelle, et al. "Negative ion chemistry in Titan's upper atmosphere". Planet. Space Sci. **57**(13), 1558 (2009).

[117] J. Žabka, C. Romanzin, C. Alcaraz, and M. Polášek. "Anion chemistry on Titan: A possible route to large N-bearing hydrocarbons". Icarus **219**(1), 161 (2012).

[118] M. Larsson, W. D. Geppert, and G. Nyman. "Ion chemistry in space". Rep. Prog. Phys. **75**(6), 066901 (2012).

[119] F. C. Fehsenfeld and E. E. Ferguson. "Laboratory studies of negative ion reactions with atmospheric trace constituents". J. Chem. Phys. **61**(8), 3181 (1974).

[120] D. W. Fahey, H. Böhringer, F. C. Fehsenfeld, and E. E. Ferguson. "Reaction rate constants for $O_2^-(H_2O)_n$ ions $n = 0$ to 4, with O_3, NO, SO_2, and CO_2". J. Chem. Phys. **76**(4), 1799 (1982).

[121] W. N. Lipscomb and N. Sträter. "Recent Advances in Zinc Enzymology". Chem. Rev. **96**(7), 2375 (1996).

[122] C. Han, H. Su, Z. Sun, et al. "Biomimetic Ion Nanochannels as a Highly Selective Sequential Sensor for Zinc Ions Followed by Phosphate Anions". Chem. Eur. J. **19**(28), 9388 (2013).

[123] M. R. Jackson, R. Beahm, S. Duvvuru, et al. "A Preference for Edgewise Interactions between Aromatic Rings and Carboxylate Anions: The Biological Relevance of AnionQuadrupole Interactions". J. Phys. Chem. B **111**(28), 8242 (2007).

[124] Z.-C. Wang, Y.-K. Li, S.-G. He, and V. M. Bierbaum. "Reactivity of amino acid anions with nitrogen and oxygen atoms". Phys. Chem. Chem. Phys. **20**, 4990 (2018).

[125] C. Hollenstein. "The physics and chemistry of dusty plasmas". Plasma Phys. Control. Fusion **42**(10), R93 (2000).

[126] D. J. Economou. “Fundamentals and applications of ion–ion plasmas”. Appl. Surf. Sci. **253**(16), 6672 (2007).

[127] H. Kageyama, K. Hayashi, K. Maeda, et al. “Expanding frontiers in materials chemistry and physics with multiple anions”. Nat. Commun. **9**(1), 772 (2018).

[128] R. Casasús, M. D. Marcos, R. Martínez-Máñez, et al. “Toward the Development of Ionically Controlled Nanoscopic Molecular Gates”. J. Am. Chem. Soc. **126**(28), 8612 (2004).

[129] R. Casasús, E. Climent, M. D. Marcos, et al. “Dual Aperture Control on pH- and Anion-Driven Supramolecular Nanoscopic Hybrid Gate-like Ensembles”. J. Am. Chem. Soc. **130**(6), 1903 (2008).

[130] K. R. Lykke, R. D. Mead, and W. C. Lineberger. “Observation of Dipole-Bound States of Negative Ions”. Phys. Rev. Lett. **52**, 2221 (1984).

[131] K. D. Jordan and F. Wang. “Theory of Dipole-Bound Anions”. Annu. Rev. Phys. Chem. **54**(1), 367 (2003).

[132] P. Skurski and J. Simons. “An excess electron bound to urea. I. Canonical and zwitterionic tautomers”. J. Chem. Phys. **115**(18), 8373 (2001).

[133] S. Xu, J. M. Nilles, and K. H. Bowen. “Zwitterion formation in hydrated amino acid, dipole bound anions: How many water molecules are required?” J. Chem. Phys. **119**(20), 10696 (2003).

[134] T. J. Lee and C. E. Dateo. “Ab initio quartic force fields for anions: A benchmark study on $^{16}OH^-$, $^{18}OH^-$, and $^{16}OD^-$”. J. Chem. Phys. **107**(24), 10373 (1997).

[135] M. A. Cordiner and S. B. Charnley. “Negative ion chemistry in the coma of comet 1P/Halley”. Meteorit. Planet Sci. **49**(1), 21 (2014).

[136] J. C. Owrutsky, N. H. Rosenbaum, L. M. Tack, and R. J. Saykally. “The vibration-rotation spectrum of the hydroxide anion (OH^-)”. J. Chem. Phys. **83**(10), 5338 (1985).

[137] P. Langevin. “Une formule fondamentale de théorie cinétique”. Ann. Chim. Phys **5**, 245 (1905).

[138] R. Wester. “Radiofrequency multipole traps: tools for spectroscopy and dynamics of cold molecular ions”. J. Phys. B: At. Mol. Opt. Phys. **42**(15), 154001 (2009).

[139] H. Bruhns, H. Kreckel, K. Miller, et al. "A novel merged beams apparatus to study anion-neutral reactions". Rev. Sci. Instrum. **81**(1), 013112 (2010).

[140] E. E. Ferguson. "Ion-Molecule Reactions". Annu. Rev. Phys. Chem. **26**(1), 17 (1975).

[141] C. H. DePuy, J. J. Grabowski, and V. M. Bierbaum. "Chemical Reactions of Anions in the Gas Phase". Science **218**(4576), 955 (1982).

[142] V. M. Bierbaum. "Go with the flow: Fifty years of innovation and ion chemistry using the flowing afterglow". Int. J. Mass Spectrom. **377**, 456 (2015).

[143] S. G. Ard, J. J. Melko, B. Jiang, et al. "Temperature dependences for the reactions of O_2^- and O^- with N and O atoms in a selected-ion flow tube instrument". J. Chem. Phys. **139**(14), 144302 (2013).

[144] E. Teloy and D. Gerlich. "Integral cross sections for ion—molecule reactions. I. The guided beam technique". Chem. Phys. **4**(3), 417 (1974).

[145] K. Rempala and K. M. Ervin. "Collisional activation of the endoergic hydrogen atom transfer reaction $S^-(^2P)+H_2 \rightarrow SH^-+H$". J. Chem. Phys. **112**(10), 4579 (2000).

[146] Y. T. Lee, J. D. McDonald, P. R. LeBreton, and D. R. Herschbach. "Molecular Beam Reactive Scattering Apparatus with Electron Bombardment Detector". Rev. Sci. Instrum. **40**(11), 1402 (1969).

[147] D. M. Neumark, A. M. Wodtke, G. N. Robinson, et al. "Molecular beam studies of the $F+H_2$ reaction". J. Chem. Phys. **82**(7), 3045 (1985).

[148] J. J. Lin, J. Zhou, W. Shiu, and K. Liu. "Application of time-sliced ion velocity imaging to crossed molecular beam experiments". Rev. Sci. Instrum. **74**(4), 2495 (2003).

[149] J. Mikosch, S. Trippel, C. Eichhorn, et al. "Imaging Nucleophilic Substitution Dynamics". Science **319**(5860), 183 (2008).

[150] D. Gerlich. "Inhomogeneous rf fields: A versatile tool for the study of processes with slow ions". Adv. Chem. Phys. **82**, 1 (1992).

[151] D. Gerlich and M. Smith. "Laboratory astrochemistry: studying molecules under inter- and circumstellar conditions". Physica Scripta **73**(1), C25 (2005).

[152] E. R. Lovejoy and R. R. Wilson. “Kinetic Studies of Negative Ion Reactions in a Quadrupole Ion Trap: Absolute Rate Coefficients and Ion Energies”. J. Phys. Chem. A **102**(13), 2309 (1998).

[153] R. Otto, J. Mikosch, S. Trippel, et al. “Nonstandard Behavior of a Negative Ion Reaction at Very Low Temperatures”. Phys. Rev. Lett. **101**, 063201 (2008).

[154] F. A. Gianturco, L. González-Sánchez, B. P. Mant, and R. Wester. “Modeling state-selective photodetachment in cold ion traps: Rotational state “crowding” in small anions”. J. Chem. Phys. **151**(14), 144304 (2019).

[155] J. Franz, B. P. Mant, L. González-Sánchez, et al. “Rotational state-changing collisions of C_2H^- and C_2N^- anions with He under interstellar and cold ion trap conditions: A computational comparison”. J. Chem. Phys. **152**(23), 234303 (2020).

[156] D. Hauser, S. Lee, F. Carelli, et al. “Rotational state-changing cold collisions of hydroxyl ions with helium”. Nat. Phys. **11**(6), 467 (2015).

[157] E. Endres, G. Egger, S. Lee, et al. “Incomplete rotational cooling in a 22-pole ion trap”. J. Mol. Spectrosc. **332**, 134 (2017).

[158] X.-B. Wang, H.-K. Woo, and L.-S. Wang. “Vibrational cooling in a cold ion trap: Vibrationally resolved photoelectron spectroscopy of cold C_{60}^- anions”. J. Chem. Phys. **123**(5), 051106 (2005).

[159] M. Simpson, M. Nötzold, T. Michaelsen, et al. “Influence of a Supercritical Electric Dipole Moment on the Photodetachment of C_3N^-”. Phys. Rev. Lett. **127**, 043001 (2021).

[160] D. Gerlich, P. Jusko, Š. Roučka, et al. “Ion trap studies of $H^- + H \rightarrow H_2 + e^-$ between 10 and 135 K”. Astrophys. J. **749**(1), 22 (2012).

[161] K. Geistlinger, M. Fischer, S. Spieler, et al. “A sub-4 Kelvin radio frequency linear multipole wire trap”. Rev. Sci. Instrum. **92**(2), 023204 (2021).

[162] J. Deiglmayr, A. Göritz, T. Best, et al. “Reactive collisions of trapped anions with ultracold atoms”. Phys. Rev. A **86**, 043438 (2012).

[163] B. Höltkemeier, P. Weckesser, H. López-Carrera, and M. Weidemüller. “Dynamics of a single trapped ion immersed in a buffer gas”. Phys. Rev. A **94**, 062703 (2016).

[164] B. Höltkemeier, P. Weckesser, H. López-Carrera, and M. Weidemüller. “Buffer-Gas Cooling of a Single Ion in a Multipole Radio Frequency Trap Beyond the Critical Mass Ratio”. Phys. Rev. Lett. **116**, 233003 (2016).

[165] M. Kas, J. Loreau, J. Liévin, and N. Vaeck. “Reactivity of Hydrated Hydroxide Anion Clusters with H and Rb: An ab Initio Study”. J. Phys. Chem. A **123**(41) (2019).

[166] B. Höltkemeier, J. Glässel, H. López-Carrera, and M. Weidemüller. “A dense gas of laser-cooled atoms for hybrid atom–ion trapping”. Appl. Phys. B **123**(1), 51 (2017).

[167] S. Trippel, J. Mikosch, R. Berhane, et al. “Photodetachment of Cold OH^- in a Multipole Ion Trap”. Phys. Rev. Lett. **97**, 193003 (2006).

[168] J. Tauch New approaches for cooling molecular anions to the Kelvin range (Ph.D. Thesis, Universität Heidelberg, 2021).

[169] H. López-Carrera Sympathetic cooling and rotational quenching of molecular anions in a hybrid atom ion trap (Ph. D. thesis, Universität Heidelberg, 2018).

[170] B. Höltkemeier Sympathetic cooling of ions in a hybrid atom ion trap (Ph. D. thesis, Universität Heidelberg, 2016).

[171] J. Glässel Saturation absorption imaging of a high-density rubidium dark spot (Master thesis, Universität Heidelberg, 2014).

[172] D. L. Osborn, D. J. Leahy, D. R. Cyr, and D. M. Neumark. “Photodissociation spectroscopy and dynamics of the $N_2O_2^-$ anion”. J. Chem. Phys. **104**(13), 5026 (1996).

[173] C. Greve, M. Kröner, S. Trippel, et al. “Storage of protonated water clusters in a biplanar multipole rf trap”. New J. Phys. **12**(6), 065035 (2010).

[174] N. Beier A versatile anion source for studying atom-ion collisions (Bachelor thesis, Universität Heidelberg, 2017).

[175] J. Trautmann Manipulating Hydroxyl Anions - Hydration and Rotational Cooling (Master Thesis, Universität Heidelberg, 2018).

[176] W. C. Wiley and I. H. McLaren. “Time-of-Flight Mass Spectrometer with Improved Resolution”. Rev. Sci. Instrum. **26**(12), 1150 (1955).

[177] W. D. Phillips. "Nobel Lecture: Laser cooling and trapping of neutral atoms". Rev. Mod. Phys. **70**, 721 (1998).

[178] W. Ketterle, K. B. Davis, M. A. Joffe, et al. "High densities of cold atoms in a dark spontaneous-force optical trap". Phys. Rev. Lett. **70**, 2253 (1993).

[179] B. Höltkemeier 2D MOT as a source of a cold atom target. (Diploma thesis, Universität Heidelberg, 2011).

[180] P. Hlavenka, R. Otto, S. Trippel, et al. "Absolute photodetachment cross section measurements of the O^- and OH^- anion". J. Chem. Phys. **130**(6), 061105 (2009).

[181] G. Reinaudi, T. Lahaye, Z. Wang, and D. Guéry-Odelin. "Strong saturation absorption imaging of dense clouds of ultracold atoms". Opt. Lett. **32**(21), 3143 (2007).

[182] D. A. Steck "Rubidium 85 D Line Data available online at `http://steck.us/alkalidata` (revision 2.2.3, 9 July 2021)."

[183] C. G. Townsend, N. H. Edwards, C. J. Cooper, et al. "Phase-space density in the magneto-optical trap". Phys. Rev. A **52**, 1423 (1995).

[184] S. Chakrabarty, M. Holz, E. K. Campbell, et al. "A Novel Method to Measure Electronic Spectra of Cold Molecular Ions". J. Phys. Chem. Lett. **4**(23), 4051 (2013).

[185] O. Asvany, K. M. T. Yamada, S. Brünken, et al. "Experimental ground-state combination differences of CH_5^+". Science **347**(6228), 1346 (2015).

[186] M. Brümmer, C. Kaposta, G. Santambrogio, and K. R. Asmis. "Formation and photodepletion of cluster ion–messenger atom complexes in a cold ion trap: Infrared spectroscopy of VO^+, VO_2^+, and VO_3^+". J. Chem. Phys. **119**(24), 12700 (2003).

[187] O. Asvany, P. K. P, B. Redlich, et al. "Understanding the Infrared Spectrum of Bare CH_5^+". Science **309**(5738), 1219 (2005).

[188] P. Jusko, O. Asvany, A.-C. Wallerstein, et al. "Two-Photon Rotational Action Spectroscopy of Cold OH^- at 1 ppb Accuracy". Phys. Rev. Lett. **112**, 253005 (2014).

[189] S. Lee, D. Hauser, O. Lakhmanskaya, et al. "Terahertz-visible two-photon rotational spectroscopy of cold OD^-". Phys. Rev. A **93**, 032513 (2016).

[190] O. Lakhmanskaya, M. Simpson, S. Murauer, et al. "Rotational Spectroscopy of a Triatomic Molecular Anion". Phys. Rev. Lett. **120**, 253003 (2018).

[191] S. Lee, K. Ravi, and S. A. Rangwala. "Measurement of collisions between rubidium atoms and optically dark rubidium ions in trapped mixtures". Phys. Rev. A **87**, 052701 (2013).

[192] R. Otto, A. von Zastrow, T. Best, and R. Wester. "Internal state thermometry of cold trapped molecular anions". Phys. Chem. Chem. Phys. **15**, 612 (2013).

[193] A. K. Hansen, O. O. Versolato, Ł. Kłosowski, et al. "Efficient rotational cooling of Coulomb-crystallized molecular ions by a helium buffer gas". Nature **508**(7494), 76 (2014).

[194] H. Bohringer, W. Glebe, and F. Arnold. "Temperature dependence of the mobility and association rate coefficient of He^+ ions in He from 30-350 K". J. Phys. B: At. Mol. Opt. Phys. **16**(14), 2619 (1983).

[195] C. Basic, J. R. Eyler, and R. A. Yost. "Probing trapped ion energies via ion-molecule reaction kinetics: Quadrupole ion trap mass spectrometry". J. Am. Soc. Mass Spectrom. **3**(7), 716 (1992).

[196] J. C. Bergquist, D. J. Wineland, W. M. Itano, et al. "Energy and Radiative Lifetime of the $5d^9 6s^{2^2} D_{\frac{5}{2}}$ State in Hg II by Doppler-Free Two-Photon Laser Spectroscopy". Phys. Rev. Lett. **55**, 1567 (1985).

[197] O. Asvany, O. Ricken, H. S. P. Müller, et al. "High-Resolution Rotational Spectroscopy in a Cold Ion Trap: H_2D^+ and D_2H^+". Phys. Rev. Lett. **100**, 233004 (2008).

[198] M. Lunney, F. Buchinger, and R. Moore. "The Temperature of Buffer-gas Colled Ions in a Paul Trap". J. Mod. Opt. **39**(2), 349 (1992).

[199] F. Vedel and J. André. "Influence of space charge on the computed statistical properties of stored ions cooled by a buffer gas in a quadrupole rf trap". Phys. Rev. A **29**, 2098 (1984).

[200] H. Dehmelt. "Radiofrequency Spectroscopy of Stored Ions II: Spectroscopy". Adv. At. Mol. Opt. Phys. **5**, 109 (1969).

[201] I. Rouse and S. Willitsch. "Superstatistical velocity distributions of cold trapped ions in molecular-dynamics simulations". Phys. Rev. A **92**, 053420 (2015).

[202] M. Guilhaus. “Special feature: Tutorial. Principles and instrumentation in time-of-flight mass spectrometry. Physical and instrumental concepts”. J. Mass Spectrom. **30**(11), 1519 (1995).

[203] J. L. Franklin, P. M. Hierl, and D. A. Whan. “Measurement of the Translational Energy of Ions with a Time-of-Flight Mass Spectrometer”. J. Chem. Phys. **47**(9), 3148 (1967).

[204] L. Spitzer Physics of fully ionized gases. (Interscience Publ., New York, 2.edition, 1962).

[205] P. Allmendinger, J. Deiglmayr, K. Höveler, et al. “Observation of enhanced rate coefficients in the $H_2^+ + H_2 \rightarrow H_3^+ + H$ reaction at low collision energies”. J. Chem. Phys. **145**(24), 244316 (2016).

[206] Z.-C. Wang and V. M. Bierbaum. “Reactions of substituted benzene anions with N and O atoms: Chemistry in Titan’s upper atmosphere and the interstellar medium”. J. Chem. Phys. **144**(21), 214304 (2016).

[207] D. Smith and P. Spanel. “Ions in the terrestrial atmosphere and in interstellar clouds”. Mass Spectrom. Rev. **14**(4-5), 255 (1995).

[208] N. Y. Bykov and D. V. Leshchev. “Modelling of water clusters formation processes in the inner atmosphere of comets”. J. Phys. Conf. Ser. **438**, 012008 (2013).

[209] P. Chaizy, H. Rème, J. A. Sauvaud, et al. “Negative ions in the coma of comet Halley”. Nature **349**(6308), 393 (1991).

[210] E. Fermi and E. Teller. “The Capture of Negative Mesotrons in Matter”. Phys. Rev. **72**, 399 (1947).

[211] P. Linstrom and W. Mallard Eds., NIST Chemistry WebBook, NIST Standard Reference Database Number 69 (National Institute of Standards and Technology, Gaithersburg MD, 20899).

[212] J. Simons. “Propensity rules for vibration-induced electron detachment of anions”. J. Am. Chem. Soc. **103**(14), 3971 (1981).

[213] Z. Idziaszek, T. Calarco, and P. Zoller. “Controlled collisions of a single atom and an ion guided by movable trapping potentials”. Phys. Rev. A **76**, 033409 (2007).

[214] L. Ratschbacher, C. Sias, L. Carcagni, et al. “Decoherence of a Single-Ion Qubit Immersed in a Spin-Polarized Atomic Bath”. Phys. Rev. Lett. **110**, 160402 (2013).

[215] P. Puri, M. Mills, C. Schneider, et al. “Synthesis of mixed hypermetallic oxide $BaOCa^+$ from laser-cooled reagents in an atom-ion hybrid trap”. Science **357**(6358), 1370 (2017).

[216] S. Willitsch, M. T. Bell, A. D. Gingell, et al. “Cold Reactive Collisions between Laser-Cooled Ions and Velocity-Selected Neutral Molecules”. Phys. Rev. Lett. **100**, 043203 (2008).

[217] F. H. J. Hall and S. Willitsch. “Millikelvin Reactive Collisions between Sympathetically Cooled Molecular Ions and Laser-Cooled Atoms in an Ion-Atom Hybrid Trap”. Phys. Rev. Lett. **109**, 233202 (2012).

[218] S. Haze, R. Saito, M. Fujinaga, and T. Mukaiyama. “Charge-exchange collisions between ultracold fermionic lithium atoms and calcium ions”. Phys. Rev. A **91**, 032709 (2015).

[219] W. W. Smith, D. S. Goodman, I. Sivarajah, et al. “Experiments with an ion-neutral hybrid trap: cold charge-exchange collisions”. Appl. Phys. B **114**(1), 75 (2014).

[220] M. Kas, J. Loreau, J. Liévin, and N. Vaeck. “Cold reactive and nonreactive collisions of Li and Rb with ${C_2}^-$: Implications for hybrid-trap experiments”. Phys. Rev. A **99**, 042702 (2019).

[221] C. W. Bauschlicher, H. Partridge, and L. G. M. Pettersson. “Franck–Condon factors for photodetachment from LiO^-, NaO^-, and KO^-”. J. Chem. Phys. **99**(5), 3654 (1993).

[222] B. Mintz, B. Chan, M. B. Sullivan, et al. “Structures and Thermochemistry of the Alkali Metal Monoxide Anions, Monoxide Radicals, and Hydroxides”. J. Phys. Chem. A **113**(34), 9501 (2009).

[223] C. Zipkes, L. Ratschbacher, C. Sias, and M. Köhl. “Kinetics of a single trapped ion in an ultracold buffer gas”. New J. Phys. **13**(5), 053020 (2011).

[224] C. Tsallis. “Possible generalization of Boltzmann-Gibbs statistics”. J. Stat. Phys. **52**(1), 479 (1988).

[225] C. Tsallis, R. Mendes, and A. Plastino. “The role of constraints within generalized nonextensive statistics”. Phys. A: Stat. Mech. Appl **261**(3), 534 (1998).

[226] P. Weckesser, F. Thielemann, D. Wiater, et al. “Observation of Feshbach resonances between a single ion and ultracold atoms”. Nature **600**(7889), 429 (2021).

[227] “COMSOL Multiphysics, version 5.4.” Available at `https://www.comsol.com/`.

[228] R. Otto, P. Hlavenka, S. Trippel, et al. “How can a 22-pole ion trap exhibit ten local minima in the effective potential?” J. Phys. B: At. Mol. Opt. Phys. **42**(15), 154007 (2009).

ACKNOWLEDGEMENTS

This thesis would not have been possible without the relentless support and guidance of so many people. This time was an extremely humbling experience and I would like to thank everyone who helped me in some way or the other in the last few years and even, in these uncertain times, for making this time indeed a memorable one.

Firstly, I would like to thank **Prof. Dr. Matthias Weidemüller** for giving me an opportunity to work in his group and the hybrid atom-ion trap (HAITrap) experiment. Your thoughts and ideas have always inspired me. Without your unmatched guidance and support, none of the work in this thesis would have been possible. Thanks to you, I immediately felt comfortable in the group, and thank you for the confidence you showed in me over the last few years.

I would also like to extend my thanks to **Prof. Dr. Roland Wester**. With your expertise and knowledge, we gained a lot of insights from the discussions within our collaboration. Thank you for your ideas and motivation that helped make this work better.

I would also like to thank **Prof. Dr. Andreas Wolf** for his cooperation and agreeing to be the second referee for my thesis, and evaluation of this work. I would also like to express my gratitude towards **Prof. Dr. Ulrich Schwarz** and **Dr. Robert Moshammer** for being on my doctoral exam committee.

Undoubtedly, thanks are also due to the entire **HAITrap team** for being the close-knit group that it is. Every member of the team had been extremely welcoming, and helpful throughout my time here! I would also like to thank them for unhesitatingly switching to English once I started in the group, always trying to translate the jokes for me. I am sure the Bräustadl misses the group more than ever! I surely do! I have learned something from each one of you and I couldn't have asked for a better working group and am thankful to everyone who was a part of this team. With the HAITrap chapter closing in Heidelberg, this really seems like the end of an era...

One person who I cannot thank enough is **Jonas**. I learned so much from you, not just about the experiment but also about things outside the lab. Thank you for your patience and time in explaining and helping me with things. None of the results achieved would have been possible without your support. I also want to

thank you for all the times you made things easier for me, be it helping me in the lab even when you were writing or accompanying me to the Foreign Office for my early morning visa appointments. I really enjoyed our conversations about the football club opera, you "winning" the lottery, trash TV, ant farm, etc. I could always look up to you for advice as I knew you would always help me with your useful inputs and I really missed your presence in the last months here.

Markus! Thank you so much for everything. You had always been around to help and motivate me whenever I needed support. You always inspired me with your work and words. Without your constant support and cheering, the road to this thesis would have been extremely difficult. Thank you for helping me at each step and believing in me sometimes even more than I did myself. It took some time but you made sure I came around to appreciate your dark humor. Most importantly, thank you for your innumerable memes that always managed to crack me up.

Milaim, I would like to thank you for your constant help, work, and patience during this collaboration. Your insights always (please read as "usually") turned out to be extremely valuable and formed the theoretical basis of this work. It always amazed me how you manage so many hobbies together and I really appreciate you for that! I wish you the best for the future and many congratulations for embarking on your new journey, both personally and professionally!

Domme!! You had been extremely nice to me from the very first day when I was at the institute for my interview. Your dedication and sincerity towards work always inspired me. More than that, you had always been a great friend to all of us in the group. Thank you for being super enthusiastic about the trips to halle02 and also helping me with my apartment move! It was always fun to join you for the Friday beers and music at the workshop. Thank you for dragging us to The Keller at the DPG in Rostock. It was so much fun! Britta and you have always been really warm and welcoming to everyone around and I am so happy to have been friends with you.

Eric, I always appreciated your optimistic attitude even during the tougher times. Your presence comforted me in the initial years of my time here. I learned a lot from you and thank you for all the help and support over these years! Your dedication towards the football world cup, Karaoke at O'Reilleys, and DJ nights at halle02 were really infectious and I remember these times with a lot of fondness!

Jan, thank you for helping me feel welcomed while I started in the group. I always found your insights quite interesting! I believe it was also you who introduced the idea of Jägermeister at Braustädl to me (and maybe I do not thank you so much for that)!! Nevertheless, thank you for these fun times and for always keeping in touch (with your notepad filled with Jonas' "jokes") and I wish you the best for your future.

Henry, Henry, Henry! You are one of the most friendly and craziest people I have met! Thank you for always being the enthusiastic soul that you are!

Basti, though we didn't have any overlap with our time at the HAITrap, I always believed that the HAITrap got its fun spirit largely from you! Thank you for always making me feel included as a part of the group. I would also like to thank **Ioanna** for always being so warm and cordial to me. You always made me feel comfortable and thank you so much for unhesitatingly offering to help me whenever you could.

I thank the **Mixtures** team for the fun and friendly chats. I want to especially thank Binh, Manuel, and Eleonora for the fun time we had together in China and the time we worked together on the ventilator project. I would like to thank **Manuel** for his weird sense of humor and the constant exchange of Instagram memes. I cannot thank **Eleonora** enough for always being willing to help and being so warm and friendly. You were one of the first few friends I made in Heidelberg and the group when we met the first time at the IMPRS-QD interviews. You always tried to instill confidence and motivation in me whenever I felt low and I really thank you for all these times, and am extremely grateful to have you around!

I would also like to extend my thanks to the entire **Quantum Dynamics** group for a great working time during the last few years.

I would also to thank **Claudia** for always being cordial while trying to help me with the administrative things during the last years! I cannot thank you enough for your time and help.

I would also take this opportunity to thank **HGSFP and IMPRS-QD graduate schools** for their financial support and for organizing very informative workshops.

Thanks to all my friends who also, in some way or the other, helped me during my time here. My friends from Bonn often helped me in the initial months of my time in Heidelberg. I would like to thank **Keshav** for helping me a lot in settling here. I want to thank **Vasanth**, who no matter what, always made me laugh, and for being the brother I never had! **Karthik**, your motivation and enthusiasm always inspired me and I wish you all the best for your doctoral work. **Avu**, we have already known each other for a long time, and our bond has only gotten stronger over the last few years. Thank you for always bringing me joy and love and I wish the utmost happiness for you.

Another group of people, I cannot thank enough are these amazing people I met in Heidelberg! **Apoorva**, it was amazing how we had heard so much about each other without even meeting once before! Thank you for always being there, especially during the really low times when I needed you the most. I am also grateful that we could always cry together over our own experiments and vacuum horror stories.

Kaustav, Bhaii, thank you for your help whenever I needed you. I would like to thank you for the amazing times at Vetters and the great Tandoori chicken! Thank you for sharing my struggles regarding the contracts and sorry (not sorry) for having joined Apoorva's quest of "Let me zoom his face".

Praveen macha, I am always amazed at your contacts and your nature of helping everyone, come what may! You had always been a dependable friend and despite our initial fights, you had been an important part of my life here. I admire your discipline and dedication and I wish you the best for the new phase of your life that you are embarking on!

Vikas macha!! Thank you for always understanding me and always sharing the first laughs with me because..well..we both have equally weird minds.Thank you for always being the fun one in the group. I know I can always count on you Macha! Thank you so much for being a part of my life!

Reena, I would like to thank you for all the fun times we had together over the last few years.

Venky Pai, I probably met you the last but already in that short time, we have made so many memories together. I remember being amazed the first time at your capability to sleep on Regional Train rides and well, I still am. Thank you for bearing with all my rants over the last few years and always trying to cheer me up, mostly with Food! Thank you for introducing me to so many new places and people. I am so grateful to have you in my life and I hope we can embark on many more adventures together in the future too!

Shiti, you have been such a great friend to me for the last 7 years. From Delhi to Germany you have always helped me gain peace and comfort whenever I needed it the most. You are like a sister to me. **Sagar** and you have together become such an important part of my life and I am so lucky to have you in my life.

Last but not the least, I would like to thank my family for their undying love, support, and guidance throughout my life. My eldest sister **Shazia** for being the strong person that she is and for always inspiring me to do better and work harder in life. My sister **Sana** for literally everything. Thank you for inspiring me and for being the one constant that I had and will continue to have for the rest of my life. I can never imagine my life without you in it. Thank you to both my sisters for always having my back and creating a strong support system for me. I would like to thank **Abhaar** for always trying to keep us happy and for always looking out for us. I would like to thank my parents, **Papa** and **Mumma** for all their sacrifices, hard work, and guidance in shaping each one of us into the people we are. Thank you for your determination and love for all of us over anything else. None of us could have achieved anything without you and your support. All we are and ever will be is dedicated to both of you!